Development of bandgap graded a-SiO$_x$:H solar cells

for two-terminal and four-terminal applications

Venkateswaran Raman

Photovoltaic Materials and Devices Group, ESE, EEMCS, TU Delft

TU Delft

Development of bandgap graded a-SiO$_x$:H solar cells
for two-terminal and four-terminal applications

by

Venkateswaran Raman

in partial fulfillment of the requirements for the Master of Science in

Electrical Sustainable Energy

at the Delft University of Technology,
to be defended publicly on Wednesday October 3, 2018 at 2:00 PM.

Student number:	4622790	
Supervisor:	Dr. R.A.C.M.M. van Swaaij,	TU Delft
Thesis committee:	Prof. Dr. ir. Arno. H. M. Smets,	TU Delft
	Dr. Erik van der Kolk,	TU Delft
	Dr. ir. R. Santbergen,	TU Delft

This thesis is confidential and cannot be made public until October 3, 2018.

An electronic version of this thesis is available at `http://repository.tudelft.nl/`.

TU Delft Delft University of Technology

Acknowledgement

I would like to express my gratitude to Dr. Rene van Swaaij for providing me with the opportunity to do my master thesis on graded bandgap energy a-SiO_x:H solar cells. I am very lucky to have you as my thesis supervisor and as a daily supervisor. I have learned so much from you during our weekly meetings, be it the basics, approaching the grading method, experiment planning, result presentation and analysis. Aside from the guidance that you provided me with, I am also grateful to you for giving me the freedom to carry out the experiments and the freedom to contact you any time in person or by mail. This thesis could not have been accomplished without your help and support.

I also thank Martijn Tijssen and Stefaan Heirman who helped me a lot with the training on the use of the deposition and measurement systems. I remember a solid block of two - three months when the matchbox for one of the deposition chambers was malfunctioning and the both of you had been there to switch the functioning matchbox back and forth between the two deposition chambers so that i could proceed with my work. I thank the both of you again for the technical support provided during the course of my thesis.

I am also very thankful to Dr. Rudi Santbergen for his help with simulations on the graded bandgap energy layers. You have supported me during a time when I had no idea on how to interpolate the n and k data for using in my simulation. I also thank you for helping me with some of the coding done by matlab.

I would like to thank Michele, Taha and Sandeep for being the best office mates. I also want to thank Radhakrishnan, my good friend, spending endless days helping each other on depositions and simulations. Best of luck to all of you.

I would like to thank my parents for their continued love and support. I am who I am because of the both of you. Both of you have given me a lot of freedom, exposure to different cultures, an education and a humble home for which i am fortunate.

Venkateswaran Raman
Delft, September 2018

Abstract

Of all the renewable energy sources, solar energy has a high potential. Electricity generated from photovoltaic (PV) systems have risen by 25% since 2008 and around 1% of global electricity consumption comes from PV systems. Amongst others, this is a result of the decrease in the prices of wafer based (c-Si) PV modules by 83% from 2010 to 2017.

Although researchers have been increasing the efficiency of c-Si based solar cells, they have also been investigating the application of thin films in photovoltaics. Thin film silicon solar cells make use of a thin layer of absorber material compared to the thicker absorber layers seen in c-Si based solar cells. However, due to the thin absorber layer, thin film silicon solar cells exhibit a low short-circuit current density (J_{SC}).

In this work we show results on hydrogenated amorphous silicon oxide (a-SiO_x:H) solar cells. These solar cells are interesting as they potentially can have a high $V_{OC}\times$ fill factor (FF) product. But, a-SiO_x:H solar cells have small J_{SC} in comparison to a-Si:H solar cells because of their high bandgap energy. Research has shown that increasing the absorber layer thickness of a-SiO_x:H solar cells, increases the J_{SC}, but leads to an increase in absorber layer thickness also contributes to a decrease in the $V_{OC}\times$ FF product. Above a certain thickness, the conversion efficiency of the solar cell drops dramatically as the $V_{OC}\times$ FF product drops fast. This means that the increase in J_{SC} as a result of increasing absorber layer thickness of a-SiO_x:H solar cells is limited to a certain value of the absorber layer thickness. An alternate way of increasing the J_{SC} needs to be investigated.

One such way is through grading the bandgap energy of the absorber layer for a-SiO_x:H solar cells. The bandgap energy is linearly graded to lower bandgap energy values, aiming at absorbing lower energetic photons by the absorber layer and leading to a higher J_{SC}. This is the focus of this work.

In this thesis, **graded bandgap energy a-SiO_x:H solar cells are developed to attain a high J_{SC} without compromising their high $V_{OC}\times$ FF product**. First, a grading method which takes into account the interdependence of bandgap energy, deposition rate and the desired grading profile for a-SiO_x:H materials is developed. Then, graded bandgap energy a-SiO_x:H solar cells are fabricated to investigate the optimum grading width. The bandgap energy is linearly graded from 2.1 eV to 1.96 eV. It was observed that, when fabricating graded bandgap energy a-SiO_x:H solar cells, the grading width at both the ends of the absorber layer should be as small as possible. A 10 nm grading at the front end and 20 nm grading in the rear of the absorber layer showed the best result among all the graded bandgap cells developed during the optimization, with an efficiency of 8.2 % (V_{OC}: 0.96 V, J_{SC}: 13.36 mA/cm^2, FF: 0.64).

The effects of grading the bandgap energy on the performance of a-SiO_x:H solar cells were also investigated. For instance the bandgap variation within the graded region was investigated. We found that increasing the range over which the bandgap energy is varied within a fixed graded region was detrimental to the J_{SC} and FF. When increasing the thickness of the graded bandgap energy absorber layer for a-SiO_x:H, J_{SC} as high as 14.4 mA/cm^2 was achieved. Also, the increase in the thickness of these graded bandgap energy absorber layers did not result in a drastic drop in efficiency as seen for a-SiO_x:H solar cells without bandgap energy grading.

Finally, optical simulations of graded bandgap energy a-SiO_x:H solar cells were attempted. Graded bandgap energy i-a-SiO_x:H layers were simulated. The matching of the simulated absorbance to the measured absorbance of the graded bandgap absorber layers were found to be satisfactory. However, the simulations of the graded bandgap energy a-SiO_x:H solar cells were not satisfactory and requires more attention.

Further research into improving the FF of graded bandgap energy solar cells can help increase the $V_{OC}\times$ FF product and efficiency of such devices. Moreover, the increase in J_{SC} obtained by grading the bandgap energy makes the device a suitable candidate for a top cell in four-terminal (4T) applications.

Contents

List of Figures

List of Tables

1 Introduction

1.1. Energy demand, consumption and the need for renewables

Energy is a major driving force for the economy of all countries in the world. As seen in Figure 1.1, the majority of energy comes from fossil fuels, with oil, coal and natural gas being the dominant fossil fuels being consumed. Among these oil is the most consumed energy source, followed by coal and then natural gas. These three dominant fossil fuels are termed as primary energy sources.

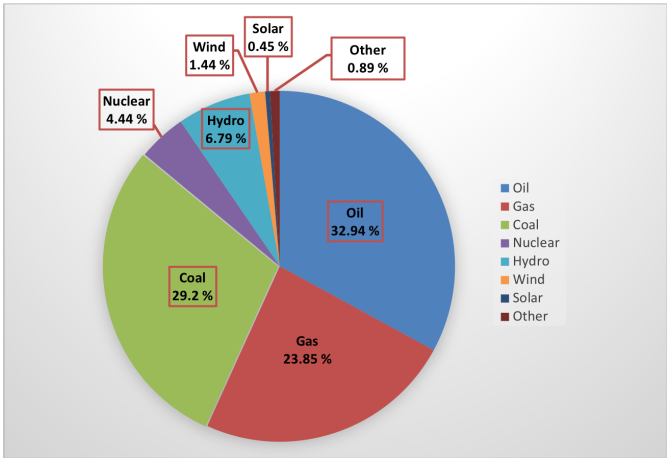

Figure 1.1: Energy consumption contributed by over various energy sources [1].

As of 2014, global consumption of primary energy sources equivalent to 13.28 billion metric tons of oil was recorded [20]. This included Asia and Pacific regions which contained the highest consumption rate. With a fast-growing economy and a population well above a billion, China is the largest primary energy consumer in the world. It is estimated that the global population will reach 9.7 billion by 2050 and world energy consumption to grow by 28% between 2015 and 2040 [21, 22].

According to the International Energy Outlook report published in 2018 by the U.S Energy Information Administration, rise in primary energy consumption is related to the rise in population [23]. Especially the rise in population is expected in developing countries like China, India and countries in Africa in the coming years. It is also not just the rise in population in the developing countries that drives the demand for primary energy consumption in the developing countries, but also the consumption per individual also increases. Since 1960, the primary energy demand per capita has doubled [1]. These two factors combined lead to an increase in energy demand.

The increasing demand of energy needs to be met with a suitable supply of energy sources. The future consumption of fossil fuels is significantly impacted by the limitations in resources available across the world. When it comes to the availability of oil, the amount of oil reserves is not the only limiting factor, but it is also the rate of extraction. 'Peak oil' is described as a point at which maximum extraction of oil has reached and

after which production has declined [20]. According to reputable bodies such as the International Energy Agency [20], peak oil is likely to occur around 2020. Though the consequences of peak oil are not known, it is highly likely that oil prices will soar and production will be difficult as procurement of energy will probably be from unconventional oil reserves. These are reserves from which resources are difficult and expensive to produce in comparison to conventional reserves which can be produces using traditional drilling methods.

Another figure of merit which is used to express the remaining amount of fossil fuels from proved reserves is the reserves to production ratio (R/P ratio)[24]. Proved reserves are reserves which have been discovered and declared. A reputable source of the R/P ratio for natural gas is BP Statistical Review of World Energy [25]. BP indicates that the Middle East has just another 80 years of production and Europe has another 63 years [25] of production left. Coal has a worldwide R/P ratio of 122 years, with Europe having a R/P ratio of 51 years. The UK is shown to have 155 million tonnes of coal reserves [25]. With the current rate of production, UK has a R/P ratio of 9 years for coal. Uranium is used as fuel for nuclear reactors and it faces similar limitations as fossil fuels. For security reasons the R/P ratio for uranium is not available. However, the World Nuclear Association [26] estimates that the R/P ratio for uranium is over 200 years. Another source of nuclear fuel is thorium, which is naturally available three times more than uranium. Technology for the use of thorium in existing nuclear reactors is not yet mature but there is potential to enhance the supply of energy from thorium through nuclear. The R/P ratio is at best only an indication of the amount of non-renewable sources. The R/P ratio takes into account only present production rates, which is deemed to change in the future with the increase in demand. Also, it does not take into account the resources that may become viable reserves in the future and reserves not discovered.

But the availability of energy from fossil fuels are not only influenced by the limited amount of naturally occurring resources. Fuel availability can also be restricted by commercial and political pressures across borders [24]. Energy geopolitics focuses on the use of natural resources and the impact of geographic characteristics in national and foreign policies [27]. The geopolitics of energy looks into two elements: (1) the location of the resource; and (2) the politics of state - it may be a state in which resource is found or a state that is reliant on the resource [27]. Energy resources can change the state of politics that can be a source of power, control and influence. For instance a country can hold the supply of energy hostage over another nation for influence in matters of legislation and security. This especially true for Europe, as they import a majority of their energy from other countries. Energy resources are also essential to ensure national and global stability and security.

The consumption of fossil fuel based natural resources results in the emission of green house gasses. When fossil fuels are converted into energy, waste products like CO_2 and water are also produced. While CO_2 is a naturally occurring green house gas, large quantities emitted into the atmosphere has been proved to cause global warming. In 2016 around 10 billion tons of CO_2 emission from fossil fuels was recorded. This value is exactly as foretold by Flavin and Dunn in a 1998 report titled ' The state of the world -1998 [28]. The increase in CO_2 emissions are projected to increase dramatically over the next 20 years if production of energy from fossil fuels were to keep increasing. The increasing trend of CO_2 emission overwhelms the natural cycling of CO_2 by the oceans and the forests and has brought the CO_2 concentration in the atmosphere up by 29% since the pre-industrial age. If the current trend of increasing emissions through the consumption of fossil fuels were to continue, then there is a possibility that the global temperature could increase by 1-3.5 ^oC as suggested by renowned climatologist Stephen Schneider [29]. The consequences of climate change are rise in sea levels, droughts, heat waves, change in precipitation patterns and frost-free seasons will lengthen [28, 29].

A way to overcome the limited supply of fossil fuels and emission of green house gases is to employ renewable energy sources to meet energy demands. Technologies have now become available to convert the sunlight, wind and earth's heat into energy which can meet the needs of the world's energy demand. These technologies are much more environmental friendly than utilizing fossil fuels and can cut carbon emissions by upto 80% [28]. Solar energy is energy which comes from the sun itself. The sun is made up of mostly hydrogen and helium in a plasma state. During the nuclear fusion process taking place at the sun's core, radiant energy from the solar surface is released and reaches the Earth in under 8 minutes [30].

Sunlight has the highest theoretical potential of all the renewable energy sources. Only 50% of sunlight strikes the surface of the Earth, the rest are either scattered or absorbed by atmosphere and clouds. Off the amount of sunlight that strikes the surface, around 70% falls into the oceans and the seas [31]. Taking into account the percentage of usable light falling on the surface, the achievable energy generation for solar technologies is 1600 EJ [32]. These are huge potentials in comparison to other renewable energy technologies, such as wind with 600 EJ and hydropower with 50 EJ [32].

There are two ways with which solar energy can be harnessed to generate electricity. One is solar thermal technology and the second is photovoltaic technology. Solar thermal technology utilizes mirrors spread over a wide area to concentrate an enormous amount of energy at one point to produce temperatures over 500^o C [30]. The thermal energy is used for heating water which changes to steam and is used to move a turbine generator.

Photovoltaic technologies depend on the direct conversion of sunlight to electricity using photovoltaic cells, also known as PV cells or solar cells. The first useful silicon solar cell was developed at Bell Labs in 1954, with a conversion efficiency of 6% [33]. Since then the efficiencies of silicon based solar cells have increased to values ranging between 14% and 26% depending on the manufacturer and model [33]. PV module prices in Europe have dropped by 83% from 2010 to 2017 to a cost price of 0.37 $/W and is predicted to drop to a cost price of 22$/W by 2040 [34]. This is because recent advances in research and a competitive market that have made it possible for the increase in efficiency and reduction in the cost of producing PV modules. This led to a decrease in the cost per unit energy ($/kWh) of a PV system and in some places less or equal to the selling price of electricity from the utility grid.

Photovoltaic systems are being used more nowadays as compared to 15 years ago. As of 2012 the outlines of a global market for solar generated electricity began to emerge. According to an article by Fialka [35], in 2015 nations from all regions reported to the International Energy Agency that for the first time their markets for what is now known as the PV electricity market were growing. The PV electricity market grew by 25% as of 2015 as a result of a stunning drop in prices for solar panels since 2008 (by almost 80%) [1]. According to World Energy Resources 2016, around 1% of the global electricity consumed comes from PV systems. In the near future, it is expected for the costs of PV modules and installation to decrease making photovoltaic technologies an easily affordable and accessible source of energy.

1.2. Working of a solar cell

The working principle of a solar is based on the photovoltaic (PV) effect. The photovoltaic effect is the creation of a potential difference at the junction of two different materials upon exposure to light. The photovoltaic effect was discovered by a French physicist, Alexander Edmond Becquerel in 1839 while experimenting with a solid electrode in an electrolyte solution [36].

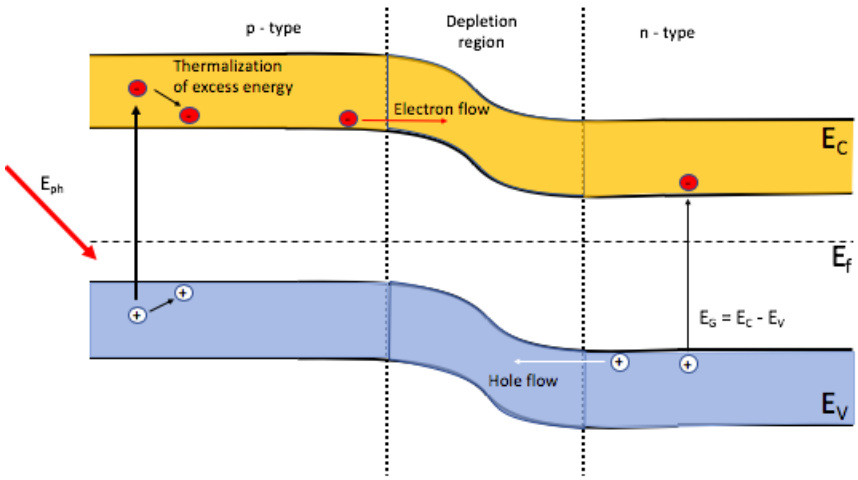

Figure 1.2: Bandgap energy diagram of a solar cell p-n junction.

A bandgap energy diagram of a standard solar cell p-n junction is shown in Figure 1.2. A photon incident on the solar cell, is absorbed by the semiconductor material to generate an electron-hole pair. The electrons in the valence band are excited to the conduction band, provided the energy of the photon is greater than or equal to the bandgap energy of the semiconductor material.

The electrons and holes diffuse towards the n-type and p-type regions, respectively. Some of the charge carriers recombine and release energy in the form of a photon or transfer it to other charge carriers and lattice vibrations. In case the energy of the photon is greater than the bandgap energy, then the excess energy thermalizes in charge-carrier phonon interaction. Photons with an energy less than the bandgap energy are

not absorbed by the semiconductor material. The electrons will flow through an external circuit connected to the electrical contacts of the solar cell. After passing through the circuit, the electrons will reach the p-type semiconductor and recombine with the holes.

1.2.1. Crystalline silicon solar cells

The crystalline silicon lattice structure has a long range order and symmetry with the silicon atoms arranged in a diamond-like configuration. Unlike GaAs and InP which posses a direct bandgap, crystalline silicon has an indirect bandgap. When using an indirect bandgap structure, the charge carriers must change in energy and momentum to be excited form the valence band to the conduction band [36]. Because of the indirect bandgap structure, the absorption coefficient of crystalline silicon is smaller than material that possesses a direct bandgap structure, as we can see in Figure 1.3.

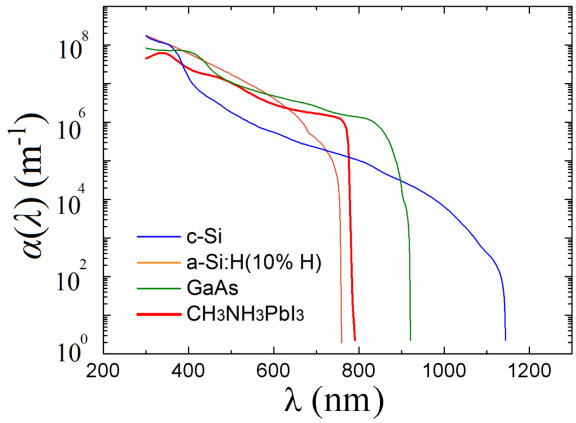

Figure 1.3: The absorption coefficients of c-Si, a-Si:H, GaAs and an organic-inorganic hybrid $CH_3NH_3PbI_3$ perovskite [2].

The application of crystalline silicon as a solar cell has its advantages and disadvantages. The advantages include the abundant supply of raw material, well developed material and device technology, high efficiency and a well established long term solar cell stability. The disadvantage is the small absorption coefficient, which makes it necessary for c-Si based solar cells to have a large material thickness for the absorber layer.

The crystalline silicon wafer used in solar cells are classified based on the defect density in the bulk of silicon: monocrsytalline silicon and polycrystalline silicon. Monocrystalline silicon is a crystalline solid with a continuous lattice without any grain boundaries over the entire bulk structure. Polycrystalline silicon consists of several silicon crystal and are cheaper than monocrystalline silicon.

As of 2017 crystalline silicon based solar cells accounted for 95% of total production, of which 62% is shared by polycrystalline silicon technology [37]. The current world record efficiency for c-Si based solar cells is 26.7%, a hetero-junction interdigitated back contact cell developed by Yoshikawa et al. [38]. Although the cost of producing modules have decreased, module manufacturers are investigating ways to increase the efficiency in an effort to reduce the cost of PV systems further.

1.2.2. Multi-junction solar cells

The maximum conversion efficiency that can be obtained by using a single junction solar cell is given by the Shockley-Queisser limit, as seen in Figure 1.4. The general losses taken into account are the non-absorbed photons below bandgap energy and the thermalized energy of photons that have an energy higher than the bandgap energy. The other losses are because of the voltage losses due to thermal radiation and FF being different from 100% [36]. So, for a single junction solar cell receiving light corresponding to the AM 1.5 spectrum, the limit is about 33.1% efficiency at a bandgap energy of 1.34 eV.

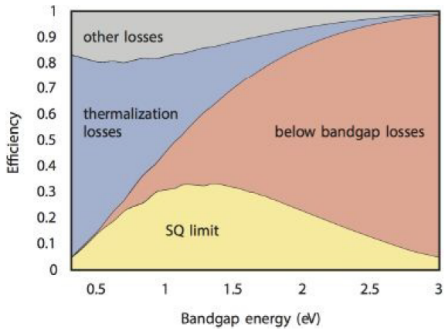

Figure 1.4: The loss mechanisms in the Shockley–Queisser limit [3].

It is important to note that the Shockley-Queisser limit only took into account radiative recombination, hence it was not applicable to c-Si solar cells. This is because crystalline silicon is an indirect bandgap semiconductor and Auger recombination, a non-radiative recombination mechanism is the dominant mode of recombination in these solar cells. Which was why, the SQ limit is usually derived for solar cells with semiconductor materials with direct bandgap such as amorphous silicon, GaAs; etc. Because of their direct bandgap, radiative recombination is the dominant mode of recombination. As for crystalline silicon several attempts were conducted to calculate the efficiency limit and in 2013 a study by Richter et al. [39] derived it to be around 29.43% for single junction c-Si solar cells.

The SQ limit took into consideration only the bandgap energy E_G for deriving the efficiency limit. However, the performance is also strongly influenced by the optical properties of the various components of the solar cell (i.e. the TCO, the p-i-n layers, back contacts, glue; etc) like the complex refractive index, absorbance and even the spectral response of the material to the incident light.

To reduce spectral losses solar cells of different band gaps are stacked on top of one another to absorber light from a larger available spectrum. This is termed as the multi-junction approach. Multi-junction approaches involve the use of two output electrodes. To fabricate multi-junction solar cells, there are two crucial requirements [40]. The first requirement is that the current generated at the maximum power point has to be equal in each component cell and is aptly termed as current matching in tandem cells. The second requirement is the presence of tunnel recombination junctions and they should feature low optical and electrical losses. The solar cells are stacked on a decreasing bandgap order i.e. top cell has the highest bandgap and the bottom cell has the lowest bandgap. This is the basis of multi-junction solar cells; wherein a cell of high bandgap material is added to a solar cell of relatively lower bandgap so as to reduce losses from spectral mismatches.

The solar cells can be used in a four terminal (4T) configuration as in Figure 1.5 . The need for current matching which is needed in multi-junction solar cells no longer poses a problem in the 4T configuration. For example, if a tandem cell has been optimized for AM 1.5G conditions, at dusk or dawn there is relatively more red light in the solar spectrum and this additional fraction will pass through the top-cell and generate increased current in the bottom cell. So in such a case the electrical power that can be delivered to an external load is limited by the top cell. Similarly, when the solar spectrum contains a relatively higher amount of blue light in the solar spectrum such as in cloudy conditions, then the tandem is limited by the bottom cell. In 4T configuration no such restrictions apply, all that is needed is for it to be operated at maximum power point for each of the sub-cells by a tracker and the electrical matching will be optimal [41]. Problems of lattice mismatch can also be discarded when fabricating a 4T solar cell. Each component or cell can be fabricated separately and can be joined by a highly transparent glue to form the main device. Finally, the need for tunnel recombination junctions between the component cells and its further optimization for reducing losses is not needed in 4T solar cells.

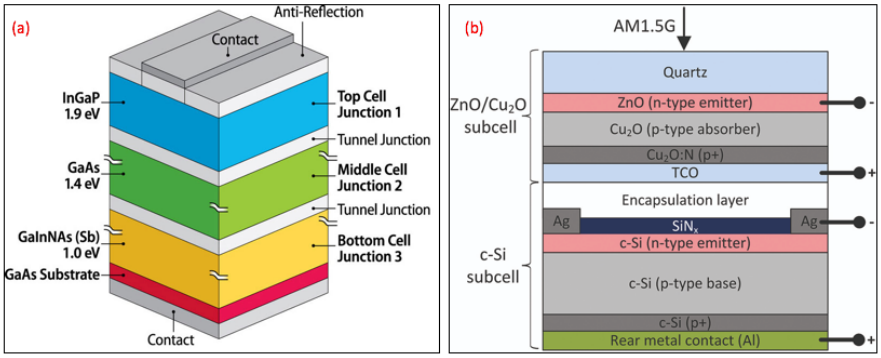

Figure 1.5: (a) A schematic for a multi-junction solar cell [4]. (b) A schematic of a four-terminal solar cell [5].

In 4T solar cells, each solar cell operates at its respective maximum power point. Plus, the cells are optically coupled such that the lower wavelength of the light spectrum is absorbed by the top cells (corresponding to materials with high bandgap energy) and the rest of the light spectrum is utilized by the bottom cell. The properties and potential advantages of a 4T configuration in silicon based solar cells were first explored in detail by Hamakawa [42]. In time Madan [43] analyzed prototype 4T micromorph structures and outlined possible production methods. 4T solar cells have reduced spectral sensitivity and increased energy yield over time as compared to solar cells adopting the multi-junction structure [44]. Hassan [45] from University of Michigan simulated a 4T solar cell with two sub-cells, a GaAs sub-cell and a c-Si subcell with an efficiency of 27.55%.

1.3. Hydrogenated amorphous silicon solar cells

Crystalline silicon is a material that has a rigid three dimensional network having a long range order. The strong covalent bond that each silicon atom has with four other silicon atoms attributes to its rigid network. The term 'amorphous' is commonly applied to materials which do not posses a long range crystalline order. Such materials are non-crystalline in nature because of their small or disorderly variations in their bond angles which eliminates the regular lattice structure. The amorphous silicon structure has dangling bonds. Dangling bonds refers to a valence electron not forming a bond with the valence electron of the neighbouring silicon atom and causes recombination of charge carriers. The differences in the structures are shown in Figure 1.6.

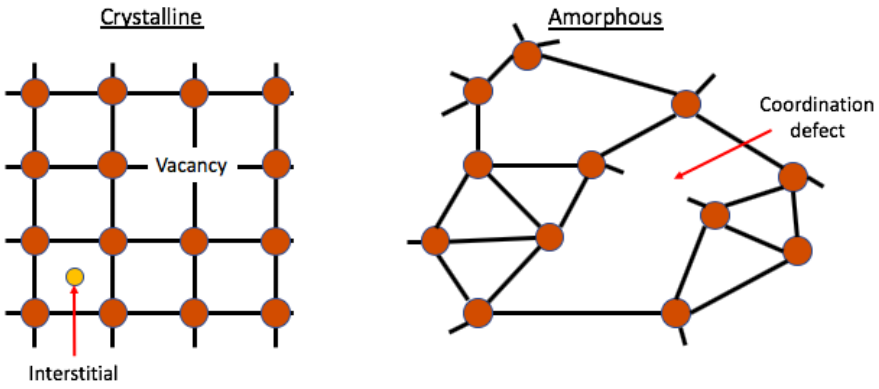

Figure 1.6: An illustration of the structures of crystalline silicon and amorphous silicon.

The first investigation of amorphous silicon deposited from radio frequency glow discharge of silane gas was conducted by Chittik et al. in 1966 [46]. Further work carried out on this material showed that it had a lower density of defects than that of evaporated or sputtered amorphous silicon. The ability to dope amorphous silicon p- and n-type as discovered independently by by Carlson [47] and Spear and LeComber [48]

using the plasma enhanced chemical vapor deposition technique.

Amorphous silicon for use in thin film solar cells is often deposited by a PECVD process and are generally known as hydrogenated amorphous silicon (a-Si:H) thin film. This is because in early studies of amorphous silicon, it was determined that the plasma deposited amorphous silicon contained a significant percentage of hydrogen atoms bonded to the silicon structure [49]. These hydrogen atoms were discovered to be essential to the improvement of the electronic properties of the material [49]. Incorporation of hydrogen into the amorphous silicon network passivates a large fraction of dangling bonds. Unlike crystalline silicon, amorphous silicon has a direct bandgap. This implies that amorphous silicon has higher absorption coefficients and for a given layer of thickness a-Si:H absorbs much more energy than c-Si (about 2.5 times) [50].

In 1977, Staebler and Wronski [51] observed changes in the photoconductivity and dark conductivity of a-Si:H under prolonged exposure. These changes, now commonly known as the Staebler-Wronski effect (SWE) are reversible upon annealing at or above 150^{o}C for a few hours. According to Staebler and Wronski, the defect density is observed to be increasing and stabilizes with increasing illumination time, or 'light soaking'. Because of this effect there is a decline in the efficiency of a-Si:H solar cell during the first few hundred hours under illumination [52]. The discovery of SWE had a critical effect on the development of solar cells by impacting its design and optimization. For instance, the impact of SWE on solar cells can be minimized by implementing active layers to be as thin as possible.

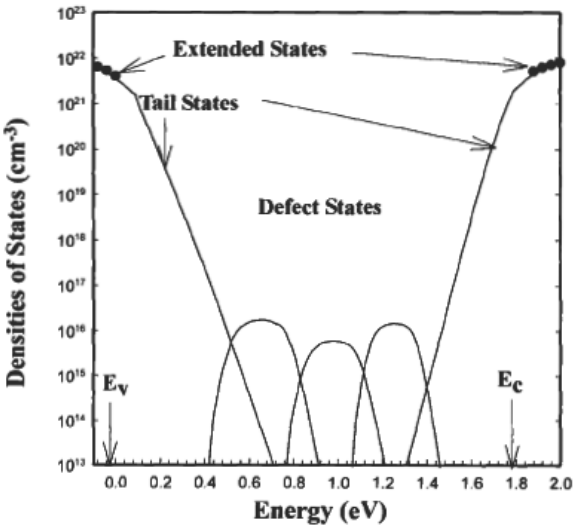

Figure 1.7: A schematic representation of the density of states for hydrogenated amorphous silicon [6].

A knowledge of the density of states (DOS) and the energy distributions in the bandgap of a-Si:H is necessary for a quantitative analysis that describes the role of native and light-induced defects on the optoelectronic properties of the material. A schematic representation of the density of electronic states distribution in a-Si:H is shown in Figure 1.7. The deep lying states or midgap defect states consist of neutral dangling bond defects (D_i) lying around the middle of the bandgap, negatively charged defect states (D_n) lying below the middle of the bandgap and the positively charged defect states (D_p) lying above the middle of the bandgap [53–55]. This is also the basis of the defect pool method used in simulations of solar cells using a-Si:H materials [40]. It is these deep lying defect states that are very important in determining the collection of the photogenerated carriers in solar cells.

Hydrogenated amorphous silicon thin film solar cells make use of a p-i-n or n-i-p structure, which is different from the structure used in conventional c-Si solar cells. An intrinsic layer is added to the conventional p-n structure of c-Si solar cells, because the minority carriers in a doped a-Si:H material have a very low diffusion length and results in a lesser yield of photon generated carriers. The i-layer is usually several hundreds of nanometers thick, while the doped layers are only about 10 - 20 nm thick. Between the p and n- layers a built in electric field is created across the intrinsic absorber layer. Because of this built in electric field, holes move toward the p-layer and the electrons towards the n-layer, as seen in Figure 1.8. Such devices where charge carriers drift under the influence of a built in electric field are called drift devices.

The first result on a-Si:H solar cells was reported by Carlson and Wronski [56] with a conversion efficiency of 2.4% in 1976 and the efficiency increased to 5% soon after [57]. Since then several research groups have

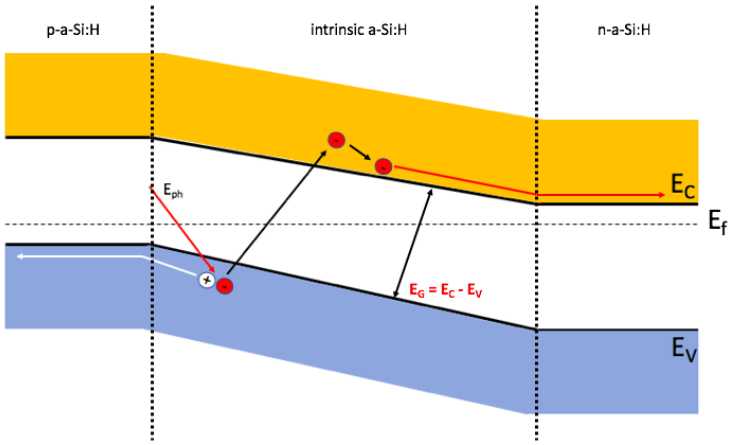

Figure 1.8: Schematic of a bandgap energy diagram of a p-i-n a-Si:H solar cell. The figure shows the generation of an electron-hole pair upon absorbing the energy E_{ph} of a photon. The electron is excited to the conduction band at an energy level E_c. If $E_{ph} > E_G$, a part of the photon energy lost due to thermalization. The electrons move towards the n-layer and the holes to the p-layer.

made continuous efforts to achieve high performance solar cells using p-i-n a-Si:H layers. The highest initial efficiency seen from a single junction a-Si:H solar cells is 12% from Yoshimi et al. [58] in 2003.

1.4. Amorphous silicon oxide solar cells

The bandgap energy and density of states of a-Si:H can be changed by controlling the hydrogen content and by alloying with other elements [59]. The most commonly used elements for alloying are germanium, carbon and oxygen. Narrow bandgap materials are made with a-SiGe$_x$:H, which can reach bandgaps as low as 1.1 eV [60]. Wide bandgap materials are made with a-SiC:H and a-SiO:H, which can reach bandgaps of 2.5 eV. The presence of the elements used for alloying creates new defects. Thus, the transport parameters like mobility and lifetime for alloyed materials are generally lower due to the additional recombination centers [61].

This work focuses on a-SiO$_x$:H solar cells. The bandgap energy of i-a-SiO$_x$:H material can be changed by varying the CO_2 to SiH_4 gas flow ratio. The CO_2 flow required for obtaining a certain bandgap decreases with decreasing deposition pressure and substrate temperature. Kim et al. [62] also reported other ways with which the deposition parameters could be tuned to vary the bandgap energy other than changing just the CO_2 to SiH_4 gas flow ratio, such as the pressure and power. But there are always trade-offs that need to be made, as at low pressure high energetic ion bombardment can result in film damage and decreasing the substrate temperature can result in a film rich in voids. Both dark conductivity and photoconductivity decrease with increased incorporation of oxygen into the silicon network which as a direct result of increased bandgap.

A major feature of a-SiO$_x$:H solar cells, is their high V_{OC} × FF product. In order to attain a high V_{OC}, a high built in potential V_{bi} across the entire solar cell is needed as the V_{OC} is determined by the upper limit of the V_{bi} [62]. The various options to increase V_{bi} as seen from literature [62] are to :

1. Increase mobility bandgap (E_g).
2. Decrease activation energy (E_a) of doped layers.
3. Having low contact energy barriers between TCO - p and -n layers (implementing AZO instead of ITO).
4. Decreasing defect density of the intrinsic layer.

The optimized structure developed by Kim et al. [62] for a-SiO$_x$:H solar cells will be utilized in this work as a reference cell. This is because of its high V_{OC} and fill factor product and reasonable J_{SC}. Further details about the reference cell are included in chapter 4.

In another research article from Do Yun Kim et al. [63], in an effort to increase the J_{SC} of the a-SiO:H solar cell, a p-nc-SiO:H layer was used instead of a p-a-SiO:H layer. It was observed that the J_{SC} did increase due to reduced absorption losses in the shorter wavelength, but at the cost of V_{OC}. Afterwards, the n-a-SiO:H layer was replaced with an n-nc-SiO:H layer which has lower n and k values. This resulted in reduced absorption

losses namely reduced plasmonic losses at the n-nc-SiO:H/metal interface and reduced parasitic absorption in the n-nc-SiO:H layer without drop in the V_{OC} x FF product. The cell produced had an efficiency of 8.8%, which is the highest efficiency recorded for a-SiO$_x$:H solar cells.

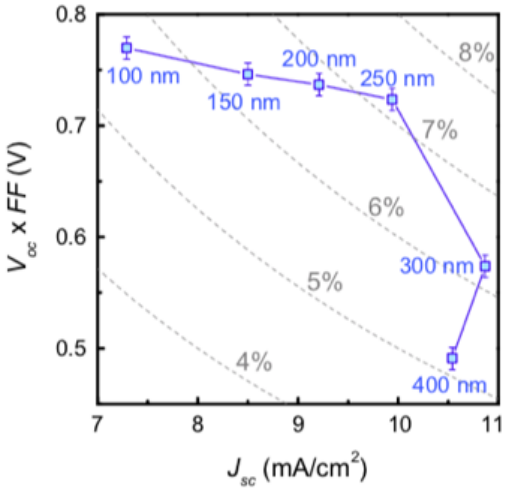

Figure 1.9: V_{OC}× fill factor FF vs. J_{SC} for a-SiO$_x$:H solar cells as a function of i-layer thickness [7].

Kim et al. also observed that as the thickness of the intrinsic layer increases in order to obtain a higher J_{SC}, the V_{OC}× FF product decreases [7]. Also, beyond a certain thickness, the efficiency drops considerably. This trend is observable in Figure 1.9. This implies that the J_{SC} of a-SiO$_x$:H solar cells can only be increased corresponding to a certain absorber layer thickness. Because of its high V_{OC}× FF product and , a-SiO$_x$:H solar cells are suitable candidate for increasing their J_{SC} through bandgap grading.

The use of a-SiO$_x$:H solar cells as a top cell in multi-junction applications have also been reported. An initial efficiency as high as 12.58% for a 3J solar cell with the middle cell being the current limiting cell [7]. Also two other 2J solar cells were developed with an a-SiO$_x$:H cell with efficiencies of 10.25% and 10.92% and was limiting the current for the entire tandem cell structure. [7].

In the case of a four-terminal (4T) solar cell, the gain in Jsc results in more photogenerated carriers collected in the terminals of the top cell. Zhang et al. [64] performed optical simulations and design of a 4T solar cell with a wide bandgap a-SiO:H top cell and a IBC c-Si bottom cell. In the work by Zhang et al. [64], a good analysis between V$_{OC}$× FF product of the top cell and the J$_{SC}$ of the bottom cell was presented and the reduction in reflection losses by implementing pyramid like textures on the glass substrate.

1.5. Thesis objective and outline

The basis of this work conducted is taken from :

1. The development of a high V_{OC}× FF product a-SiO$_x$:H solar cell by Kim et al. [62].
2. Texturing of AZO to enhance the J_{SC} of a-SiO$_x$:H solar cells in the thesis work done by Kavvadas [65].
3. The thesis work done by Rodriguez. Rodriguez showed the effects of changing the grading width of a bandgap energy graded a-SiO$_x$:H solar cell. The bandgap energy was graded in a step wise fashion [18].
4. The thesis work conducted by Chaudhary. Through spectral response calculations, Chaudhary reported an efficiency gain of upto 3.9% could be obtained by utilizing a wide gap a-SiO$_x$:H solar cell in a four terminal mechanically stacked structure with a crystalline silicon bottom cell [9].

Kim et al. developed a high V_{OC}× FF product a-SiO$_x$:H solar cell [62]. Due to the high bandgap energy possessed by the absorber layer of an a-SiO$_x$:H solar cell, the less energetic photons are not absorbed leading to the generation of lesser charge carriers. This is the reason for the lower J_{SC} in comparison to a-Si:H solar cells. There are ways to increase the J_{SC} of the solar cell. One is to increase the absorber layer thickness of the a-SiO$_x$:H solar cells. This was shown by Kim et al. (see Figure 1.9), where the J_{SC} increases with increasing the absorber layer thickness [7]. When increasing J_{SC} by increasing the absorber layer thickness, the V_{OC}×

FF product decreases. After a certain thickness, the efficiency drops dramatically. This implies that the J_{SC} can only be increased upto a certain value and we have to look at other ways to increase the J_{SC} of a-SiO_x:H solar cells.

In the work done by Kavvadas [65], the AZO layer of a-SiO_x:H solar cells are textured in an effort to increase J_{SC}. The J_{SC} shows an increase in J_{SC} from 9.58 mA/cm^2 to 9.69 mA/cm^2, but the rise in J_{SC} was not significant [65].

Another way is to grade bandgap energy to lower values in the absorber layers so as to increase the J_{SC} in hopes that the more lower energetic photons are absorbed in the lower bandgap energy region of absorber layer. This is the main objective of this thesis.

Rodriguez developed graded bandgap energy a-SiO_x:H solar cells for his thesis. In his work, the bandgap energy was graded in a step wise fashion and the cells developed showed an increase in J_{SC} [18]. In this work the bandgap energy will be graded linearly in a single deposition with zero plasma discontinuity during the fabrication process.

Finally, Chaudhary [9] showed a 3.9% increase in efficiency gain for a c-Si based solar cell when placed in a 4T configuration with an a-SiO_x:H solar cell. Chaudhary recommended in his thesis, that a higher response for the top a-SiO_x:H solar cell in the lower wavelength can increase the efficiency gain even further. In this work, the possibility that grading the bandgap energy of the absorber layer can increase the response of the cell at lower wavelength regions of the visible spectrum will also be observed.

In total, the main objective of this thesis is:

To linearly grade the bandgap energy of a-SiO_x:H solar cell in order to increase the J_{SC} of the cell without affecting the high V_{OC} × FF product.

This thesis is structured in a way so as to accomplish this objective. Chapter 2 discusses the sample preparation, deposition procedures used and measurement systems utilized in this work. Chapter 3 gives insight into the history ,possible applications and recent progresses in bandgap grading and the grading method used to linearly grade the bandgap energy in the PECVD setup. Chapter 4 dives into the optimization of the grading width for graded bandgap energy a-SiO_x:H solar cells. Chapter 5 presents the results on the effects of grading the bandgap energy of the a-SiO_x:H cell. It is different from Chapter 4 as it looks into varying thickness and bandgap energy of bandgap graded absorber layer. Chapter 6 dwells into the optical simulations of graded bandgap energy a-SiO_x:H cell using GenPro4 simulation software. Finally, chapter 7 presents the conclusions and recommendations, which includes the major observations and important results in this work and some recommendations for future work.

2

Experimental Methodology

2.1. Introduction

This chapter elaborates on the sample preparation techniques, deposition systems and processes utilized in this work for the development of the graded bandgap energy a-SiO_x:H solar cells. The depositions are undergone in the clean room 10,000 of the Else Kooi Lab, TU Delft. Finally, the characterization setup used to obtain measurements are also detailed. The characterization setups used were carried in EWI/EEMCS , TU Delft.

2.2. Deposition Techniques

2.2.1. Substrate Preparation

Sample preparation is an important task in the fabrication process to produce high quality thin films. This is done to remove any unwanted or residual particles that may be present or stuck to the substrate. Thin film samples were deposited on a 2.5cm × 10cm Coring Eagle XG glass substrate and the solar cells were deposited on an Asahi VU substrate of the same dimensions. The Asahi VU substrate is coated with a textured fluorine doped tin oxide (FTO). First the substrates were dipped into an ultrasonic bath of acetone for 15 minutes, after which the substrates were dried using nitrogen gas. Then the substrates were dipped into an ultrasonic bath of isopropylalcohol (IPA) for another 15 after which they were dried with nitrogen gas. Also the substrate holders were wiped with IPA in order to reduce the inclusion of particles and impurities as much as possible.

2.2.2. Plasma Enhanced Chemical Vapour deposition

Plasma Enhanced Chemical Vapor Deposition (PECVD) is a deposition process where the energy required for the reaction products to deposit onto the substrate comes from the plasma. The deposition processes in a PECVD occur at temperatures lower than those in a standard CVD setup. Deposition is achieved by introducing reactant/precursor gasses between two parallel electrodes - a grounded electrode and a RF energized (13.56 MHz) electrode. The capacitive coupling between the parallel plate electrodes excites the precursor gasses into a plasma - consisting of fractionally ionized gas, electrons and radicals. In this plasma gas phased chemical reactions take place and some of the reaction products drift in the plasma and diffuse towards the electrode resulting in film growth. The lower temperatures for deposition of thin films are critical in many applications where high temperatures can damage the fabricated device, hence only allowing the use of specific substrates. A schematic of the PECVD system is shown in Figure 2.1.

The amorphous silicon oxide thin films are deposited using three different precursor gasses - silane (SiH_4), hydrogen (H_2), carbon dioxide (CO_2). The doped p- and n-layers were deposited by mixing these gasses with diborane (B_2H_6) and phosphine (PH_3) gasses, respectively.The PECVD system used, called Amigo has 6 deposition chambers and 5 load-lock chambers to place the substrates in. A distance of 1.4 cm is kept between the electrode and the substrate while depositing the p- and i-layers and a distance of 2.1 cm for the n-layers [62]. Also the electrodes in all the deposition chambers had an area of 144 cm^2. The Amigo PECVD system has the following chambers :(1)Load-lock chamber.(2)Transfer chamber.(3)DPC 1 - for p-type layer deposition.(4)DPC 2 - for n-type layer deposition.(5)DPC 3 - intrinsic amorphous layer deposition.(6)DPC 4 - μ-crystalline silicon layer deposition.(7)DPC 5 - a multi-process chamber.(8)DPC 6 - sputtering chamber for

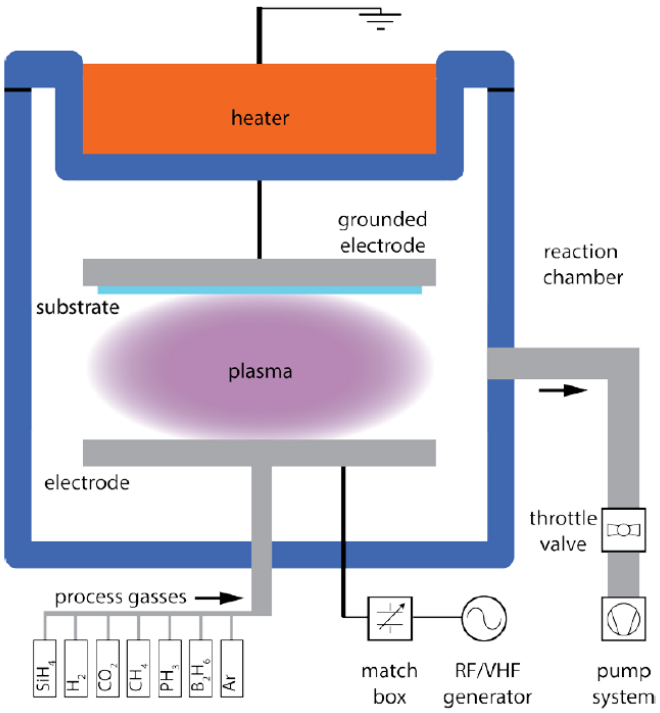

Figure 2.1: A schematic of the PECVD system [8].

AZO layer deposition. These deposition chambers are kept at very low pressures, typically around 0.2 mbar.

2.2.3. RF Magnetron Sputtering

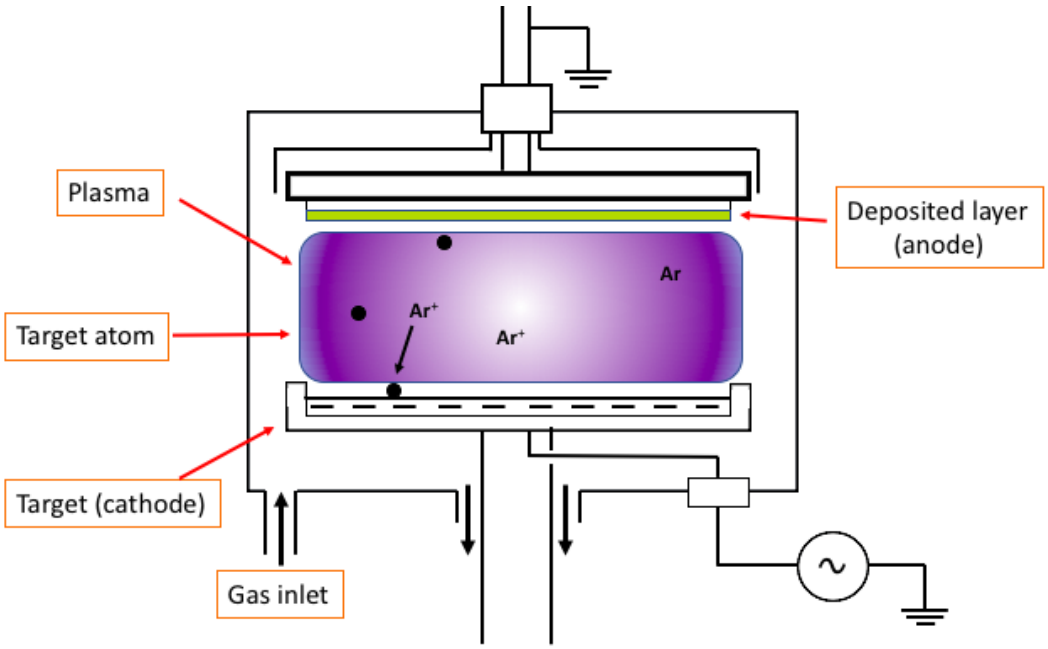

Figure 2.2: A schematic of the RF magnetron sputtering system [9].

RF magnetron sputtering is physical vapour deposition technique where the thin film is deposited using

both plasma and a magnetic field. Magnetrons are a class of cold cathode discharge devices [66]. A plasma is initiated between the cathode and anode by the application of a high voltage from an RF source. The plasma is composed of ionised argon gas which bombard on to the target. The plasma is sustained by the ionisation caused by secondary electrons emitted from the target due to ion bombardment which are accelerated into the plasma. A magnet is place underneath the plasma to provide a magnetic field for better utilization and confinement of secondary electrons leading to much higher plasma yield [66].

A schematic of RF magnetron sputtering is shown in Figure 2.2. AZO was deposited in chamber 6 of the Amigo machine, where A 13.56 MHz AC supplied to a target electrode to generate a magnetic field inside the deposition chamber. A plasma is ignited and charged particles are provided by the argon gas. The argon ions are accelerated towards and bombard a ceramic ZnO/AlO_3 target (98/2 % by weight), resulting AZO particles being released. The AZO particles are then deposited onto a substrate.

2.2.4. Metal Evaporation

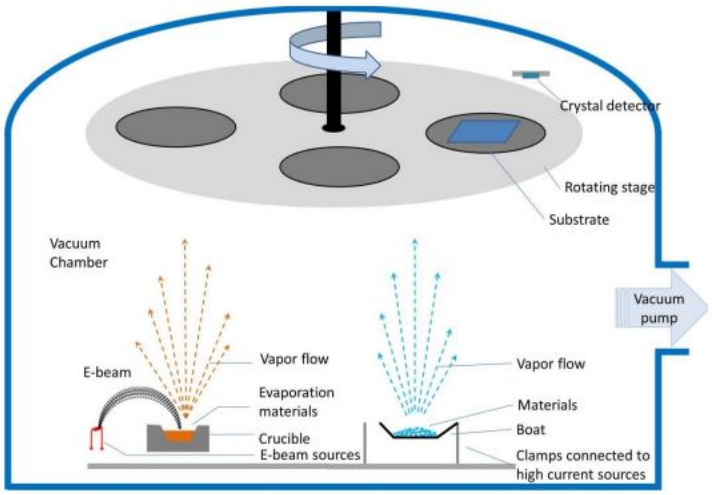

Figure 2.3: A schematic of the Provac PRO500S metal evaporator used in Else Kooi Lab [10].

The deposition of thin metal films for the purpose of contacts for the solar cells and to measure the activation energy (E_a) of doped semiconductor thin films were done on the Provac PRO500S metal evaporator in the Else Kooi Lab. The metal depositions are done at high vacuum, this allows for the metal vapor particles to travel directly onto the substrate. There are two ways in which the metals are evaporated in the Provac metal evaporator, one is thermal evaporation and the other is electron beam evaporation. The difference in both methods is the temperature at which they operate at.

For thermal evaporation, metals with lower melting point such as silver can be used for depositing thin metal films. While in electron beam evaporation, an electron beam is directed to the crucible with the intended metal of higher melting points needed to be deposited. The metals deposited through e-beam are aluminum and chromium. Though Al has a lower melting point, the metal is deposited using e-beam because of the fact that Al can alloy with the tungsten boat when thermal evaporation is used [67]. The vacuum chamber is also equipped with a rotating stage that can hold upto four 10x10 cm^2 substrates or sixteen 2.5x10 cm^2 samples. The stage is rotated at a fixed RPM to allow for uniform deposition across all substrates. A quartz crystal is present in the vacuum chamber with which the exact thickness of the metal thin film is known. The metal evaporator system is depicted in Figure 2.3.

2.3. Characterization Techniques

2.3.1. Spectroscopic Ellipsometry

Ellipsometry is a characterization technique used to determine the thin film thickness and optical constants (n and k). It can also be used to characterize composition, crytallinity, roughness, doping concentration and other properties associated with a change in optical response [11]. The elliposmetery spectrometer used in this work is M-2000DI form J.A. Woollam Co. in the PVMD group.

In ellipsometry a change in polarization is measured as light is reflected or transmitted from a material structure. The polarization change is represented as an amplitude ratio, Ψ and the phase difference, Δ. The measured response depends on the optical properties and thickness of individual materials [11]. The light emitted from the light source and then linealry polarized by a polarizer, after which the linearly polarized light falls onto the sample. the refelcted or transmitted light is then analyzed. Ellipsometry primarily analyzes the change in amplitude and phase of the p- and s- components upon reflection and transmission. The general setup for collecting the ellipsometry data include the following : light source, polarization generator, sample, polarization analyzer and detector [11]. In this work, ellipsometry spectrometer was used to measure the thickness of thin films deposited, the optical bandgap (E_{04}) and obtain the optical constants for use in GenPro otical simulations. The change in polarization measured is illustrated in Figure 2.4.

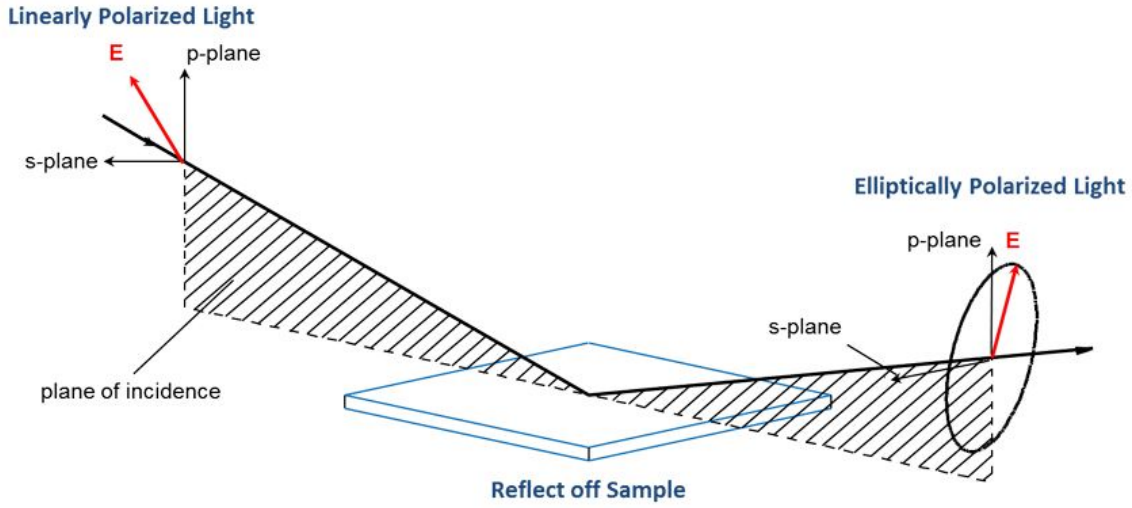

Figure 2.4: An illustration on the change in polarization on linearly polarized upon passing through the sample [11].

2.3.2. Activation Energy Measurements

Activation energy (E_a) is an important parameter, which is used to determine the level of doping in a thin film semiconductor material. The activation energy is the difference between the fermi level and the valence band for a p-type material and the difference between the conduction band and the fermi level for an n-type material. Figure 2.5 shows the bandgap energy diagram of a p- and n-type semiconductor.

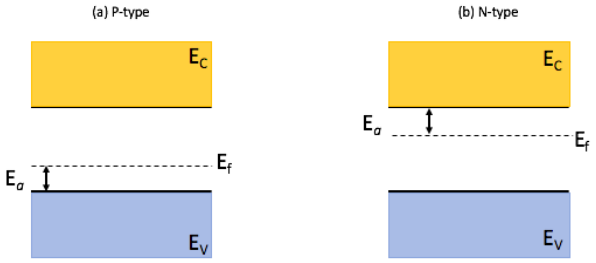

Figure 2.5: A bandgap energy diagram showing the fermi energy and activation energy for : (a) P-type semiconductor; and (b) N-type semiconductor.

The conductivity of semiconductor material is as follows:

$$\sigma = e(\mu_n n + \mu_p p) \tag{2.1}$$

where e is the elementary charge, μ_n and μ_p are the mobility of the electron and hole and n and p are the free electron and hole concentration. The free charge carrier concentration depends on the bandgap energy, activation energy and charge carrier generation due to absorption of light.

For measuring the dark conductivity and activation energy, a doped material is deposited onto a glass substrate. Then coplanar aluminum contacts are evaporated on top of the thin film material. The sample is placed on a thermal controller and is connected to a Keithley 6517A electrometer. The conductance of the layer was measured in dark so as to avoid any photogenerated carriers. The conductance was measured after annealing the thin film material at 130^o for 30 minutes. The temperature dependent dark conductivity (σ_D) is given by Equation 2.2.

$$\sigma_D(T) = \frac{1}{R} \cdot \frac{d}{tL} = \frac{I}{V} \cdot \frac{d}{tL} \tag{2.2}$$

Here R is the resistance of the thin film layer, which is in turn dependent on the current I and voltage V. d is the the distance between the metal contacts, t the film thickness and L the length of the metal contact. The activation energy of the layer was obtained by fitting the $\sigma_D(T)$ and $1/kT$ plot. This plot is known as the Arrhenius plot and is given by equation Equation 2.3.

$$\sigma_D(T) = \sigma_0 \cdot e^{-E_a/kT} \tag{2.3}$$

Where E_a is the activation energy, T is the temperature, k is the Boltzmann's constant and σ_0 is the conductivity pre-factor [68]. The slope of the linear fit Arrhenius plot gives the activation energy of the doped layers.

2.3.3. Illuminated Current Density-Voltage (J-V) Measurement

The current density - voltage curve is a characteristic of solar cells. The J-V curve is measured under standard test conditions. A temperature of 25^{o}C and an irradiance of 1000 W/m^2, A.M 1.5 spectrum is used to obtain the electrical parameters of the solar cell. In this work, the Wacom WXS-156S-L2 solar simulator was used to obtain the J-V curves for the solar cells. A cooling system is fitted within the system so as to maintain a temperature of 25^{o}C during the measurement. The solar simulator is equipped with a halogen lamp and a xenon lamp to simulate the A.M 1.5 spectrum. Electrical parameters such as the V_{OC}, J_{SC}, fill factor (FF), efficiency, series resistance (R_s) and shunt resistance (R_{sh}).

2.3.4. External Quantum Efficiency (EQE) Measurement

External quantum efficiency is parameter that describes how many charge carriers are delivered per photon absorbed. It can be defined as the ratio of charge carriers collected by the solar cell to the number of photons incident on the solar cell. To measure the EQE, the current derived from the solar cell at short-circuit conditions is divided by the elementary charge which is then divided by the total number of incident photons of a given wavelength. The J_{SC} can be calculated by multiplying the photon flux ($\phi(\lambda)$) as a function wavelength to the EQE of the cell measured under short circuit conditions and is mathematically expressed as,

$$J_{SC} = -\int_{\lambda_{min}}^{\lambda_{max}} \phi(\lambda) \cdot EQE(\lambda)_{cell} \cdot e \cdot d\lambda \tag{2.4}$$

Here e is the elecronic charge.

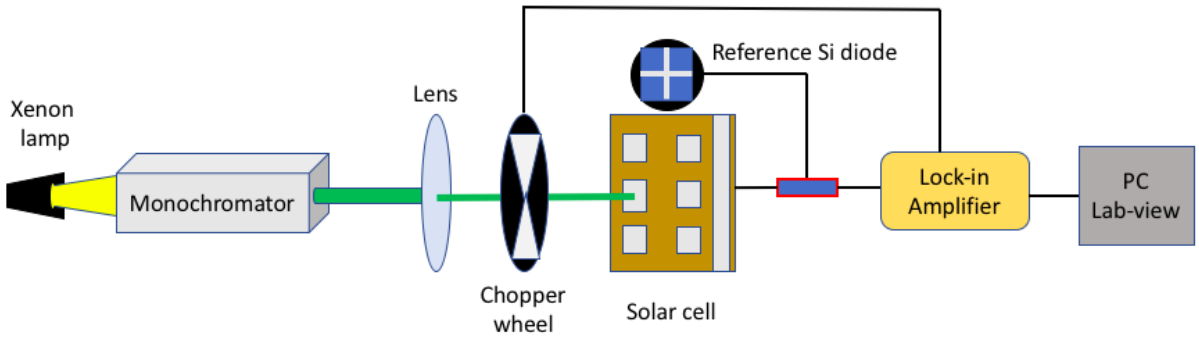

Figure 2.6: In house EQE measurement setup.

The EQE measurement system were designed and built in the PVMD group, TU Delft. The light source is a broad band xenon lamp and a monochromator selectively filters out light of a specific wavelength which is directed onto the solar cells by using lens and mirrors. The measurement beam is chopped at 123 Hz to provide a periodic signal, which is coupled to a lock-in amplifier. The lock-in amplifier is used to improve the signal-to-noise ratio. The EQE is measured in steps for every 10 nm and for each step a calibration step is performed before and after each measurement with a reference silicon diode. The signals are received and analyzed by the computer where the EQE plot is processed.

2.3.5. Reflectance and Transmittance Measurement

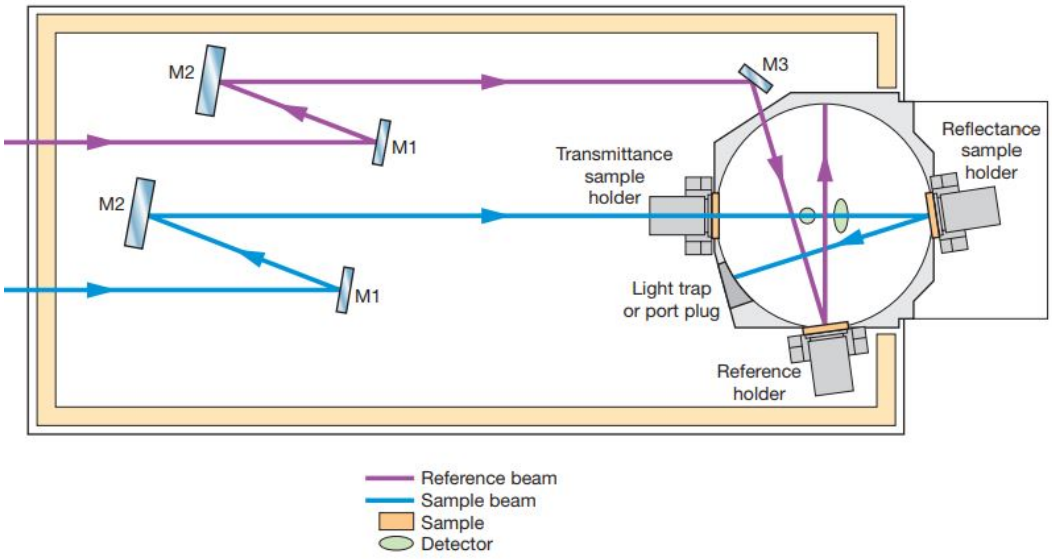

Figure 2.7: A schematic of the Lambda 950 fitted with an Integrating sphere accessory used in this work [12].

A spectrophotometer is used for obtaining the optical properties such as reflectance, transmittance and angular intensity distribution (AID) of the films that are developed. In this work, a Perkin Elmer Lambda 950 spectrophotometer is used to measure the reflectance and transmittance of the solar cells over a spectral range of 300 - 1200 nm.

The spectrophotometer utilizes a deuterium arc lamp and a halogen lamp for visible and infrared light. The instrument is fitted with an integrating sphere accessory for a photodiode detector. An integrating sphere used in a combination with a spectrophotometer can give high precision reflectance (R) and transmission (T) measurement [12]. The absorbance (A) of a thin film can be calculated using Equation 2.5. The sphere has a diameter of 150 mm and is coated with a highly reflective and scattering coating. The coating effectively takes the incident beam and spreads it evenly throughout the sphere making the light homogeneous [69]. The optical design of a 150 mm integrating sphere is shown in Figure 2.7.

$$A = 100 - (R + T) \tag{2.5}$$

2.3.6. Calculation of Efficiency

The solar cells were deposited in a p-i-n fashion onto a Asahi VU substrate of dimensions 10 cm×2.5 cm. Each substrate consisted of thirty solar cells with an area of 4×4 mm^2. In this work, the mean values for the V_{OC}, J_{SC} and fill factor of the ten best performing cells are included in the results. The results are presented with plots showing the error bars determined from calculating the standard deviations from the values obtained. The efficiency was calculated using the J_{SC} calculated from EQE measuring system and not the WACOM solar simulator. In the EQE setup, the illuminated area incident on the cell roughly equals the area of the cell, unlike in the Wacom setup where the illuminated area is much larger. Because of this the photon flux calculated by means of a reference cell is more accurate than that calculated by the Wacom setup, hence giving an accurate measurement for the J_{SC}. The final efficiency was calculated using Equation 2.6.

$$\eta(\%) = \frac{V_{OC} \cdot J_{SC} \cdot FF}{P_{in}} \cdot 100\% \tag{2.6}$$

For the efficiency alone, the error was calculated by taking into account the propagation of error. Here, the standard deviations of the three parameters used to calculate the efficiency are combined to give the standard deviation in the values of the efficiency obtained. This is represented in Equation 2.7 [70].

$$\sigma_\eta = \eta \cdot \sqrt{\left(\frac{\sigma_{V_{OC}}}{V_{OC}}\right)^2 + \left(\frac{\sigma_{J_{SC}}}{J_{SC}}\right)^2 + \left(\frac{\sigma_{FF}}{FF}\right)^2} \tag{2.7}$$

3

Grading bandgap energy and grading method

3.1. Introduction

In this chapter the concept and history of grading the bandgap energy will be introduced. We will look at how the parameters needed for grading the bandgap energy such as, the deposition rate, bandgap energy and flow ratio are related to one and other. Using these relations, a grading method for depositing graded bandgap layers will be derived and introduced in this chapter. Finally, an example on grading the bandgap energy of a 100 nm thick i-a-SiO_x:H layer using the grading method will be explained in detail.

3.2. Bandgap Grading on Solar Cells

Grading the bandgap of a solar cell means that the bandgap energy of the absorber layer is continuously varied by continuously varying the material properties. The electrical conduction and photovoltaic effect of semiconductors with graded bandgap energies has been of interest to researchers since the 1960s. In 1962, Emtage [71] performed calculations and found that an efficiency of 35% could be attained for solar cells with graded bandgap under direct sunlight, if certain requirements are met.The requirements are; (1) the lesser bandgap must be near 0.7 eV and the greater bandgap near 2.5 eV; (2) the minority carrier lifetime must be in the order of 10^{-3} to 10^{-4} sec; and (3) the mobility ratio (ratio of free electron concentration to free hole concentration) must be greater than 10 [71]. Graded bandgap solar cells are not only of research interests, but are also of interest for radiation hardened devices. The graded bandgap region provides an effective field which enhances the collection of charge carriers, even after carrier lifetimes are reduced as a result of radiation damage [16].

A thin film solar cell with an uniform or flat bandgap energy throughout the entire intrinsic layer results in a typical bandgap diagram as was shown in Figure 1.8. To operate the cell at maximum power, it is forward biased to a point near the V_{OC}. This means that in order to boost the power output of the solar cell closer to the ideal point, the fill factor needs to be increased while keeping V_{OC}, as a high as possible. To increase the V_{OC}, the built in voltage V_{bi} needs to be increased.

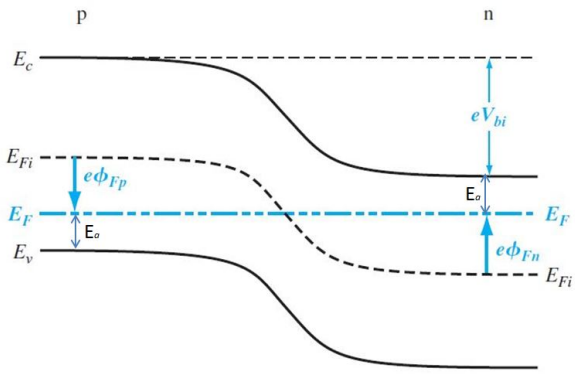

Figure 3.1: Energy bandgap of a p-n junction in thermal equilibrium [13].

The V_{bi} is the maximum obtainable V_{OC} in a solar cell. A schematic depicting the V_{bi} in a pn junction under equilibrium conditions is shown in Figure 3.1. Simply put, the V_{bi} is the electrostatic potential difference arising as a result of the junction formation [72]. Under illumination, the equilibrium condition is broken and a lot of carriers are induced in the p- and n-type semiconductor. A photovoltage (V_{OC}) is induced and kinetic equilibrium is established [72]. The V_{OC} is the difference in the fermi levels at the quasi-neutral regions of the pn junction, when under illumination conditions.

Increasing the bandgap energy of the intrinsic layer at the p-i interface increases the V_{bi}, but wide bandgap materials have lower absorption coefficients. Therefore, the bandgap energy can be graded to lower values for the rest of intrinsic layer.

Konagai et al. [14] at Tokyo Institute of Technology presented their work on GaAs solar cells with a graded bandgap energy in 1975. They found that the surface recombination velocity was high for GaAs solar cells without bandgap grading, which limited any improvements on the efficiency of GaAs solar cells. To counter this, a GaAs solar cell was proposed where the bandgap energy was increased towards the surface (1.43 eV to 1.73 eV). The bandgap energy was graded by increasing the amount of Al diffused into a Ga melt. A figure showing the bandgap energy diagram of the GaAs solar cell is shown in Figure 3.2. A theoretical study was also conducted that showed increased spectral response at shorter wavelengths and electric fields producing a collection efficiency two times larger than that of an abrupt heterojunction solar cells with surface recombination velocities in the range of 10^6 and 10^7. The device so fabricated showed an efficiency of 14%.

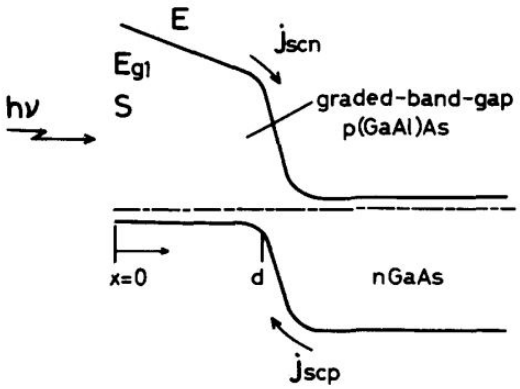

Figure 3.2: bandgap energy diagram for the GaAs solar cell with a graded bandgap energy as reported by konagai et al. [14].

Guha et al. [15] showed through computer simulations the benefits of grading the bandgap energy of the intrinsic layer of an a-SiGe:H solar cell. In their work grading profiles such as normal profiling, reverse profiling were proposed as shown in Figure 3.3. It was observed that when implementing a normal profiling to the intrinsic layer, the V_{OC} and the fill factor of the a-SiGe:H solar cell increased while keeping grading width minimal. On implementing a reverse profile, the V_{OC} of the cell increased even more than the cell with

the normal profiling. The increase in V_{OC} is attributed by the lower value of dark saturation current, J_0 in the graded interface cells indicating less leakage currents at the p-i interface [73]. The improvement in the fill factor is attributed to the higher electric field in the device as a result of bandgap grading.

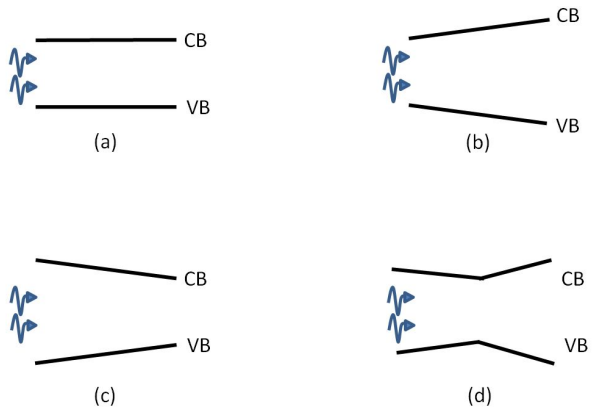

Figure 3.3: Different grading profiles schemes (a) no profiling (b) normal profiling (c) reverse profiling (d) double profiling [15].

Zimmer et al. [74] also showed through computer simulation on how varying the grading width of the p-i interface affected electrical and optical properties of an a-SiGe:H solar cell. Zimmer at al. showed that by having a small grading width, the the positively charged defects at the front of the cell enhances the electric field and transport of charge carriers in the middle and the rear parts of the cell. Also the cells with a smaller p-i grading width showed a higher generation/recombination ratio was observed for small voltages of forward bias indicating good extraction of photogenerated carriers unlike a cell with a large p-i grading width which possess higher recombination.

The findings of Zimmer et al. were further investigated by Folsch et al. [75] and arrived at the same conclusion. Conde et al. [76] showed how the mobility-lifetime product of electrons and holes were enhanced through compositional grading of the bandgap of a a-SiGe:H solar cell. The $\mu\tau$ values observed were higher than that in bulk alloys with the same optical bandgap. Van Swaaij et al. [77] showed the performance dependence of grading width on the a-SiGe:H solar cell. Both experimental and computer simulations were used to explain the observations. It was found that in order to obtain high efficiency amorphous silicon germanium solar cells, the p-i grading width needs to be kept as small as possible to improve the V_{OC} and fill factor and making the i-n grading width as wide as possible.

Using the information provided from articles published by the authors referred to in this section, Hsu et al. [78] published a research article on the effects of graded bandgap absorber on the performance of a a-SiGe:H solar cell. The bandgap grading was accomplished by varying the germanium content in the intrinsic layer of the a-SiGe:H solar cell. It was observed that by having a 20 nm thin graded layer at the p-i interface of the intrinsic layer of the a-SiGe:H solar cell, the V_{oc} improved and also implementing a 160 nm thick graded layer at the i-n interface of the intrinsic layer improved all the parameters including the efficiency by about 25%.

Bandgap grading was also implemented to other types of thin film solar cells. For instance, Morales [79] showed that increasing the bandgap variation over a graded layer promoted the drift-diffusion length of the charge carriers in a CIGS solar cell. Morales showed this not only experimentally, but also theoretically. The equations derived for the internal electric field associated to bandgap energy grading, showed that the electrons will drift due to the potential variation and by the quasi-electrostatic field associated with the affinity (conduction band) variation with position. This field reduces the back surface recombination at the ohmic contact and the bulk recombination typically characterized by the diffusion length [79] and also helps in the separation of photogenerated electron-hole pairs [80].

Olsen [16] observed high photoresponse and photocurrent generated in $Al_xGa_{1-x}As$ solar cells with a graded bandgap energy profile. It also exhibited an AM 1 efficiency of 21.5% which was declared one of the best results obtained for a graded bandgap energy solar cell in 1990 by the Solar Energy Research Institute. A figure of the graded bandgap energy of the $Al_xGa_{1-x}As$ solar cell is shown in Figure 3.4.

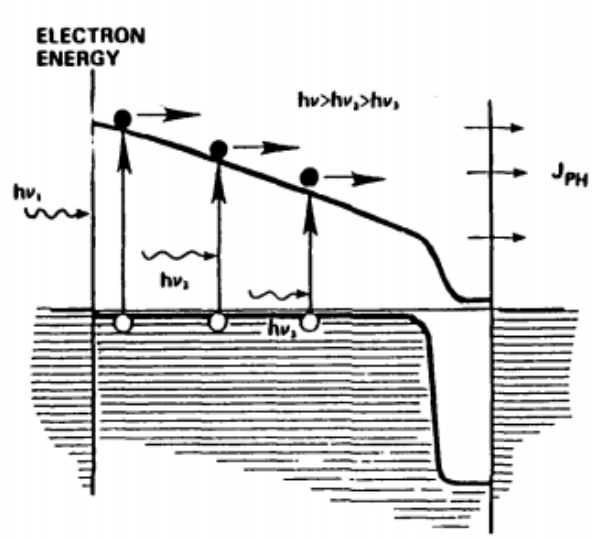

Figure 3.4: Schematic of the graded bandgap energy of the $Al_xGa_{1-x}As$ solar cell as shown by Olsen [16].

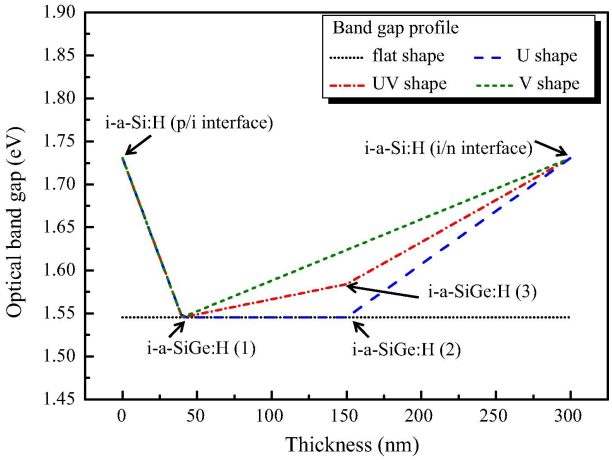

Figure 3.5: Schematic of the graded bandgap energy of a-SiGe:H solar cells showcasing several grading profile schemes [17].

Though the effects of grading a bandgap seem promising, Lundszien et al. [81] [82] showed experimentally that replacing the graded bandgap region of an a-SiGe:H solar cell with a buffer layer with a constant intermediate bandgap to have almost similar results. But there is a slight improvement (around 2% increase) in the performance of the graded bandgap solar cell over a solar cell including a buffer layer with constant intermediate bandgap. The effects of graded bandgap are not yet fully understood as few authors propose the need to grade the entire absorber layer (V type) as a pre-requisite to obtain high-efficiency solar cells. While other authors prefer grading the bandgap at the p-i and i-n interface (U type). Krajangsang et al. [17] proposed another type of graded profiling known as the VU type shown in Figure 3.5, a mix of V and U type profiling which showed significant improvements on the V_{OC} and fill factor over the V and U type profiled a-SiGe:H solar cells. The performance of a V and U type grading profile on the a-SiO_x:H solar cells will also be investigated in this work. There are research articles which also present solar cells with graded bandgap using nano-rod absorber material as next generation solar cells [83].

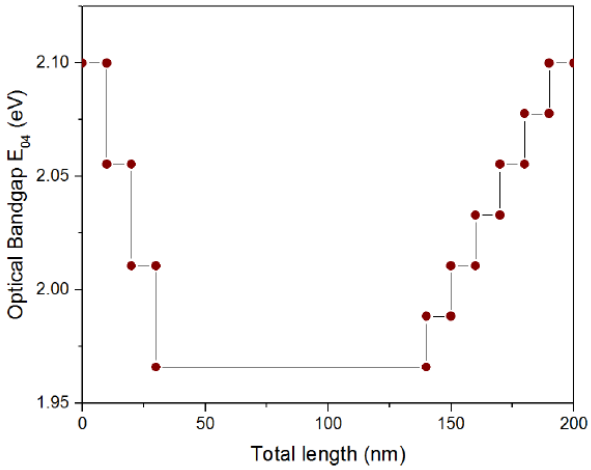

Figure 3.6: Bandgap energy at various thickness of the intrinsic layer of an a-SiO_x:H solar cell as developed by Mario Rodriguez [18].

Rodriguez [18] performed various experiments in regard to the fabrication of a-SiO_x:H solar cells with graded bandgap energies at TU Delft as part of his Mater's thesis. In his work, the bandgap energies were varied for every 10 nm for the desired bandgap energy and grading width. The bandgap energy was varied from 2.1 eV to 1.96 eV as shown in Figure 3.6. This meant that each region with a specific bandgap energy was a separate deposition process, possibly leading to more interface defects between each graded layer. It was reported that the J_{SC} of the best performing graded bandgap solar cell was around 1 mA/cm^2 higher than that of the reference cell used in his work and will also be used for reference in this work. He concluded that the photocurrent density and efficiency can be increased by grading the bandgap over a small width of the intrinsic absorber layer at both the p-i region and the i-n region. Further investigations into the topic of graded bandgap solar cells is needed.

3.3. Grading method

In this section the method for grading the bandgap energy for the intrinsic a-SiO_x:H layer for the solar cells developed. Unlike the work of Rodriguez [18], where in the bandgap energy was graded for every 10 nm, in this work the bandgap energy is graded continuously to the desired width. In this work the optical bandgap, E_{04} is utilized and obtained from spectroscopic ellipsometry. Figures 3.6 and 3.7 show the dependency of the optical bandgap energy and deposition rate on the gas flow ratio r. In this work the gas flow ratio r is defined as shown in Equation 3.1:

$$r = \frac{[CO_2]}{[SiH_4]} \tag{3.1}$$

Figure 3.9 shows the desired bandgap energy grading profile over a grading width of d_G. It can be seen that the optical bandgap increases with increasing flow ratio and the deposition rate decreases with increasing flow ratio.The data points in Figure 3.7 and Figure 3.8 are fitted linearly to obtain a line equation. These are shown in Equation 3.2, Equation 3.3 and Equation 3.4

$$E_{04}(r) = A \cdot r + E_{04}(0) \tag{3.2}$$

$$v_{dep}(r) = B \cdot r + v_{dep}(0) \tag{3.3}$$

$$E_{04}(x) = C.x + E_{04}(0) \tag{3.4}$$

where,

E_{04}**:** The optical bandgap energy in eV.

r**:** The gas flow ratio during deposition of the intrinsic layer. As seen in Equation 3.1, it is ratio between the CO_2 flow and SiH_4 flow.

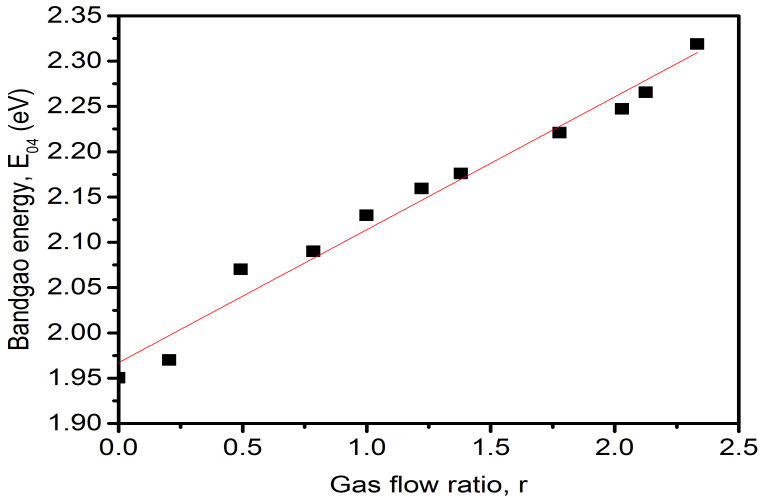

Figure 3.7: Optical bandgap energy for increasing flow ratio r.

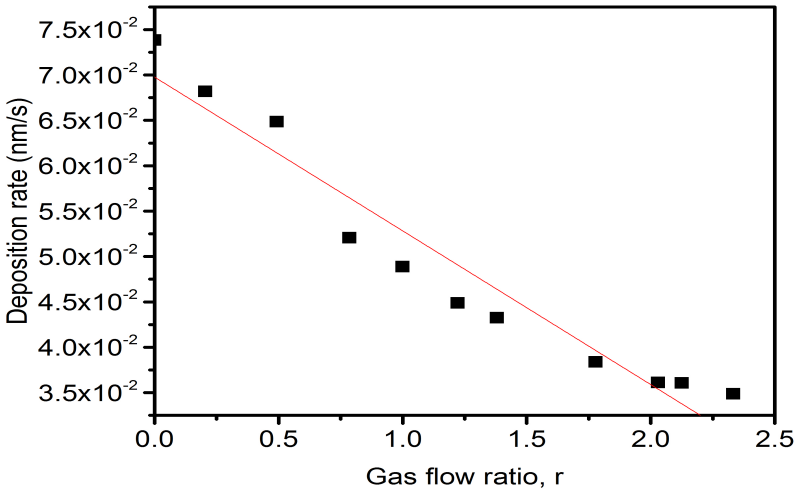

Figure 3.8: Deposition rate for increasing flow ratio.

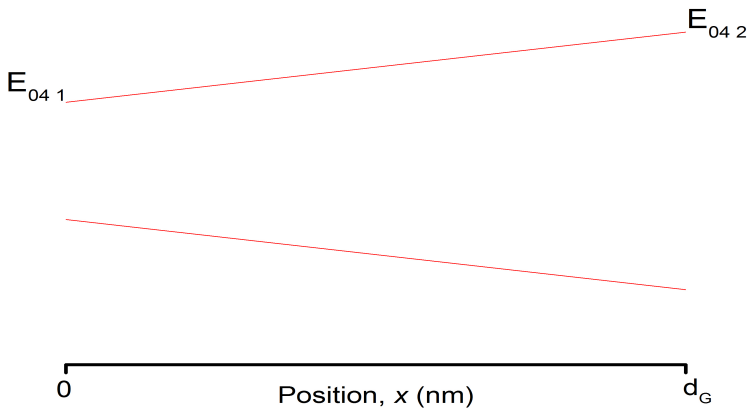

Figure 3.9: desired bandgap energy profile over grading width d_G of the intrinsic a-SiO$_x$ layer.

v_{dep}**:** The deposition rate in nm/s.

x**:** The position with respect to the grading width d_G.

A**:** The change in bandgap energy E_{04} for the change in flow ratio r as seen by linear fit trendline in Figure 3.7. It has a numerical value of 0.147 ± 0.007 eV.

B**:** The change in deposition rate v_{dep} for change in flow ratio r as seen by the linear fit trendline in Figure 3.8. It has a numerical value of -0.017 ± 1.47 · 0.002 nm/s.

C**:** The change in bandgap energy from E_{04_1} to E_{04_2} with change in intrinsic layer position x over grading width d_G as seen in Figure 3.9. C has a numerical value of $1.4 \cdot 10^{-3}$ eV.

$E_{04}(0)$**:** Initial optical bandgap energy in eV.

$v_{dep}(0)$**:** Initial deposition rate in nm/sec. It has a numerical value of $6.98 \cdot 10^{-2}$ nm/s.

In order to continuously vary the bandgap energy over a certain grading width, the gas flow ratio r needs to obtained as a function of time. This is done by obtaining the time derivative of Equation 3.4. This gives Equation 3.5:

$$\frac{dE_{04}(x,t)}{dt} = C \cdot \frac{dx}{dt} \tag{3.5}$$

$$\Rightarrow dE_{04}(x,t) = C \cdot v_{dep}(r(g(t))) \cdot dt \tag{3.6}$$

Here $r(g(t))$ is the gas flow ratio as a composite function of time. Meaning that the gas flow ratio depends on some function $g(t)$, which is not known. Upon integrating Equation 3.6, we obtain;

$$\int_{E_{041}}^{E_{042}} dE_{04} = C \cdot \int_{t1}^{t2} v_{dep}(r(g(t))) \cdot dt \tag{3.7}$$

Substituting Equation 3.3 into Equation 3.7.

$$(E_{04_2} - E_{04_1}) = C \cdot \int_{t1}^{t2} [v_{dep}(0) + B \cdot r(g(t))] \cdot dt \tag{3.8}$$

The composite function $r(g(t))$ is integrated in Equation 3.9. While integrating composite functions, the outer function $r(t)$ is integrated as is and the inner function $g(t)$ is differentiated to a constant, in this case G also unknown (as $g(t)$ is not known).

$$\Rightarrow \left(\frac{E_{04_2} - E_{04_1}}{C}\right) = v_{dep}(0)[t_2 - t_1] + B \cdot \left(\frac{r^2(t)}{2}\right)_{t1}^{t2} \cdot G \tag{3.9}$$

We get,

$$\Rightarrow r(t) = \sqrt{\left(\frac{2}{B \cdot G}\right)\left[\frac{E_{04_2} - E_{04_1}}{C}\right] - v_{dep}(0)[t_2 - t_1] + r^2(t_1)} \tag{3.10}$$

Equation 3.10 is the equation with which the flow ratio at a certain deposition time is needed to acquire the needed bandgap at position x of the graded bandgap layer. But an unknown constant G obtained from the integration of $r(g(t))$ is present in Equation 3.10. For this Equation 3.10 needs to be further simplified to remove G. This can be done by taking a part of Equation 3.10 and substituting that term as $K \cdot t$ as shown in

$$K \cdot t = \left(\frac{2}{B \cdot G(t)}\right)\left[\frac{E_{04_2} - E_{04_1}}{C}\right] - v_{dep}(0)[t_2 - t_1] \tag{3.11}$$

Here, $t \rightarrow (0, t_2)$ is the deposition time and t_2 is the final deposition time at which the flow ratio $r(t_2)$ has attained the desired final bandgap energy. t_2 can be calculated from

$$t_2 = \frac{x}{v_{dep}(0)} \tag{3.12}$$

Equation 3.13 is a line equation with K being the slope of the line for the change in flow ratio from $r(t_1)$ to $r(t_2)$ over a deposition time of t_2. An example is shown in the next section on how K is obtained and the gas flow ratio over the entire deposition process using Equation 3.13. The final equation needed to obtain the flow ratio at a certain deposition time can be obtained from

$$r(t) = \sqrt{K \cdot t + r^2(t_1)}; t \rightarrow (0, t_2) \tag{3.13}$$

3.4. Example for grading the bandgap energy for a 100 nm i-a-SiO$_x$:H layer

This section is to show how the flow ratio profile is obtained using the equations presented in the previous section for grading the bandgap energy of an i-a-SiO$_x$:H layer from 1.96 eV to 2.1 eV over a thickness of 100 nm. The resulting layer will have bandgap energy grading as seen in Figure 3.9.

Firstly, the figures showing the dependencies of the E_{04} and v_{dep} (Figure 3.7 and Figure 3.8) are fitted in a 2nd degree polynomial curve for obtaining more accurate values of the deposition rate and optical bandgap energy. The poly-fit equations are shown below :

For obtaining the E_{04} by using the flow ratio r :

$$E_{04}(r) = -1.81 \cdot 10^{-2} \cdot r^2 + 0.1895 \cdot r + 1.9523 \tag{3.14}$$

For obtaining the flow ratio r for the desired E_{04} :

$$r(E_{04}) = 5.0573 \cdot E_{04}^2 - 14.856 \cdot E_{04} + 9.7453 \tag{3.15}$$

For obtaining the deposition rate by using the flow ratio r :

$$v_{dep}(r) = 6.2 \cdot 10^{-3} \cdot r^2 - 3.16 \cdot 10^{-2} \cdot r + 7.49 \cdot 10^{-2} \tag{3.16}$$

The manner with which the flow ratio needs to be varied over deposition time is explained in the following steps:

1. To obtain the flow ratios corresponding to the optical bandgap energy of 1.96 eV at time t_1 and 2.1 eV at time t_2 of the deposition process . On using Equation 3.15 we get :

$$r(1.96 \text{ eV}) = r(t_1) = 5.566 \cdot 10^{-2} \Rightarrow r^2(t_1) = 3.01 \cdot 10^{-3} \tag{3.17}$$

$$r(2.1 \text{ eV}) = r(t_2) = 85.04 \cdot 10^{-2} \Rightarrow r^2(t_1) = 723.17 \cdot 10^{-3} \tag{3.18}$$

2. The total time taken for depositing the 100 nm intrinsic layer with a graded bandgap energy needs to be calculated. For this, the deposition rate corresponding to flow ratio r_{t_1} using Equation 3.16 and the deposition time t_2 is calculated.

$$v_{dep}(r(t_1)) = 7.316 \cdot 10^{-2} \text{ nm/sec} \tag{3.19}$$

$$\Rightarrow t_2 = \frac{100}{v_{dep}(r(t_1))} = 1366.82 \text{ sec} \tag{3.20}$$

3. With the deposition time calculated in the previous step, the parameter K as seen in Equation 3.11 and Equation 3.13 needs to calculated. As interpreted from Equation 3.11 and shown in Figure 3.10, K is the slope between the squared values of $r(t_1)$ and $r(t_2)$ over a deposition time of 1366.82 seconds.

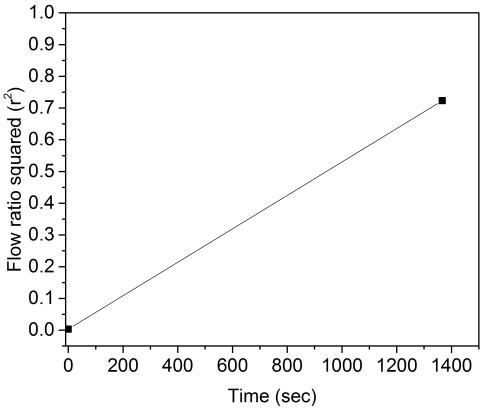

Figure 3.10: Linear relation between the squared values of the flow ratio and deposition time.

We get,

$$K = 5.268 \cdot 10^{-4}\ s^{-1} \tag{3.21}$$

4. This step involves in obtaining the flow ratio profile over the entire deposition process of the graded bandgap energy i-a-SiO$_x$:H layer. This is obtained by by using Equation 3.13. The resulting equation and flow ratio over deposition time are represented in Equation 3.22 and Figure 3.11.

$$r(t) = \sqrt{5.268 \cdot 10^{-4} \cdot t + r^2(t_1)}\ t \rightarrow (0, t_2 = 1366.82 sec) \tag{3.22}$$

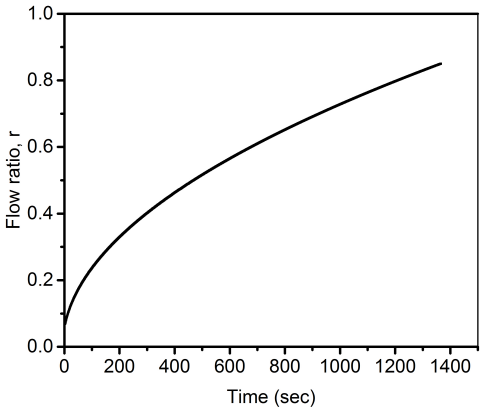

Figure 3.11: Flow ratio profile for depositing the graded bandgap energy i-a-SiO$_x$:H layer.

5. To divide the flow ratio profile shown in Figure 3.11 into several linear steps. This is done because the PECVD system operated cannot manipulate the flows in a manner as shown in the flow ratio profile. The modified flow ratio profile is as shown in Figure 3.12.

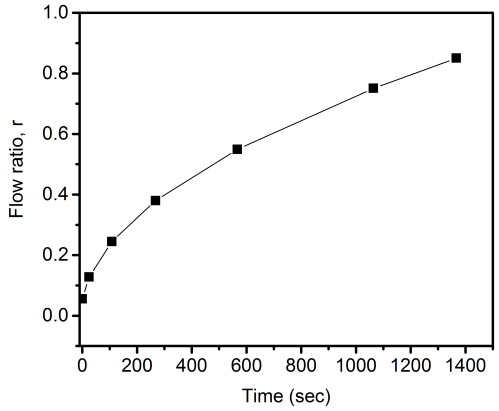

Figure 3.12: Modified flow ratio profile for depositing the graded bandgap energy i-a-SiO_x:H layer.

The 100 nm graded bandgap energy i-a-SiO_x:H layer is deposited in six flow ramping steps. The silane (SiH_4) and carbon-dioxide (CO_2) flows corresponding to $r(t_1)$, i.e the beginning feed for the deposition process are calculated as shown in Equation 3.23 and Equation 3.24. The flows are then individually ramped in steps to obtain the graded bandgap energy layer. These steps are shown in Table 3.1, indicating the SiH_4 and CO_2 flows being ramped to and the time upto which the said ramping takes place to.

$$SiH_4 = \frac{10}{1 - r(t)} \Rightarrow SiH_4 = 9.5 \text{ sccm} \tag{3.23}$$

$$CO_2 = 10 - SiH_4 \Rightarrow CO_2 = 0.5 \text{ sccm} \tag{3.24}$$

Table 3.1: Table showing the several steps in which the individual flows are ramped to in order to attain a graded bandgap energy i-a-SiO_x:H layer

Step no.	Time range (sec)	Time difference (sec)	Flow ratio at the end of the ramping step	[SiH_4] (sccm)	[CO_2] (sccm)
1	0 - 25	26	$12.75 \cdot 10^{-2}$	8.8	1.2
2	25 - 108	83	$24.5 \cdot 10^{-2}$	8	2
3	109 - 268	159	$38 \cdot 10^{-2}$	7.2	2.8
4	268 - 567	299	$54.93 \cdot 10^{-2}$	6.5	3.5
5	567 - 1064	497	$75.07 \cdot 10^{-2}$	5.7	4.3
6	1064 - 1367	303	$85.03 \cdot 10^{-2}$	5.4	4.6

In the fashion as described in the steps above the solar cells with a graded bandgap energy intrinsic layer are fabricated. It also has to be mentioned that while the flows are being ramped during the ramping steps, the plasma is never turned off. The plasma is kept on during the entire deposition process of the graded bandgap energy absorber layer without any interruption.

4

Optimization of grading width for the bandgap energy graded a-SiO_x:H solar cells

4.1. Introduction

This chapter will focus on the fabrication of graded bandgap energy a-SiO_x:H solar cells and its analysis. The cells fabricated incorporate a p-i-n structure. This chapter will concentrate on obtaining an optimal grading width for the solar cells which have a better efficiency or performance than that of the reference cell. The first section gives details on the deposition parameters and electrical parameters obtained from the reference cells used in this work. Then the grading widths at both the p-i and i-n region of the graded bandgap solar cells are optimized with their results presented independently. Finally, the results will compared to that of the reference cell and to the cells developed in the work by Rodriguez [18].

4.2. Reference a-SiO_x:H Solar Cell

The reference cell fabricated is based of the research published by Kim et al. [62]. The reference cell is chosen for its high V_{OC} × FF product. Asahi VU glass substrates were used to deposit the solar cells using PECVD process. The Asahi VU glass substrates used have a thin film layer of SnO_2:F as a transparent conductive oxide layer. Firstly, a 10-nm thick ZnO:Al layer was sputtered onto the Asahi VU glass substrate. This layer is implemented because during the deposition of the p-layer the intense H_2 rich plasma can lead to the formation of oxygen depleted surface regions, also known as Sn precipitation in the SnO_2:F [63]. After the ZnO:Al is sputtered, the solar cell is deposited in a p-i-n structure. The deposition parameters and thickness of the individual layers deposited are shown in Table 4.1 as per deposition sequence.

Table 4.1: Deposition conditions of reference a-SiO_x:H solar cell and the 1.96 eV flat bandgap energy a-SiO_x:H solar cell.

Layer	Thickness (nm)	[SiH_4] (sccm)	[CO_2] (sccm)	[H_2] (sccm)	[B_2H_6] (sccm)	[PH_3] (sccm)	RF Power (W)	RF Power Density (mW/cm^2)	Pressure (mbar)	Temperature (^{o}C)
p-nc-Si	5	1.5		200	30	-	50	347	2.5	300
p-a-SiO_x:H	7	20	45	20	2	-	5	35	0.7	300
i-a–SiO_x:H	10	2.5	2.5	200	-	-	6	42	2.6	200
i-a–SiO_x:H	200	8/9.5*	2/0.5*	200	-	-	3	21	2	200
n-nc–Si:H	5	1	-	100	-	1.2	10	69	1.5	300
n-nc–SiO_x:H	100	1	2	100	-	1.2	10	69	1.5	300

* deposition parameters of the 1.96 eV flat bandgap energy a-SiO_x:H solar cell.

A 300-nm thick strip of aluminium is used as the front contact and the back metal metal contact composed of 150 nm Ag/ 30 nm Cr/ 300 nm Al. The metal contacts were deposited using the Provac metal evaporator. The reference a-SiO_x:H solar has an i-a-SiO_x:H layer with a uniform bandgap energy of 2.02 ± 0.01 eV.

The p-a-SiO$_x$:H layer has a bandgap energy of 2.06 ± 0.03 eV and the n-nc-SiO$_x$:H layer has a bandgap energy of 2.64 ± 0.05 eV. The external parameters of the solar cell and the EQE are shown in Table 4.2 and Figure 4.1 respectively.

Also a solar cell with an absorber layer having a bandgap energy of 1.96 eV has also been fabricated. This cell will be hereby referred to as the 1.96 eV flat bandgap energy cell when comparing the results to that of the graded bandgap energy cells. The cell is same as the reference cell, except for the i-layer which has different SiH_4 and CO_2 gas flows (see Table 4.2). The electrical parameters of the 1.96 eV flat bandgap energy are shown in Table 4.2 and the EQE in Figure 4.1. As it can be seen, the 1.96 eV flat bandgap energy cell has a high value for its J_{SC} and a decent V_{oc} × FF product. The results of the fabricated solar cells with graded bandgap energy are compared to the reference a-SiO$_x$:H cell and the 1.96 eV flat bandgap energy cell to asses the effects of bandgap energy grading.

Table 4.2: External parameters of the Reference a-SiO$_x$:H solar cell and the 1.96 eV flat bandgap energy solar cell.

	V_{oc} (V)	Fill Factor	J_{SC} (mA/cm^2)	Efficiency, (%)
Reference a-SiO$_x$:H cell	0.986 ± 0.003	0.68 ± 0.01	10.84 ± 0.01	7.19 ± 0.17
1.96 eV flat bandgap energy cell	0.948 ± 0.002	0.65 ± 0.01	13.82 ± 0.03	8.52 ± 0.14

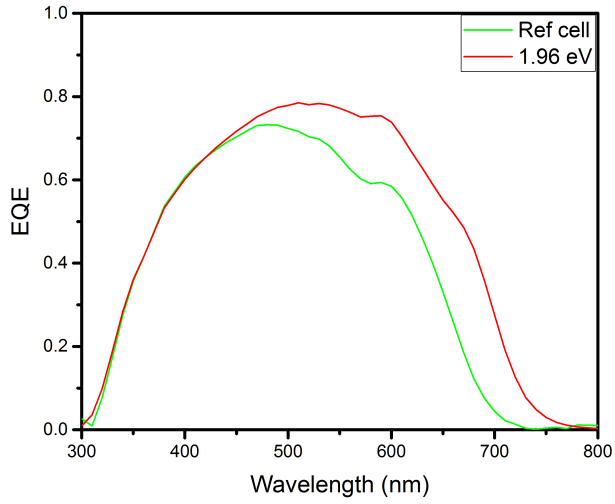

Figure 4.1: EQE of the reference a-SiO$_x$:H solar cell and the 1.96 eV flat bandgap energy solar cell.

4.3. Varying the p-i region grading width

The aim of this experiment is to optimize the grading width for both the p-i region and the i-n region so as to obtain a solar that has a better performance than the reference cell. The first approach is to find a optimum grading width for the p-i region, which is detailed in this section and then finding the optimum grading width for the i-n region which will be focused in the next section.

4.3.1. Experimental details

The approach for finding the optimum grading width is taken from Rodriguez [18]. The solar cell fabricated by Rodriguez had bandgap energies graded from 2.1 eV to 1.96 eV as seen Figure 3.6. This work follows that approach but the bandgap energy is graded linearly across the absorber layer. The p-i region and the i-n region can be described as the region of the absorber layer adjacent to the p-layer and n-layer respectively, this can be seen in Figure 4.2.

The bandgap energy was graded from 2.1 eV to 1.96 eV over a thickness of 100 nm in the i-n region and was not changed while varying the grading width in the p-i region. A schematic diagram depicting the varying

p-i region grading width while the i-n region grading is kept constant at a 100 nm is shown in Figure 4.2. Here, the p-i grading width and the central-i region are both a function of the grading width x in nm. The grading width at the p-i region grading width was varied starting from 10 nm all the way to 100 nm. In all 7 solar cells were fabricated.

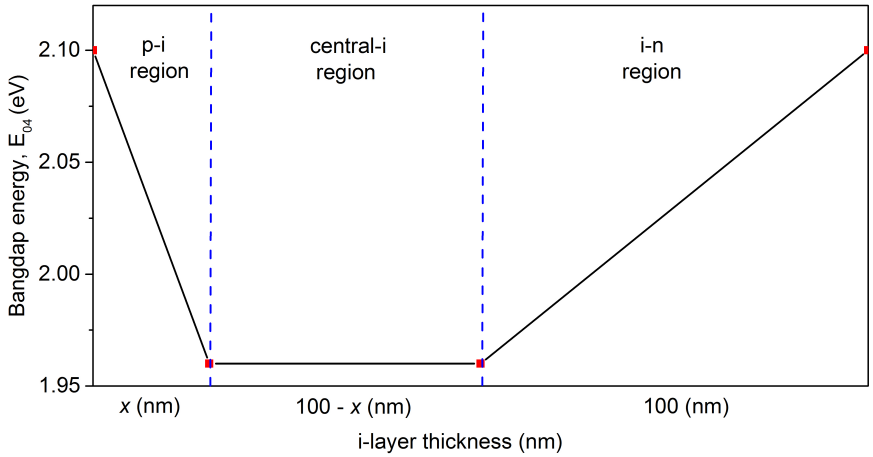

Figure 4.2: A schematic diagram of varying the p-i region grading width over a total i-layer thickness of 200 nm while the grading width at the i-n region is kept constant at a 100 nm.

4.3.2. Results and analysis

The electrical parameters of the graded bandgap energy solar cells upon varying the grading width in the p-i region are shown in Figure 4.3. It needs to be noted that out of the seven cells fabricated six cells have a U-type grading profile and one cell (cell with 100 nm p-i region grading width) has a V-type grading profile.

The V_{OC} of the cells do not show any increasing or a decreasing trend upon increasing the grading width. All the seven cells showed lower V_{OC} values than that of the reference cell. The cell with the 100 nm grading width (V-type) showed the highest V_{OC} with a value of 0.971 ±0.003 V. The cell with the 40 nm grading width showed the lowest V_{OC} with a value of 0.937 ±0.006 V.

The FF was found to decrease with increasing the grading width at the p-i region.The cells fabricated with a graded bandgap energy was found to have lower values of FF than that of the reference and that of 1.96 eV flat bandgap energy cell. As for the J_{SC}, the cell with smallest grading width showed the highest value among the graded bandgap energy cells. Though all seven cells had J_{SC} values higher than that of the reference cell, the 1.96 eV flat bandgap energy cell showed the highest of 13.82 ± 0.03 mA/cm^2.

The difference in the J_{SC} values can be observed in their EQE plots shown in Figure 4.4(c). There are two plots shown, so as to better understand the change in the EQE curves as the grading width increases. The plot in the left shows EQE curves for 10 nm and 30 nm grading widths in the p-i region. The cells with the 10 nm and 30 nm grading width showed higher values of EQE in the blue region than that of the reference cell and the 1.96 eV flat bandgap energy cell. Between 500 nm and 800 nm, the 1.96 eV flat bandgap energy cell shows a higher response than the other three cells shown in the plot. Among the 10 nm and 30 nm grading width in the p-i region, the one with 30 nm grading width has a larger response in the blue region, whereas the response of the cell with the 10 nm grading width was higher in the wavelength range of 500 nm - 800 nm.

Figure 4.4(b) shows the EQE curves for further increases in grading width. The three cells with 30 nm, 60 nm and 100 nm grading width in the p-i region had responses in the blue region that were higher than that of the reference cell and the 1.96 eV flat bandgap energy cell. Between 500 nm and 800 nm, the 1.96 eV flat bandgap energy cell had larger response than the rest of the cell showcased in the plot. Among the three cells fabricated with the graded bandgap energy, the response in the blue region was found to decrease as the grading width increases from 30 nm to 100 nm. The response between 500 nm and 800 nm increased as the grading width increased from 30 nm to 60 nm and the decreased as the grading width increases to 100 nm. Overall, it can be said that the response in the blue region first increases with increase in grading width and then decreases with further increase in the grading width.

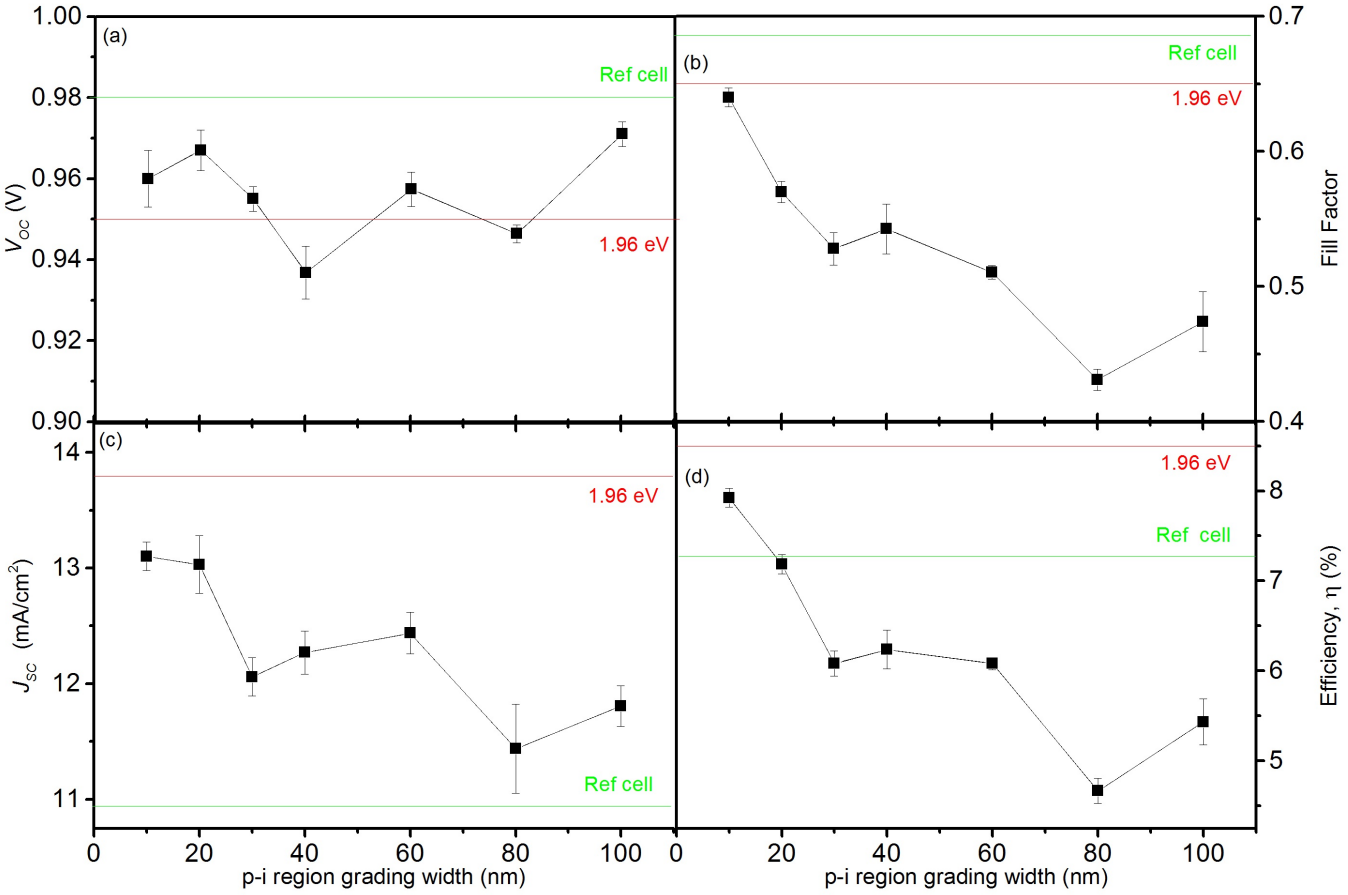

Figure 4.3: Electrical parameters of the graded bandgap energy a-SiO$_x$: solar cells as a function of p-i region grading width : (a) V_{OC}; (b) FF; (c) J_{SC}; (d) efficiency.

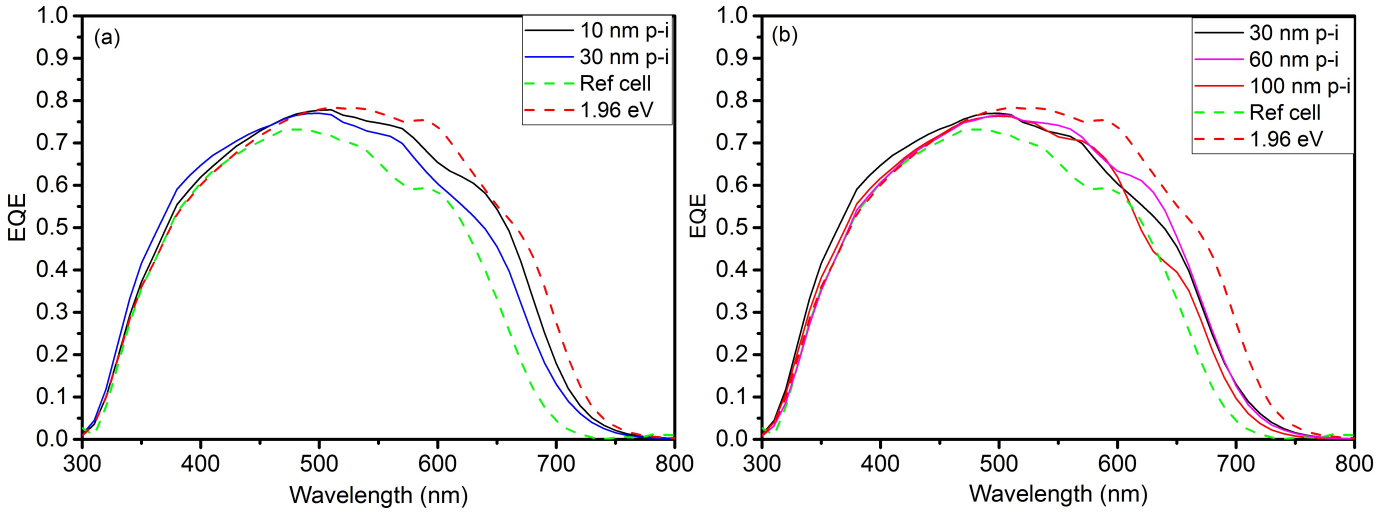

Figure 4.4: EQE plots (a) and (b) of the graded bandgap energy a-SiO$_x$:H solar cells with varying p-i region grading width.

Lastly, looking at the efficiency in Figure 4.3, the efficiency decreased with increasing grading widths. Among the seven graded bandgap energy cells, the highest efficiency was observed by the cell with the 10 nm grading width with a value of 7.9 ±0.1 % and is the only cell with an efficiency higher than the reference cell. The increase in efficiency can attributed to the significant increase in J_{SC}. Though other cells with the graded bandgap energy cells had higher J_{SC} than the reference cell, their efficiencies suffered due to their significant drop in FF. An iso-efficiency plot of the V_{OC}× FF product vs. J_{SC} for the solar cells fabricated as a function of p-i region grading width are shown in Figure 4.5. A downward trend is observable in the efficiency and V_{OC}× FF product as the grading width in the p-i region increases. The cell with the 10 nm grading width in the p-i region and 100 nm grading width in the i-n region showed the best performance among the other graded bandgap energy cells, hence the process for optimizing the i-n region grading width will be done while keeping the p-i region grading constant at 10 nm.

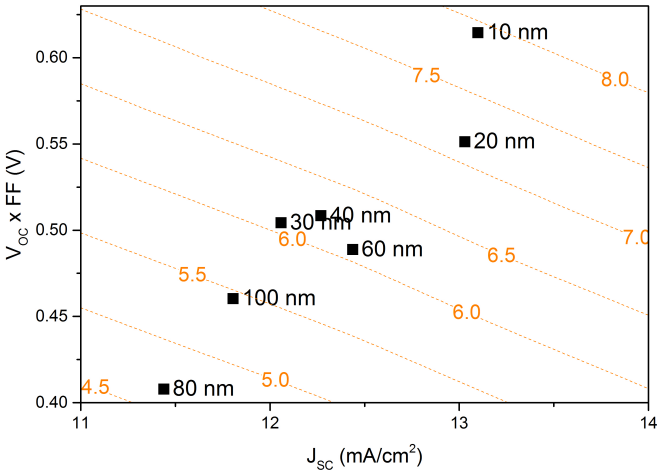

Figure 4.5: V_{OC}× FF product vs. J_{SC} for graded bandgap energy a-SiO$_x$:H solar cells as a function of p-i region grading width.

4.4. Varying i-n region grading width

4.4.1. Experimental details

The process with which the optimum grading width in the i-n region is obtained is similar to that of finding the optimum grading width in the p-i region. The bandgap gap energy values from where the grading starts and ends are the same; i.e from 2.1 eV to 1.96 eV. As established in the results and analysis of varying the p-i region grading width, a 10 nm grading width in p-i region showed better performance in comparison to other grading widths.

A schematic diagram depicting the grading width and central-i region as a function grading width x in nm while the grading width in the p-i region is kept constant at 10 nm is shown in Figure 4.6. The grading width in the i-n region was varied from 20 nm to 190 nm in no sequential order. In total 8 solar cells were fabricated with their results and effects of the grading pattern presented in the next section.

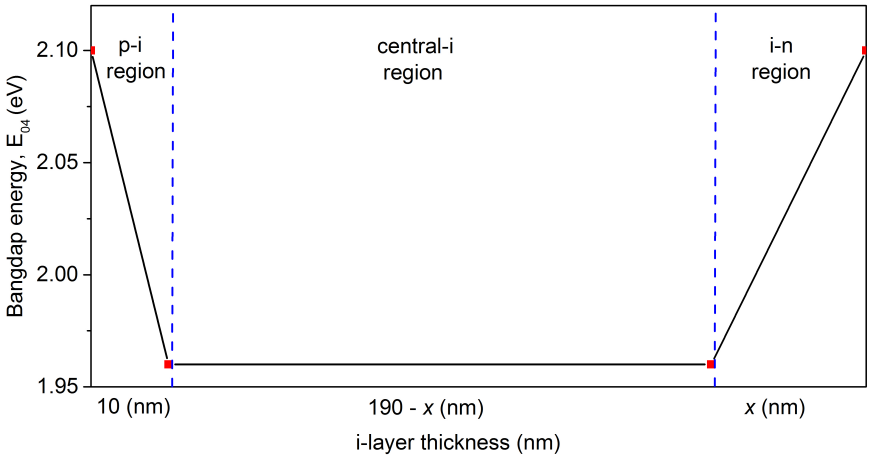

Figure 4.6: A schematic diagram of varying the i-n region grading width over a total i-layer thickness of 200 nm while the grading width at the p-i region is kept constant at a 10 nm.

4.4.2. Results and analysis

The electrical parameters of the graded bandgap energy solar cells upon varying the grading width in the i-n region are shown in Figure 4.7. A total of 8 solar cells were fabricated out which seven cells have a U-type grading profile and one cell (cell with 190 nm grading width in the i-n region) has a V-type grading profile. All cells have a 10 nm grading width in the p-i region where the bandgap energy was graded from 2.1 eV to 1.96 eV.

The V_{OC} of the graded bandgap energy cells do not show an increasing or decreasing trend upon increasing the grading width in the i-n region from 20 nm to 190 nm. Some cells fabricated with varying the grading width in the i-n region exhibited V_{OC} values lower than the 1.96 eV flat bandgap energy cell.

Discussing the FF performance in Figure 4.7(b), the FF values were below that of the reference cell. The FF showed a decreasing trend for an increase in grading width with the exception of the cell with the 80 nm grading width. The highest FF was exhibited by the cell with a 80 nm grading width in the i-n region and is also closer to the fill factor value of the reference cell.

Looking at the J_{SC} in Figure 4.7(c), all the values were above that of the reference cell. The highest J_{SC} was shown by the cell with the 20 nm grading width in the i-n region with a value of 13.4 $\pm$0.2 mA/cm^2. Also, it can be observed that the J_{SC} decreases with increasing grading width in the i-n region.

On comparing the J_{SC} values to the EQE performance in Figure 4.8, the response of the graded bandgap energy cells were higher than the reference cell over the entire wavelength range of 300 nm - 800 nm. Figure 4.8 shows the EQE plots so as to better observe the EQE performance of the cells upon varying the grading width. Figure 4.8(a) shows the EQE curves for cells with grading widths of 20 nm, 40 nm and 80 nm and Figure 4.8(b) shows the EQE curves for cells with grading widths of 80 nm, 100 nm and 120 nm. The response in the blue region increases as the grading width increases to 80 nm and then was found to decrease over further increase in grading widths. But as the grading width increases the response between the wavelengths of 500 nm and 800 nm was found to decrease. This can be explained by the fact that as the grading width increases the length of the absorber layer with a lower bandgap energy decreases. This change in response can also be observed when comparing the EQE curves with that of the 1.96 eV flat bandgap energy cell, which has a higher response than all the other cells within a wavelength range of 500 nm to 800 nm.

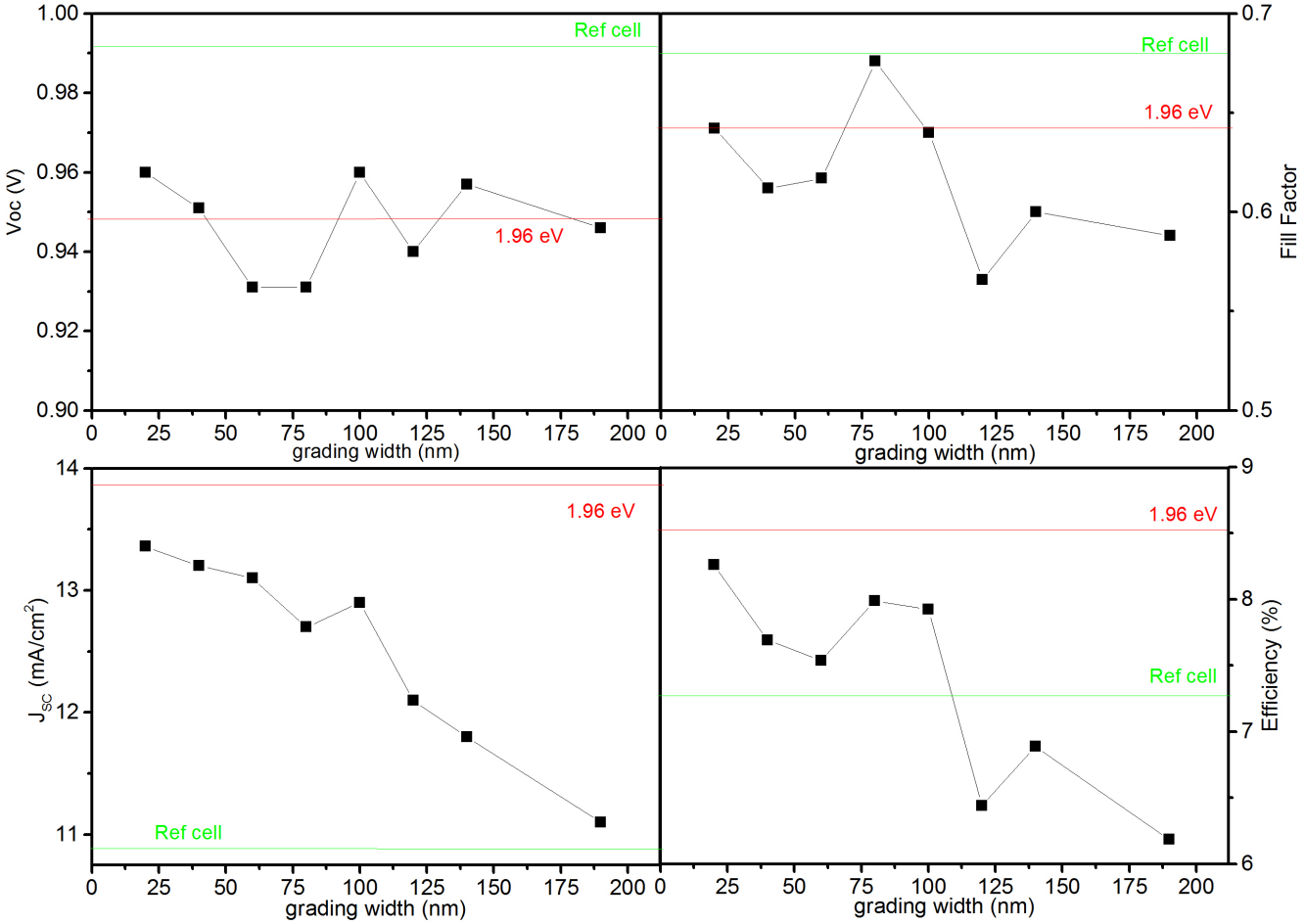

Figure 4.7: Electrical parameters of the graded bandgap energy a-SiO_x: solar cells as a function of i-n region grading width : (a) V_{OC}; (b) FF; (c) J_{SC}; (d) efficiency.

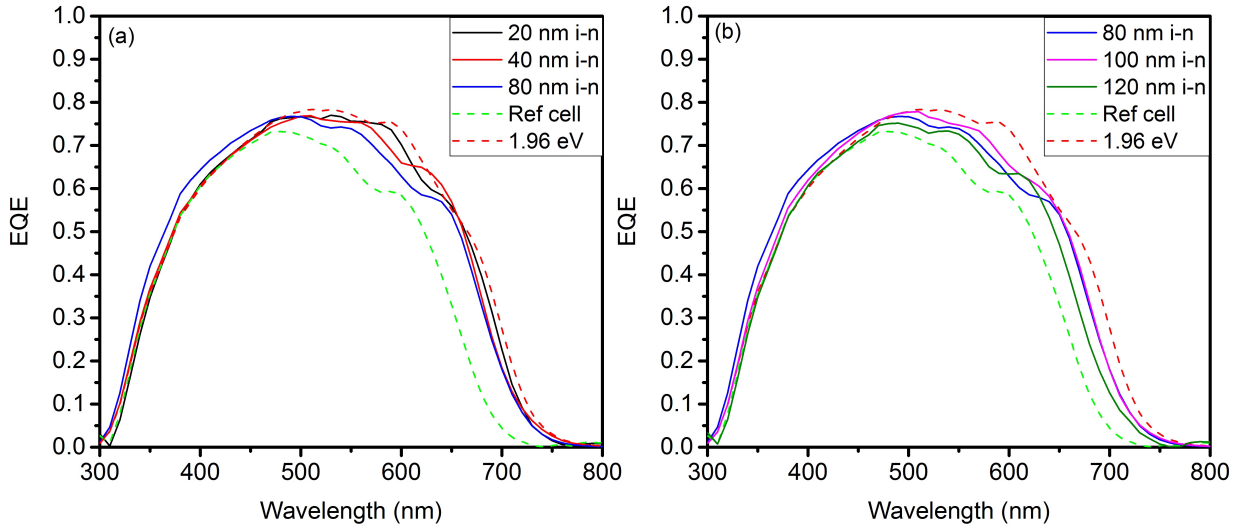

Figure 4.8: EQE plots (a) and (b) of the graded bandgap energy a-SiO_x:H solar cells with varying i-n region grading width.

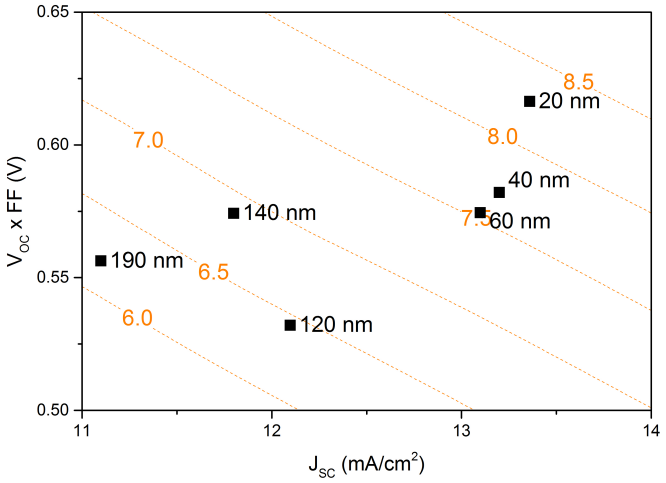

Figure 4.9: V_{OC}× FF product vs. J_{SC} for graded bandgap energy a-SiO$_x$:H solar cells as a function of i-n region grading width.

Lastly the efficiency as seen in Figure 4.7(d), follows a decreasing trend as the grading width increases. Only cells graded to widths up to 100 nm showed efficiencies above the reference cell. Off all the graded bandgap energy cells, the cell with the 20 nm grading width in the i-n region showed the highest efficiency with a value of 8.3 ±0.2 %. An iso-efficiency plot of the V_{OC}× FF product vs j_{SC} as a function of i-n region grading width is shown in Figure 4.9. A downward trend in efficiency and V_{OC}× FF product is observable with increasing i-n region grading width, similar to that observed with increasing the p-i region grading width. The graded bandgap energy solar cell with 20-nm thick grading region has the highest V_{OC}× FF product of 0.62 ± 0.01 V, combined with the J_{SC} obtained, pushes the efficiency of the cell above 8%. From this, it can be said that the optimum grading width in the i-n region is 20 nm. This means, that the optimum grading widths in the p-i region is 10 nm and the i0n region is 20 nm.

4.5. Conclusion

In this chapter, several cells with different grading widths at both the p-i region and the i-n region were fabricated and were analyzed in comparison to the reference cell and a 1.96 eV flat bandgap energy cell. Increasing the grading width at both the p-i region and the i-n region did not increase the V_{OC} or the FF above that of the reference cell. But, grading the bandgap energy did show a significant increase the J_{SC} of the cells. The highest J_{SC} was obtained by the cell with a 10 nm p-i grading and a 20 nm i-n grading with a value of 13.36 ±0.15 mA/cm^2 and a higher efficiency than that of the reference cell. This indicates that when fabricating graded bandgap energy a-SiO$_x$:H cells, keep the grading width as small as possible at both the p-i region and the i-n region. It was also observed that by having a small grading width at the p-i and i-n regions, the cell exhibited higher response in the blue region.

Also, the several graded bandgap cells fabricated did not show a J_{SC} value higher than that of the 1.96 flat bandgap energy cell. This also hints at, that no matter to how much length the bandgap energy is graded to, the J_{SC} of the graded cell will not exceed the J_{SC} produced by the cell which has an absorber layer with an uniform bandgap energy to which the other cells are graded down to.

The results obtained in this work show a significant increase in J_{SC} to the graded bandgap energy cells presented in the work of Rodriguez [18]. However, It needs to be mentioned that this work confirms the conclusion documented by Rodriguez, which is to keep grading widths as small as possible in both the p-i and i-n region for a-SiO$_x$:H solar cells. Rodriguez showed an increase in J_{SC} by 1 mA/cm^2 through the implementation of step-wise grading. In this work, an increase of J_{SC} by 2 mA/cm^2 has been observed by adapting a linearly graded bandgap energy profile.

5

Effect of grading the bandgap energy on the performance of a-SiO_x:H solar cells

5.1. Introduction

In the previous chapter, the graded bandgap energy solar cells were fabricated with varying grading widths to obtain a optimum grading width at the p-i and i-n region. It was found that the bandgap energy grading can increase the J_{SC} and efficiency of the cell by incorporating a narrow grading width at both the p-i and the i-n region of the absorber/intrinsic a-SiO_x:H layer. Despite the increase in J_{SC}, none of the graded bandgap cells developed and presented in the previous chapter showed a higher J_{SC} and efficiency than the 1.96 eV flat bandgap energy cell.

The main objective of this chapter is to perform a series of experiments on the graded bandgap structure, so as to obtain a higher J_{SC}, while maintaining a high $V_{OC}\times$ FF product. In this chapter the results are presented for the cells fabricated in three sets of experiments. The first set of experiments looks at the effect of varying the bandgap grading on the performance of the a-SiO_x:H solar cells. In the second set of experiment, the bandgap energy is graded down to 1.92 eV by varying not only the SiH_4 to CO_2 gas flow ratio, but also changing the H_2 gas flow during deposition. The third and final set of experiment was conducted to observe the performance of the graded bandgap energy a-SiO_x:H cells on varying the absorber layer thickness.

5.2. Varying the bandgap energy value for the graded bandgap energy a-SiO_x:H solar cells

5.2.1. Experiment details

The first set of experiments in this chapter will focus on varying the range at which the bandgap energies are graded and observe the results of this change in bandgap energy range. In the previous chapter, the bandgap energy is graded from a $E_{04,max}$ of 2.1 eV to a $E_{04,min}$ of 1.96 eV, and the performance of the cells were analyzed on changing the grading width. In this experiment, the $E_{04,max}$ of the cells developed will be changed while keeping $E_{04,min}$ at 1.96 eV and the grading widths at the p-i region at 10 nm and at the i-n region at 20 nm, respectively.

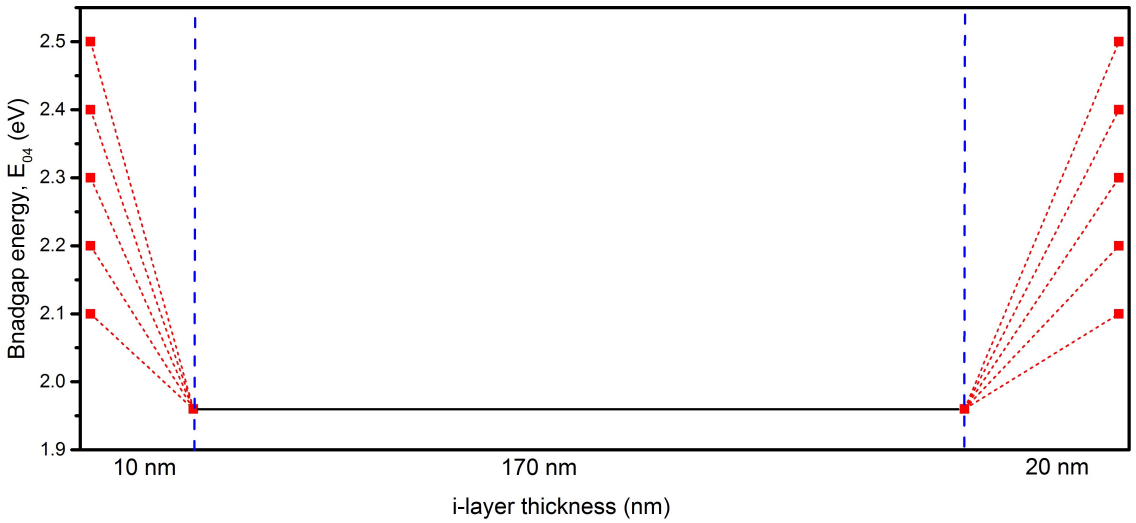

Figure 5.1: A schematic diagram of varying the bandgap energy for the graded bandgap energy a-SiO$_x$:H solar cells fabricated. The $E_{04,min}$ is kept at 1.96 eV and the grading widths at the p-i and i-n region are kept narrow at 10 nm and 20 nm respectively.

Figure 5.1 shows how the various bandgap energy ranges of which the graded bandgap energy a-SiO$_x$:H solar cells were fabricated. In total five graded bandgap energy solar cells were fabricated with the $E_{04,max}$ varying from 2.1 eV to 2.5 eV. The $E_{04,min}$ value was 1.96 eV and the objective is to compare the performance of all these cells to that of the reference a-SiO$_x$:H cell and the 1.96 eV flat bandgap energy cell explained in the chapter 4.

5.2.2. Results and analysis

The external parameters of the a-SiO$_x$:H cells with graded bandgap energy and varying bandgap energy max, $E_{04,max}$ are shown in Figure 5.2. The EQE curves of these cells are shown in Figure 5.3.

Figure 5.2a shows the V_{OC} values obtained for the cells developed. A concrete trend is not ascertainable on the values of the V_{OC} as the $E_{04,max}$ increases. The graded bandgap energy cell with an $E_{04,max}$ of 2.5 eV showed the lowest V_{OC}, despite the presence of a 2.5 eV i-a-SiO$_x$:H layer at the p/i interface. The graded bandgap energy cells had V_{OC} values lower than that of the reference cell and cells with $E_{04,max}$ values from 2.1 eV to 2.4 eV had a higher V_{OC} than the 1.96 eV flat bandgap energy cell.

The second observation is the decline in FF values as the $E_{04,max}$ of the graded bandgap energy cells are increased, as seen in Figure 5.2b. The cell with an $E_{04,max}$ of 2.3 eV showed a lowest FF of 0.28 ± 0.01. Both the reference cell and the 1.96 eV flat bandgap energy cell had a higher FF than the graded bandgap energy cells. Just like the FF performance upon increasing the grading width, also increasing the height or the $E_{04,max}$ to which the bandgap energy of cells are graded also decreases the fill factor.

The third observation is the decrease in J_{SC} values of the graded bandgap energy cells as the $E_{04,max}$ increases. All the solar cells have a J_{SC} higher than the reference cell but lower than the 1.96 eV flat bandgap energy cell. By comparing the J_{SC} to the obtained EQE curves in Figure 5.3, all the fabricated graded bandgap energy cells had a higher response at all wavelengths than that of the reference cell. Also, as the $E_{04,max}$ increases, the response of the graded bandgap energy cell decreases at wavelengths from 300 nm - 500 nm. After 550 nm the response of the graded bandgap energy with an $E_{04,max}$ of 2.1 eV drops. The response of the other cells after 550 nm decreases with increasing the $E_{04,max}$ of the graded bandgap energy cell with the cell with an $E_{04,max}$ of 2.1 eV being the exception. From 650 nm - 800 nm the response the 1.96 eV rises above the rest of the cells presented in Figure 5.3b.

Finally, the efficiency decreases with increasing the $E_{04,max}$ of the graded bandgap energy cells. This is likely to have been caused by the poor fill factor obtained by these cells. Only cells with an $E_{04,max}$ of 2.1 eV and 2.2 eV had efficiencies higher than the reference cell, while the 1.96 eV had the highest among all the cells developed. The graded bandgap energy cell with an $E_{04,max}$ of 2.1 eV showed an efficiency of 8.3 ± 0.2%, which was the closest to the efficiency of the 1.96 eV flat bandgap energy cell. It also needs to be mentioned that some of the graded bandgap energy cell developed with $E_{04,max}$ values greater than 2.2 eV exhibited the worst efficiencies among all the cells developed in this work.

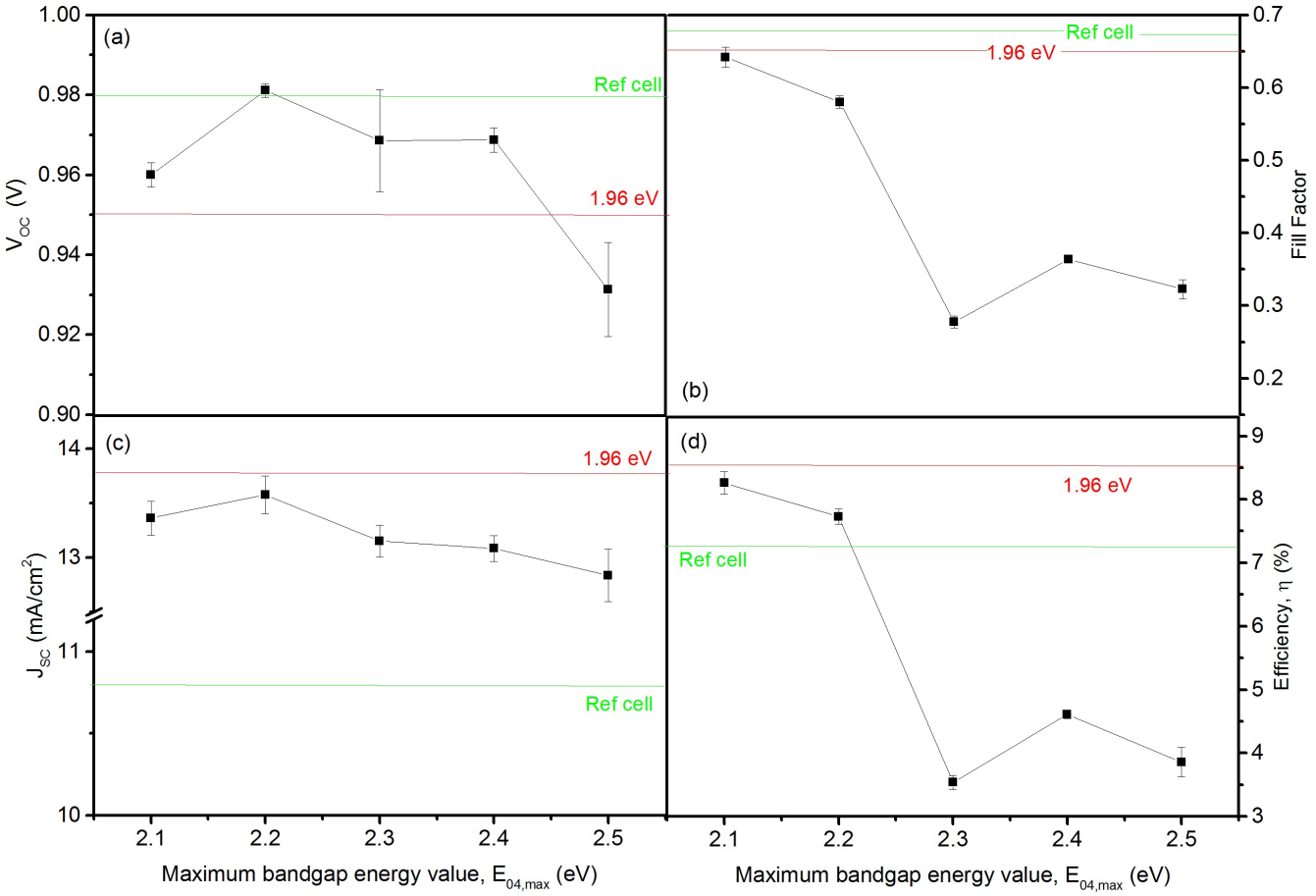

Figure 5.2: Electrical parameters of the graded bandgap energy a-SiO$_x$: solar cells as a function of $E_{04,max}$ of graded bandgap energy a-SiO$_x$:H solar cells : (a) V_{OC}; (b) FF; (c) J_{SC}; (d) efficiency.

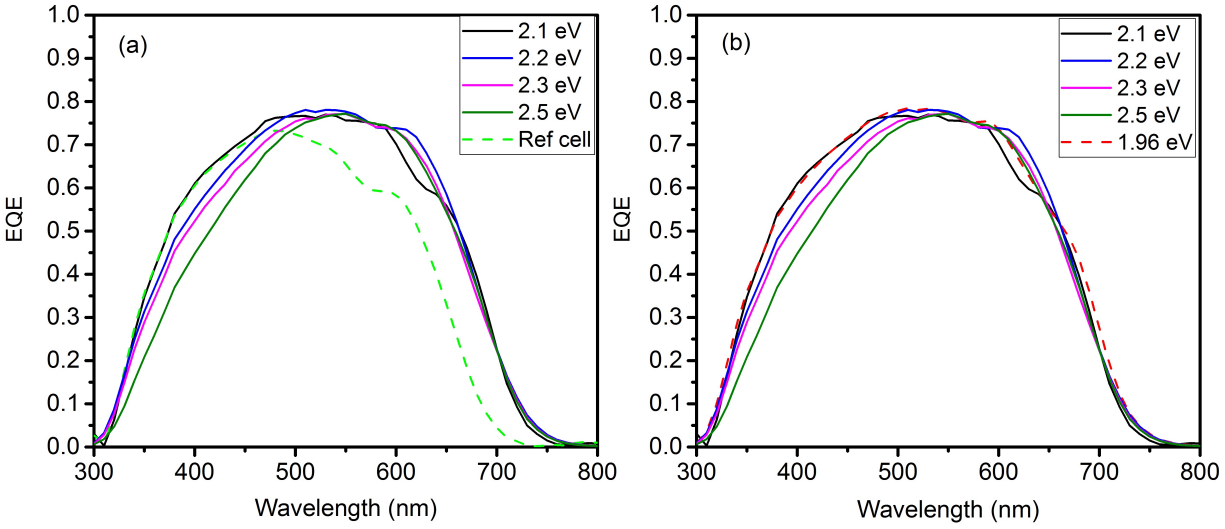

Figure 5.3: (a) EQE of graded bandgap energy cells with different $E_{04,max}$ and the reference a-SiO$_x$:H cell. (b) EQE of graded bandgap energy cells with different $E_{04,max}$ and the 1.96 eV flat bandgap energy cell.

5.3. a-SiO$_x$:H solar cell with bandgap energy graded to 1.92 eV

5.3.1. Experimental details

The aim of this set of experiment is to grade the bandgap energy to even lower values (i.e. lower than 1.96 eV) so as to have higher J_{SC} values of the fabricated graded bandgap energy cell than those cells mentioned in section 5.2 and in Chapter 4. For this experiment, test depositions of varying the H_2 gas flows are conducted so as to obtain a trend on the change in E_{04} and the deposition rate. The E_{04} and the deposition rate data obtained from varying the H_2 gas flow are shown in Figure 5.4.

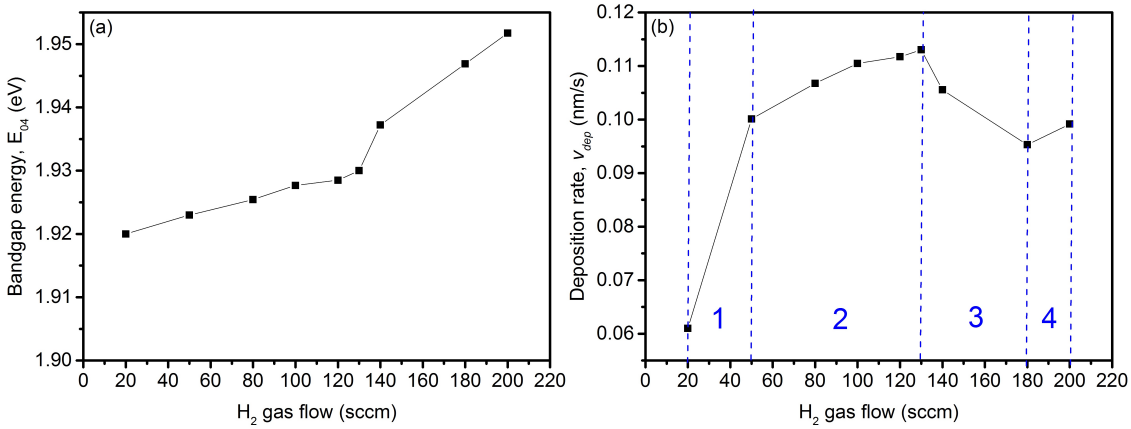

Figure 5.4: (a) diagram showing the change in bandgap energy E_{04} for change in H_2 gas flow. (b) diagram showing the change in deposition rate for change in H_2 gas flow.

It can be observed from Figure 5.4 that the E_{04} bandgap energy value can be decreased to 1.920 ± 0.003 eV by decreasing the H_2 gas flow from 200 sccm to 20 sccm. Decreasing the H_2 flow rate further resulted in the plasma discontinuing during the deposition process, due to the very small gas flows. The deposition rate values fluctuated as the H_2 gas flow decreased from 200 sccm to 20 sccm. For this experiment one graded bandgap energy a-SiO$_x$:H cell was fabricated, where the bandgap energy was graded from a value of 2.1 eV to 1.92 eV. The bandgap energy was graded from 2.1 eV to 1.95 eV by changing the gas flow ratio r defined in Equation 3.1 and the bandgap energy from 1.95 eV to 2.1 eV was graded by changing the H_2 gas flow. The H_2 gas flow is changed in four stages from 200 sccm to 20 sccm as shown by the blue dashed lines segmenting Figure 5.4b. The grading width utilized is of that optimized in Chapter 4, which is a 10 nm p-i region and 20 nm i-n region grading width.

5.3.2. Results and analysis

The external parameters of the solar cell graded to a lower bandgap energy value of 1.92 eV are shown in Table 5.1 and the EQE curve in Figure 5.5. The results of the 2.1 eV - 1.92 eV graded bandgap energy a-SiO$_x$:H is analyzed in comparison to three cells: (1) the reference a-SiO$_x$:H solar cell; (2) the 1.96 eV flat bandgap energy cell; and (3) the 2.1 eV - 1.96 eV graded bandgap energy cell with grading widths of 10 nm and 20 nm at both the p-i and i-n region respectively.

Table 5.1: External parameters of the 2.1 eV - 1.92 eV and 2.1 eV - 1.96 eV graded bandgap energy a-SiO$_x$:H solar cell with 10 nm i-n region grading width and 20 nm p-i region grading width, the reference a-SiO$_x$:H solar and the 1.92 eV flat bandgap energy a-SiO$_x$:H solar cell.

	V_{OC} (V)	Fill Factor	J_{SC} (mA/cm^2)	Efficiency (%)
2.1 eV - 1.92 eV graded bandgap cell	0.936 ± 0.004	0.59 ± 0.01	13.95 ± 0.03	7.66 ± 0.14
2.1 eV - 1.96 eV graded bandgap cell	0.963 ± 0.001	0.64 ± 0.01	13.36 ± 0.01	8.26 ± 0.17
Reference a-SiO$_x$:H cell	0.983 ± 0.003	0.68 ± 0.02	10.8 ± 0.1	7.19 ± 0.18
1.96 eV flat bandgap cell	0.948 ± 0.002	0.65 ± 0.01	13.81 ± 0.03	8.52 ± 0.15

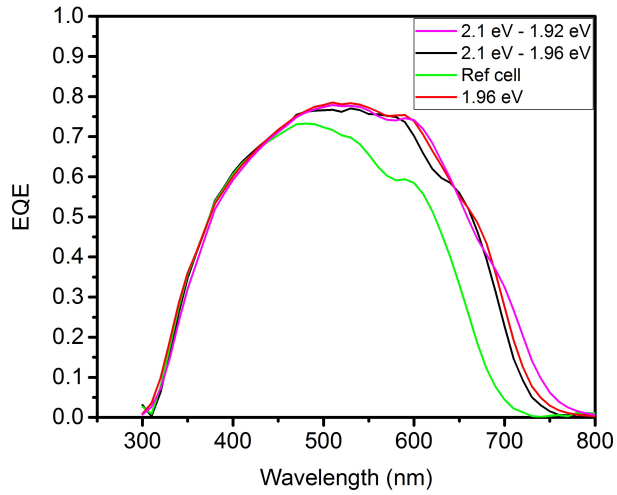

Figure 5.5: EQE of the 2.1 eV - 1.92 eV graded bandgap energy a-SiO$_x$:H solar cell

First, the V_{OC} is the lowest for the 2.1 eV - 1.92 eV graded bandgap energy cell in comparison to the other cells shown in Table 5.1 and so is the fill factor. The 2.1 eV - 1.92 eV graded bandgap energy cell showed the highest J$_{SC}$ of the four cells in Table 5.1 of 13.95 ±0.03 mA/cm^2. But due to lower V_{OC} and fill factor values, the efficiency attained by the 2.1 eV - 1.92 eV graded bandgap energy cell was only at a value of 7.7 ±0.1 %.

While comparing the EQE curves in Figure 5.5, the 2.1 eV - 1.92 eV graded bandgap energy cell has a higher response than the the reference cell, the 1.92 eV flat bandgap energy cell and the 2.1 eV - 1.96 eV graded bandgap energy cell at all wavelengths ranging from 700 nm to 800 nm. While at the rest of the wavelength range (i.e. from 300 nm to 700 nm), the cell showed lower response than that of the 1.96 eV flat bandgap energy cell. Clearly, the bigger response between 700 nm and 800nm contributes to a higher J_{SC} value than that of the 1.96 eV flat bandgap energy cell.

Finally, it can be concluded that by grading the bandgap energy down to 1.92 eV a high value of J_{SC} was attained, but the low V_{OC} × FF product drags down the performance of the cell in comparison to the 2.1 eV - 1.96 eV graded bandgap energy cell and the 1.92 eV flat bandgap energy cell.

5.4. Varying the intrinsic a-SiO$_x$:H layer of the graded bandgap a-SiO$_x$:H

5.4.1. Experimental details

The final set of experiments looks at the performance of graded bandgap energy a-SiO$_x$:H solar cells when the intrinsic layer thickness is varied. As mentioned in Chapter 1, Kim et al. [7] found that as the i-a-SiO$_x$:H layer increases in thickness, the V_{OC}× fill factor product decreases while the J_{SC} increases. The increase in J_{SC} only increases until a certain thickness of the i-a-SiO$_x$:H layer and further increase in thickness results in a sudden decrease in the J_{SC} value.

In total 8 graded bandgap energy a-SiO$_x$:H solar cells with varying i-a-SiO$_x$:H layer thicknesses. i-a-SiO$_x$:H layer thicknesses were varied from 125 nm for every 25 nm to 300 nm. The grading widths exhibited by the cells are 10 nm in the p-i region and 20 nm in the i-n region. The results of these cells fabricated will be compared to the reference a-SiO$_x$:H cell and the 1.96 eV flat bandgap energy cell. Also if any trend is observed in the V_{OC}× fill factor product vs. J_{SC} of the cells fabricated, it will also be compared to the trend observed in the work of Kim et al. [7].

Before going into the analysis of the results, it needs to mentioned that the graded bandgap energy cell with an i-layer thickness of 200 nm with p-i and i-n region grading widths of 10 nm and 20 nm are not the same as the cell with the same gas flow compositions and similar i-layer thickness, p-i and i-n region grading widths fabricated in Chapter 4. This is because the newly obtained deposition rates for performing the fabrication of the cells belonging to this set of experiments do not match and can be said to have a different material composition than the graded bandgap energy cell developed in Chapter 4.

5.4.2. Results and analysis

The external parameters of the graded bandgap energy cells with different i-layer thickness are shown in Figure 5.6 and EQE curves in Figure 5.7.

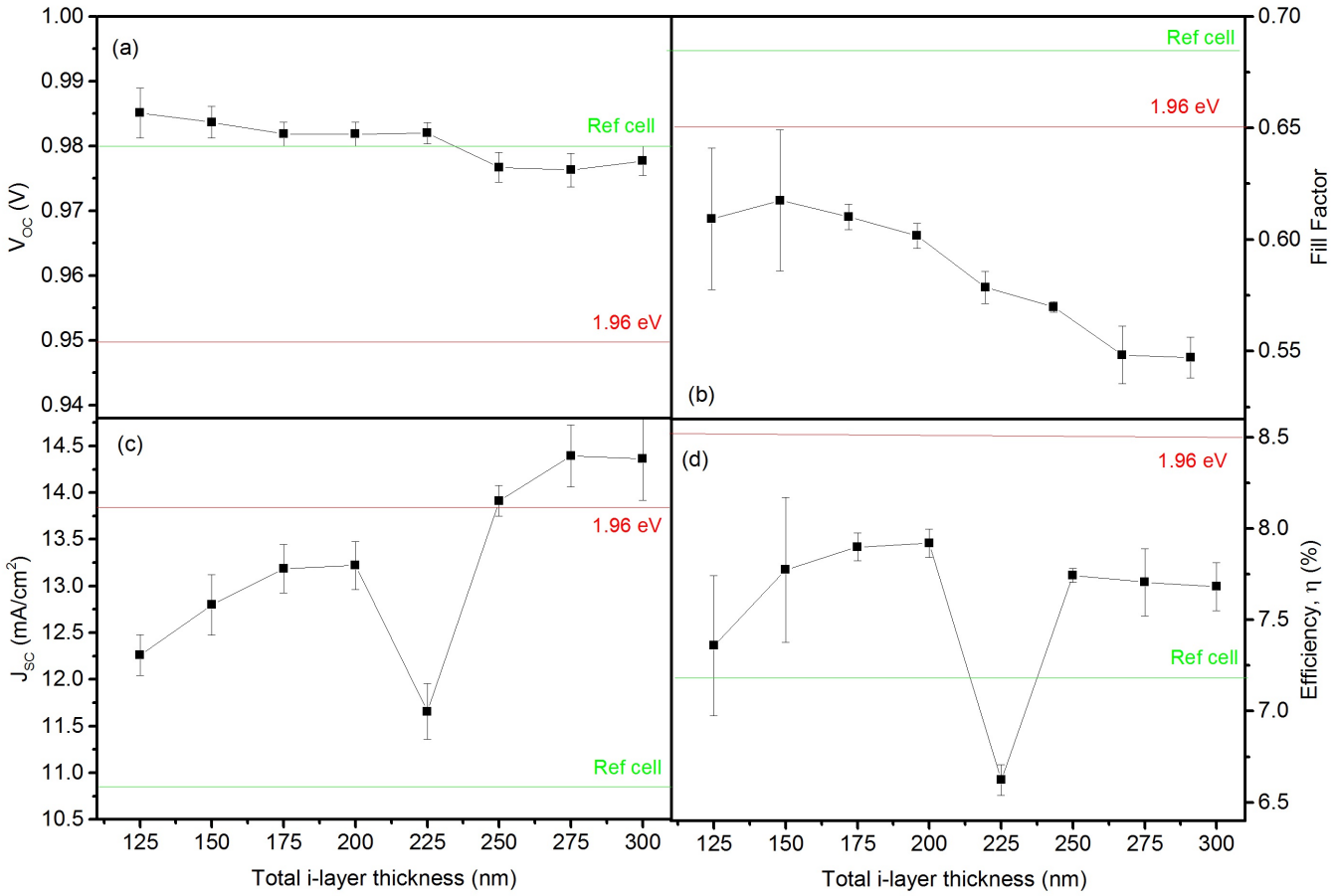

Figure 5.6: Electrical parameters of the graded bandgap energy a-SiO$_x$: solar cells as a function of i-layer thickness of the graded bandgap energy a-SiO$_x$:H solar cells : (a) V_{OC}; (b) FF; (c) J_{SC}; (d) efficiency.

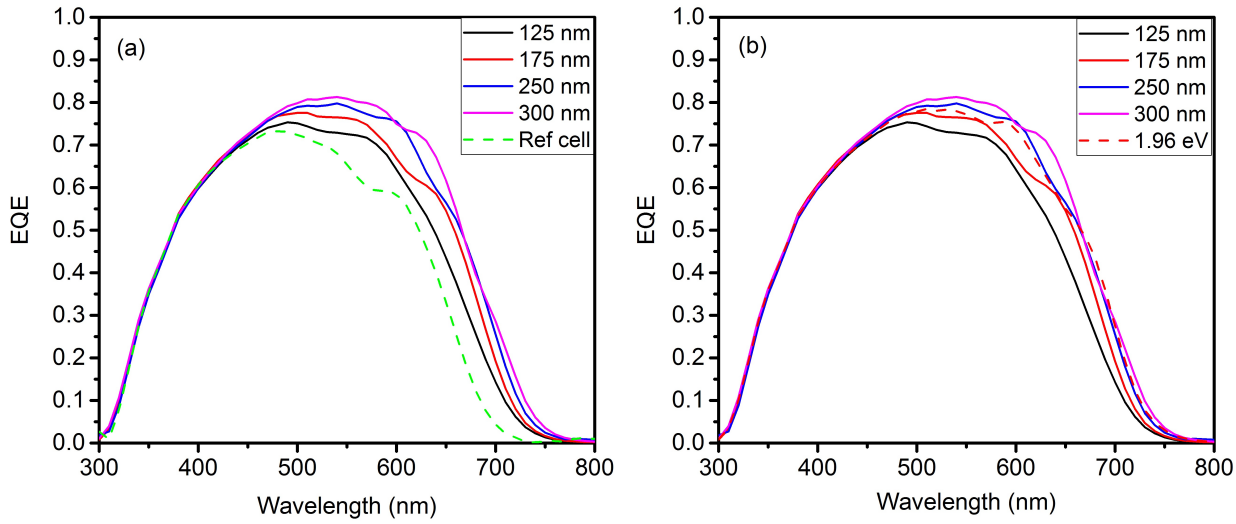

Figure 5.7: (a) EQE of graded bandgap energy cells with different $E_{04,max}$ and the reference a-SiO$_x$:H cell.(b) EQE of graded bandgap energy cells with different $E_{04,max}$ and the 1.96 eV flat bandgap energy cell.

This can be observed in the differences in the electrical properties for the 200 nm thick i-layer for the graded bandgap energy cell developed in this set of experiments to that developed in Chapter 4.

First, both the V_{OC} and the fill factor decreased as the i-layer thickness increases from 125 nm to 300 nm. All of the graded bandgap energy cells had a V_{OC} higher than the 1.96 eV flat bandgap energy cell. Graded bandgap energy cells with i-layer thicknesses from 125 nm to 225 nm showed values of V_{OC} higher than that of the reference cell itself. As the i-layer thickness increases, the V_{OC} did not drop as steep as it dropped for change in $E_{04,max}$ of the graded bandgap energy cell.

Secondly, the fill factor decreases as the i-layer thickness increased. All the graded bandgap energy cells fabricated have their fill factor lower than both the reference cell and the 1.96 eV flat bandgap energy cell.

Thirdly, the J_{SC} increases with increasing the i-layer thickness. A J_{SC} as high as 14.4 ± 0.3 mA/cm^2 is observed on increasing the i-layer thickness. The J_{SC} can be correlated to the EQE curves shown in Figure 5.7. It is observable that the response of the cells increase with increasing i-layer thickness at wavelengths from 450 nm - 800 nm. All the cells show higher response than the reference cell and the graded bandgap energy cells with thicknesses of 250 nm and 300 nm showed higher response than the 1.96 eV flat bandgap energy cell across the wavelength region of 300 nm - 800 nm. From the analysis it is evident that having a thin intrinsic layer results in a smaller J_{SC} due to lesser absorption at longer wavelengths. Whereas, increasing the i-layer thickness allows for higher absorption of photons resulting in higher J_{SC} values. Among all the graded bandgap energy cells, the cell with an i-layer thickness of 225 nm showed the lowest value of J_{SC} , not obeying trend of an increasing J_{SC}. The cells with 275 nm and 300 nm thick i-layer showed the highest J_{SC} values of all the cells developed in this work.

Finally, the efficiency of the graded bandgap energy cell increased as the i-layer thickness increased from 125 nm to 200 nm and then decreased with an increase in thickness. All of the graded bandgap energy cells exhibited efficiencies higher than the reference cell with the exception of the 125 nm thick i-layer cell.

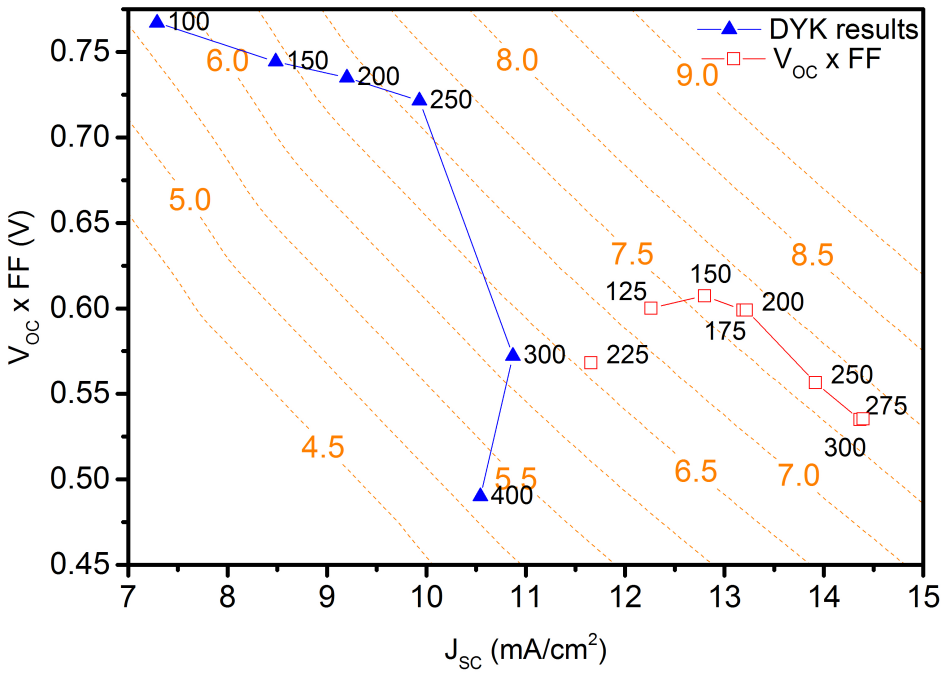

Figure 5.8: V_{OC}× fill factor product vs. J_{SC} of the graded bandgap energy a-SiO$_x$:H solar cells and a-SiO$_x$:H solar cells presented in the work of kim et al. [7] with change in i-layer thickness.

Figure 5.8 shows the V_{OC}× FF product vs. J_{SC} for the graded bandgap energy a-SiO$_x$:H solar cells with varying intrinsic layer thickness plotted on iso-efficiency lines. It is observable that as the thickness of the intrinsic layer increases the V_{OC}× FF product decreases and the J_{SC} increases. This is the same trend observed by Kim et al. in his work [7] with a-SiO$_x$:H solar cells without a graded bandgap energy intrinsic layer. Another observation from Figure 5.8 is in the efficiencies of the cell beyond i-layer thickness of 150 nm. The ef-

ficinecies decreased when the i-layer thickness was increased beyond 150 nm. But, the cells remained within an efficiency range of 7.5% - 8%. This is different from the trend observed by Kim et al [7]. in their work, as the thickness of the i-layer increased above 250 nm their efficiencies dropped from 7.2% - 5.2%, which is a dramatic drop in the efficiency in comparison to the decrease seen in graded bandgap energy cells.

As mentioned before, the cell with an i-layer thickness of 225 nm showed the lowest value of J_{SC} , not obeying trend of an increasing J_{SC}. To look into more detail as to why the graded bandgap energy cell with a 225 nm i-layer exhibited such a low value in comparison to the other cells, their EQE curves need to be observed. The EQE curves of the 225 nm intrinsic layer cell in comparison to three other cell in this set of the experiment are shown in Figure 5.9. The responses of the 150 nm, 175 nm and the 250 nm i-layer thick graded bandgap energy cells were higher than that of the 225 nm thick i-layer cell between 300 nm - 500 nm of the visible spectrum.Upon observing the deposition logs from the time of the cells depositions, the reason is a thicker p-layer which was caused due to an error during the fabrication process. During the deposition of the p-layer, the plasma was deactivated 14 seconds after the pre-programmed deposition time. This prolonged exposure to the plasma resulted in a p-layer thickness of 11 nm rather than 7 nm. Due to the thicker p-layer, there is more parasitic absorption as as majority of photons are absorbed in the p-layer and only allowing a minor amount of the photons to pass into the intrinsic layer.

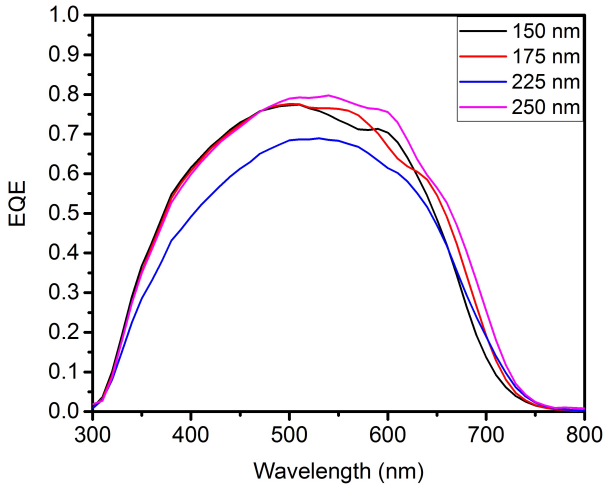

Figure 5.9: EQE curves of graded bandgap energy a-SiO$_x$:H solar cells with following i-layer thicknesses - 150 nm, 175 nm, 225 nm and 250 nm.

5.5. Conclusion

Three separate experiments were conducted to get a better outlook on the performances of graded bandgap energy with variation on the bandgap energy values of the grading and absorber thickness. On increasing the $E_{04,max}$ of the bandgap energy grading of the a-SiO$_x$:H solar cells, the fill factor dropped drastically and so did the J_{SC}. The drastic drop in fill factor resulted in cells exhibiting poor efficiencies.

For the second experiment, the bandgap energy was graded down to a value of 1.92 eV. The bandgap energy was graded by changing the SiH_4 and CO_2 gas flow followed by changing the H_2 dilution of the a-SiO$_x$:H material. The cell developed had lower V_{OC} and fill factor than the reference cell and the 1.96 eV flat bandgap energy cell. There was an increase in J_{SC} when compared to the standard bandgap energy grading (from 2.1 eV to 1.96 eV) done in this work. By taking into account the observations on varying the grading width from chapter 4, the changing in bandgap energy values, we can conclude that as the bandgap variation increases over the absorber layer the FF decreases.

Finally, the third experiment involved studying the performance of graded bandgap energy a-SiO$_x$:H solar on increasing the absorber thickness. On increasing the absorber thickness, the $V_{OC}\times$ fill factor product decreases and the J_{SC} decreases. As the absorber thickness increases the response of the cells in the far wavelength region of the visible spectrum also increases. The graded bandgap energy solar cells with i-layer thicknesses above 250 nm, show J_{SC} higher than 14 mA/cm^2, which are the highest J_{SC} values reported in this work.

6

a-SiO$_x$:H solar cells with graded bandgap energy using GenPro4

6.1. Introduction

Chapter 4 concentrated on the fabrication of graded bandgap energy a-SiO$_x$:H solar cells for the purpose of optimizing the grading widths. This is was later followed by conducting experiments to analyzing the performance of the graded bandgap energy solar cells upon changing the absorber layer thickness and the bandgap energy grading, as explained in Chapter 5. This chapter is dedicated to optical simulations of graded bandgap a-SiO$_x$:H solar cells by using the GenPro4 simulation software [84, 85].

The GenPro4 simulation software utilizes an optical model which uses wave and ray optics and calculates the reflection, absorbance and transmittance as a function of wavelength [85]. GenPro4 has been developed in the PVMD group of TU Delft. It takes in the optical constants n and k of the optical material as a function of wavelength as the input parameters for a certain solar cell design and gives the absorptance and the current generated for each layer as the output. The main goal of this chapter is to establish a method for simulating graded bandgap energy i-a-SiO$_x$:H for its use in solar cell design for the future.

6.2. Optical constants n and k of i-a-SiO$_x$:H layers for different bandgap energies

In this work, the method established to simulate the graded bandgap energy solar cells are to utilize i-a-SiO$_x$:H layers of several bandgap energies in a step wise fashion similar to that seen in Figure 3.6. This means that a graded bandgap energy i-a-SiO$_x$:H layer with a certain grading width can be divided into a number of i-a-SiO$_x$:H layers of decreasing or increasing bandgap energy values. This can result in simulating a 10 nm linearly graded i-a-SiO$_x$ layer by implementing either 10 or 20 layers of varying bandgap energies. This would require the optical constants n and k data from a bandgap energy of 1.95 eV to 2.48 eV for every 0.01 eV to substitute a linearly graded bandgap energy layer with 10, 20 or even a 100 layers of different bandgap energies.

The GenPro4 simulation software takes in the optical constants which are the refractive index and the extinction coefficient, represented as n and k respectively as the input. Determining the n and k as a function of wavelength for i-a-SiO$_x$:H layers from 1.95 eV to 2.48 eV for every 0.01 eV via the Lambda 950 spectrophotometer is possible but very time consuming. To obtain this, the n and k of a limited number of intrinsic layers for different bandgap energies are measured and the n and k for the intrinsic layers for intermediate bandgap energies are interpolated between the measured values.

The n and k as a function of wavelength four i-a-SiO$_x$:H layers for different bandgap energies are shown in Figure 6.1. It can be seen that as the bandgap energy of intrinsic layer increases the n and k decreases. Also the wavelength at which the extinction coefficient k decreases to 0 decreased with increasing bandgap energy. The n and k data of these four intrinsic layers and a few more with different bandgap energies will be used to obtain a profile of n and k for every 0.01 eV from 1.95 eV to 2.48 eV.

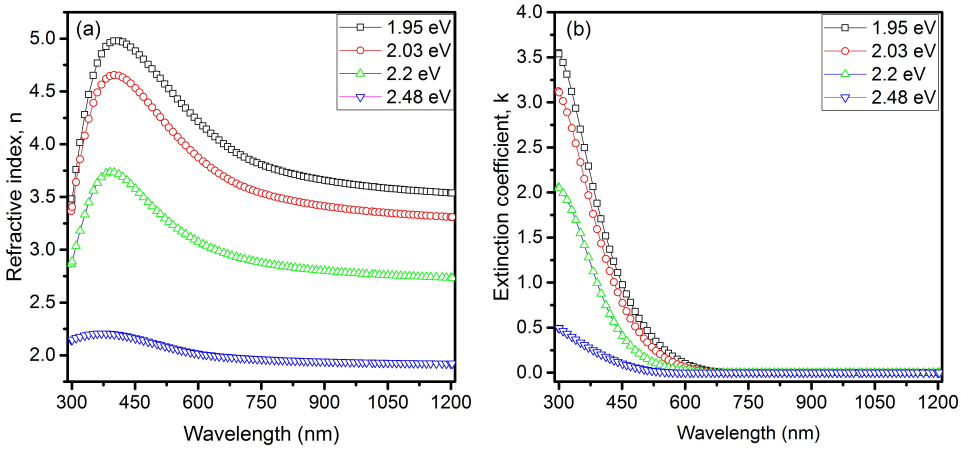

Figure 6.1: (a) Refractive index of four i-a-SiO$_x$:H with different E_{04} as a function of wavelength.(b) Extinction coefficient of four i-a-SiO$_x$:H with different E_{04} as a function of wavelength

The interpolated n and k data for the intrinsic layers for the intermediate bandgap energy values are obtained using an interpolation algorithm called gridfit. Gridfit [86] is an algorithm used in matlab which allows the user to model a surface from the data of the form $z(x, y)$ from scattered or semi-scattered data. The user can input the number of data points that one wishes to interpolate to. With just the n and k data from 14 intrinsic layers with different bandgap energies, the n and k data for 54 intrinsic layers can be obtained each with 54 different bandgap energies. A contour plot of both the refractive index n and extinction coefficient k as a function of both wavelength and bandgap energy are shown in Figure 6.2a and Figure 6.2b respectively.

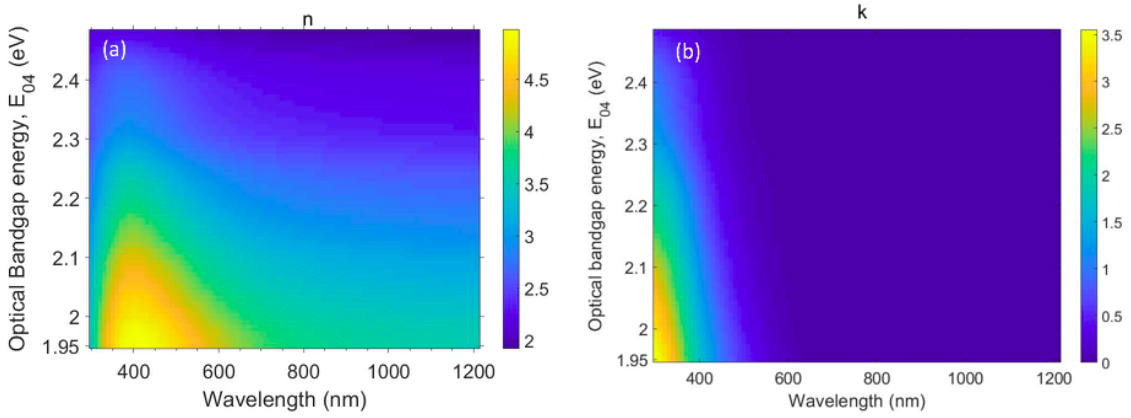

Figure 6.2: (a) Refractive index of four i-a-SiO$_x$:H with different E_{04} as a function of wavelength.(b) Extinction coefficient of four i-a-SiO$_x$:H with different E_{04} as a function of wavelength [19].

6.3. Method for simulating graded bandgap energy a-SiO$_x$:H solar cells

To simulate a graded bandgap energy i-a-SiO$_x$:H layer with a linearly graded bandgap energy, the linearly graded bandgap region was replaced with multiple layers (4, 10 and 20) with constant optical properties. A diagram depicting this model is shown in Figure 6.3. The main aim of this section is to look at how many layers might be required to replicate the absorbance A of a fabricated graded bandgap energy i-a-SiO$_x$:H layer. For this the absorbance obtained through simulations is matched to the absorbance of the fabricated

i-a-SiO$_x$:H layer by changing the number of graded layers.

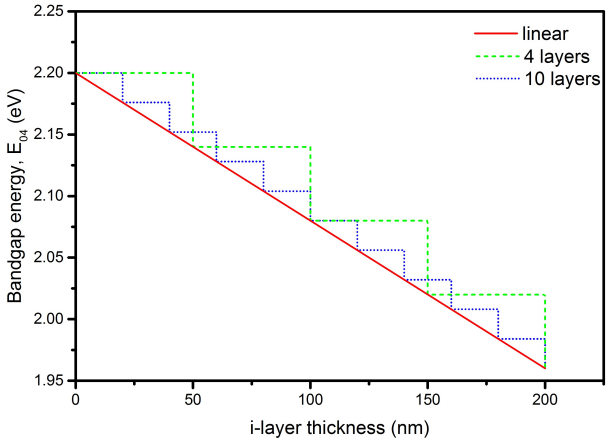

Figure 6.3: (a) Refractive index of four i-a-SiO$_x$:H with different E_{04} as a function of wavelength.(b) Extinction coefficient of four i-a-SiO$_x$:H with different E_{04} as a function of wavelength

In order to verify the accuracy of the simulation method 4 graded bandgap energy i-a-SiO$_x$:H layers are fabricated with their bandgap energies graded from 2.2 eV to 1.96 eV. Though for all four layers the bandgap energy is graded over the same region, they differ in i-layer thicknesses and grading profile as shown in Figure 6.4. Using GenPro4 simulation software and the n and k profile for i-a-SiO$_x$:H materials for various bandgap energies, multiple intrinsic layers are placed in a step-wise bandgap energy grading fashion as seen in Figure 6.3 can be simulated to obtain their absorbance and match it to the absorptance of the four fabricated graded bandgap energy i-a-SiO$_x$:H layers.

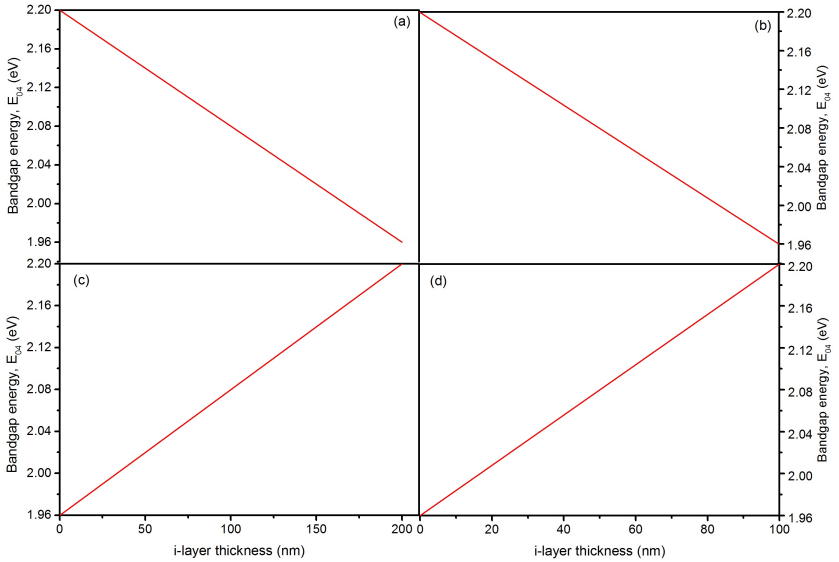

Figure 6.4: Four fabricated graded bandgap energy i-a-SiO$_x$:H layers with bandgap energies graded from 2.2 eV to 1.96 eV with the following cha (a) 2.2 eV - 1.96 eV 200 nm, (b) 2.2 eV - 1.96 eV 100 nm, (c) 1.96 eV - 2.2 eV 200 nm and (d) 1.96 eV - 2.2 eV 100 nm.

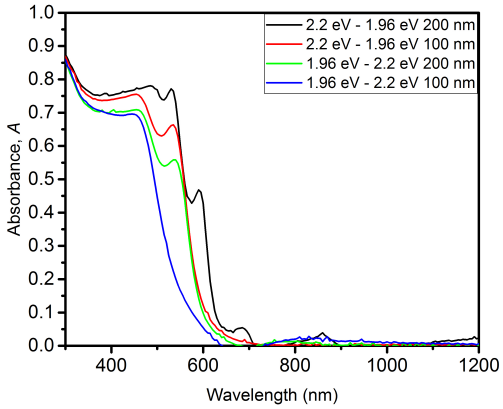

Figure 6.5: Absorbance A of the four fabricated graded bandgap energy i-a-SiO$_x$:H. The absorptance was measured using the Lambda 950 spectrophotometer.

Figure 6.5 shows the absorbance A obtained for the for fabricated graded bandgap energy intrinsic layers using the Lambda 950 spectrophotometer. In total three simulations are conducted on the four layers. The three simulations differ in the number of i-a-SiO$_x$:H layers used to replace the linearly graded region. The three simulations incorporated 4, 10 and 20 i-a-SiO$_x$:H layers. Figure 6.6 shows the absorbance obtained from the GenPro4 simulation software upon substituting the four linear bandgap energy graded intrinsic layers with 4, 10 and 20 intrinsic layers arranged in a step wise fashion of the bandgap energy. It can be seen that beyond 500 nm the simulated absorbance curves follow the measured curves for all the four samples with a maximum relative error of 15%. In the wavelength region of 300 nm - 500 nm the measured absorbance decreased from around 0.85 to 0.7. An absorbance of 0.85 measured at 300 nm for all the four samples does not correspond to the absorbance of the 2.2 eV or 1.96 eV layer, which are the first layers out of the 4, 10 and 20 layers utilized in the simulation through which the photons pass. At 300 nm the 1.96 eV intrinsic layer has a refractive index of 3.91 and the 2.2 eV intrinsic layer has a refractive index of 2.84. Using the Fresnel equation under normal incidence (angle of incidence = angle of transmission) as shown in Equation 6.1 we can obtain the maximum reflectance R_{max} at a certain wavelength between to mediums.

$$R_{max} = \left| \frac{n_1 - n_2}{n_1 + n_2} \right|^2 \tag{6.1}$$

We get,

$$R_{max} \text{ for 1.96 eV i-layer at 300 nm} = 0.30 \tag{6.2}$$

$$R_{max} \text{ for 2.2 eV i-layer at 300 nm} = 0.23 \tag{6.3}$$

Under the condition of zero transmittance, the maximum absorbance :

$$A_{max} \text{ for 1.96 eV i-layer at 300 nm} = 1 - 0.30 = 0.70 \tag{6.4}$$

$$A_{max} \text{ for 2.2 eV i-layer at 300 nm} = 1 - 0.23 = 0.77 \tag{6.5}$$

Equation 6.2 and Equation 6.3 show the maximum reflectance of a i-a-SiO$_x$:H layer with bandgap energy of 1.96 eV and 2.2 eV respectively. Supposing that there was zero transmittance, the maximum absorbance attainable for the 1.96 eV layer and the 2.2 eV intrinsic layer can be solved and are shown in Equation 6.4 and Equation 6.5. From the equations it can be seen that it would be impossible for both the 1.96 eV i-layer and the 2.2 eV i-layer to show an absorbance of 0.85 at 300 nm. This observations suggests that the layer has different properties.

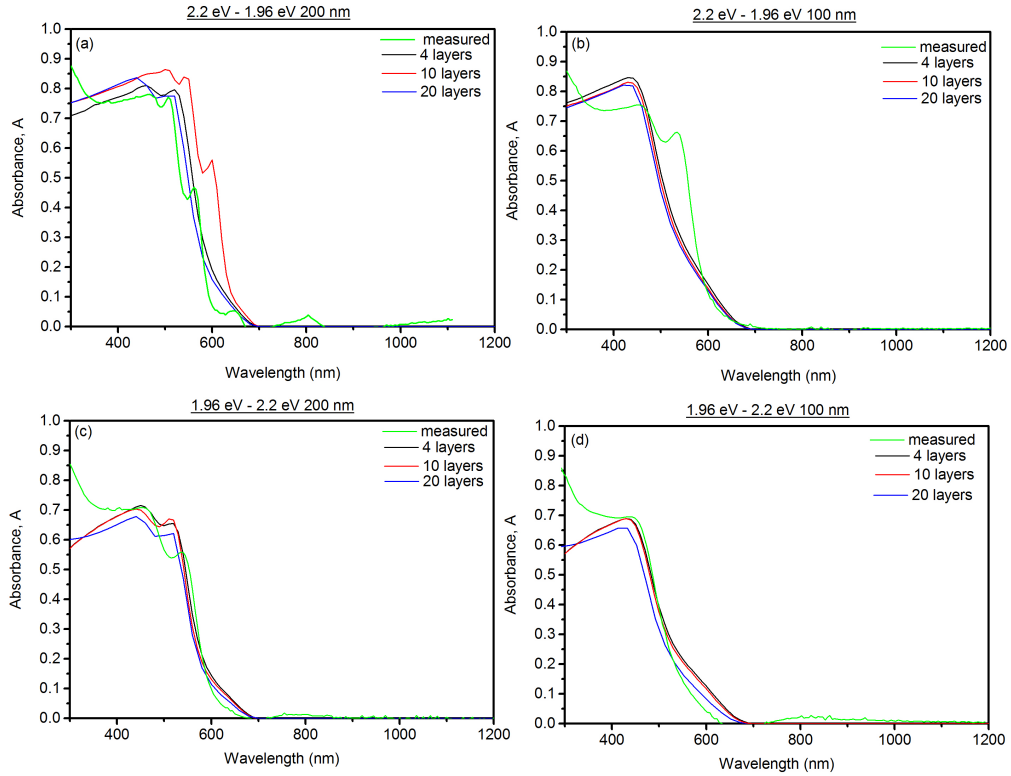

Figure 6.6: Simulated absorbance curves for graded bandgap i-a-SiO$_x$:H layers, with the linear graded bandgap region replaced by 4, 10 and 20 layers with constant optical properties for: (a) 2.2 eV - 1.96 eV 200 nm; (b) 2.2 eV - 1.96 eV 100 nm; (c) 1.96 eV - 2.2 eV 200 nm; and (d) 1.96 eV - 2.2 eV 100 nm.

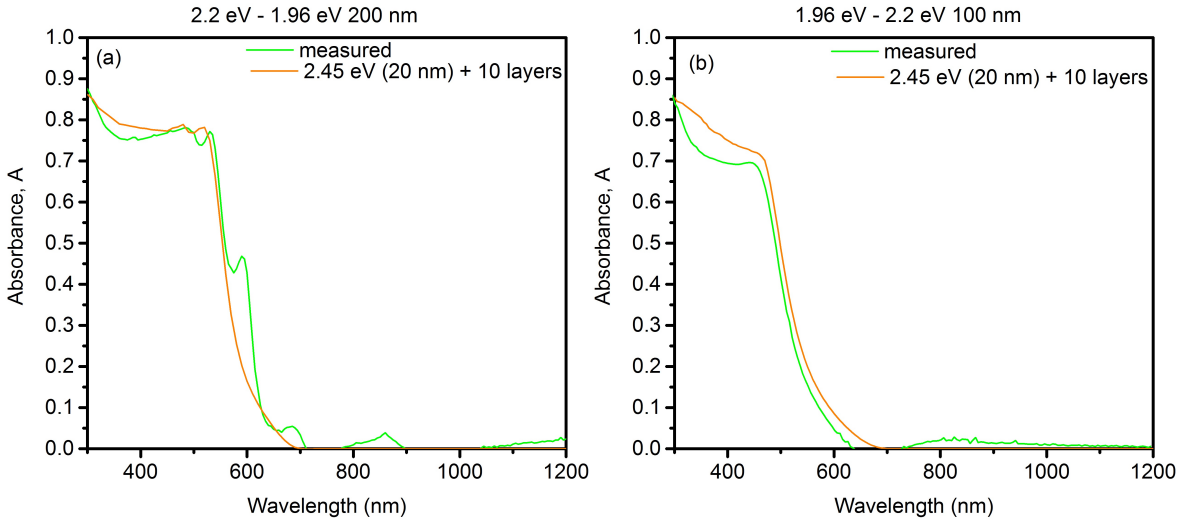

Figure 6.7: Simulated absorptance curves upon adding a 20 nm thick 2.45 eV i-a-SiO$_x$:H added in between the glass substrate and the linear graded bandgap region replaced with 10 layers having constant optical properties for: (a) 2.2 eV - 1.96 eV 200 nm sample; (b) and 1.96 eV - 2.2 eV 100 nm samples.

In order to improve the match of the simulated absorbance at shorter wavelengths, we assume additional layers have been incorporated during the deposition. At first it was speculated that a low bandgap material might have formed after the deposition process of the graded bandgap layer for all the four samples. After conducting several simulations by placing several low bandgap energy layers, it did not yield a high absorbance in the lower wavelength region of the visible region.

Upon performing further simulations on varying the position, thickness and the bandgap energy of the parasitic layer, it was found that a high bandgap material is deposited before the graded bandgap energy layer was. The simulated absorbance on placing a high bandgap energy layer before the 10 intrinsic layers oriented in a step-wise grading is shown in Figure 6.7. A 20 nm thick 2.45 eV i-a-SiO$_x$:H layer was selected as the high bandgap energy material and using this layer, the absorbance at the shorter wavelengths were matched satisfactorily. This can be explained by the observation that during the initial stages of film growth a hydrogen rich or low density overlayer is formed with a wide bandgap energy which can lasts for upto 50 nm of the bulk film thickness [87]. In this case the high bandgap energy material was for upto 20 nm of the film thickness. Since, going above the 20 nm thickness of the parasitic layer only shifted the absorbance contribution among the several layers simulated on GenPro4, meaning that a thicker 2.45 eV intrinsic layer will absorb the photons which would have been absorbed by the next layer.

For simulating the graded bandgap energy a-SiO$_x$:H solar cells, a 10 layer configuration will be used to mimic the linear graded bandgap energy intrinsic layer, without the addition of the high bandgap energy parasitic layer.

6.4. Results for the simulated graded bandgap energy a-SiO$_x$:H solar cells

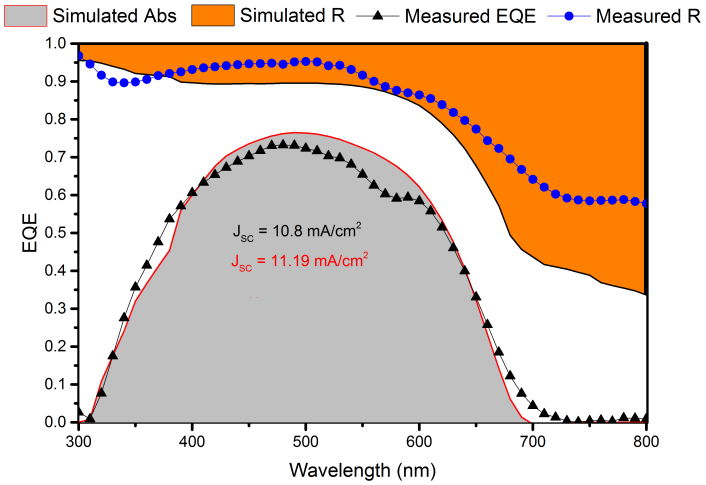

Figure 6.8: Simulated and measured EQE and reflectance R for the reference a-SiO$_x$:H solar cell.

Figure 6.8 shows the EQE curves obtained from the measuring and the absorbance from the simulation obtained from GenPro4. Also, the J_{SC} associated with the EQE curves are shown in Figure 6.8. The simulated absorbance shows a satisfactory match to the EQE of the reference cell except in the wavelength region between 500 nm and 650 nm. The measured and simulated reflectance of the reference cell is also shown inFigure 6.8. The measured and simulated reflectance curves do not match at all.

In the previous section, it was concluded that in order to simulate the graded bandgap energy intrinsic layer, 10 intrinsic layer with different bandgap energies are placed in a step wise fashion is utilized in GenPro4 simulations. In this section, the simulations are conducted to the graded bandgap energy a-SiO$_x$:H cells on varying the p-i and i-n region grading widths. The simulations conducted are the same as the experiments conducted in Chapter 4. In the first set of simulations, the p-i grading width is varied while the i-n grading width of the intrinsic layer is kept constant at 100 nm. In the second set of simulations, the i-n region grading width is varied as the p-i region grading width is kept constant at 10 nm. Figure 6.9 and Figure 6.12 show the results on simulations of the graded bandgap energy a-SiO$_x$:H solar cells as a function of varying p-i region grading width. Figure 6.11 and Figure 6.12 show the results on simulations of the graded bandgap energy a-SiO$_x$:H solar cells as a function of varying the i-n region grading width.

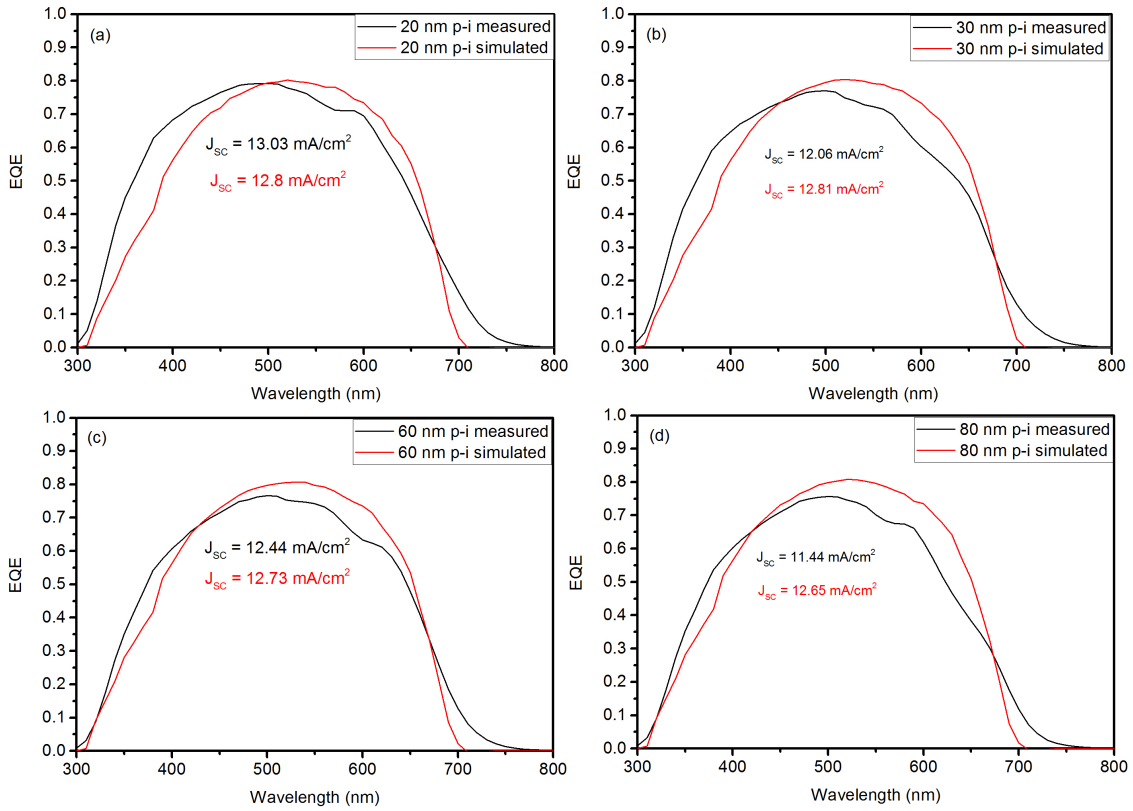

Figure 6.9: The measured and simulated EQE for graded bandgap energy a-SiO$_x$:H solar cells with a constant grading width of 100 nm in the p-i region. a-SiO$_x$:H cells labelled (a) 20 nm p-i grading width (b) 30 nm p-i grading width (c) 60 nm p-i grading width (d) 80 nm p-i grading width.

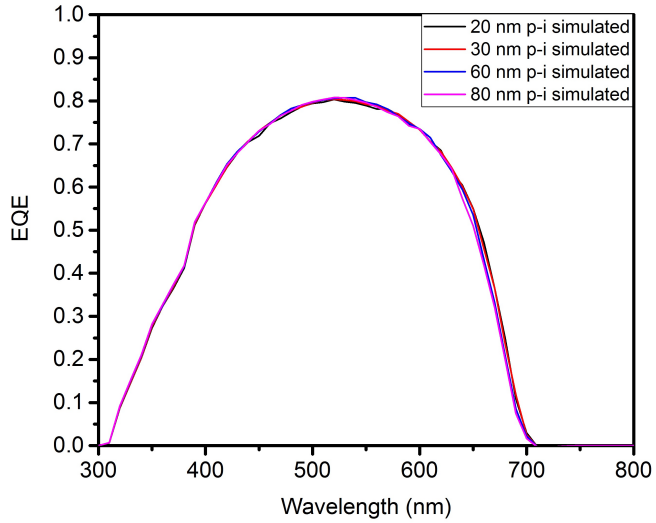

Figure 6.10: simulated EQE/absorbance curves of the simulated graded bandgap energy a-SiO$_x$:H solar cells as function of p-i grading width.

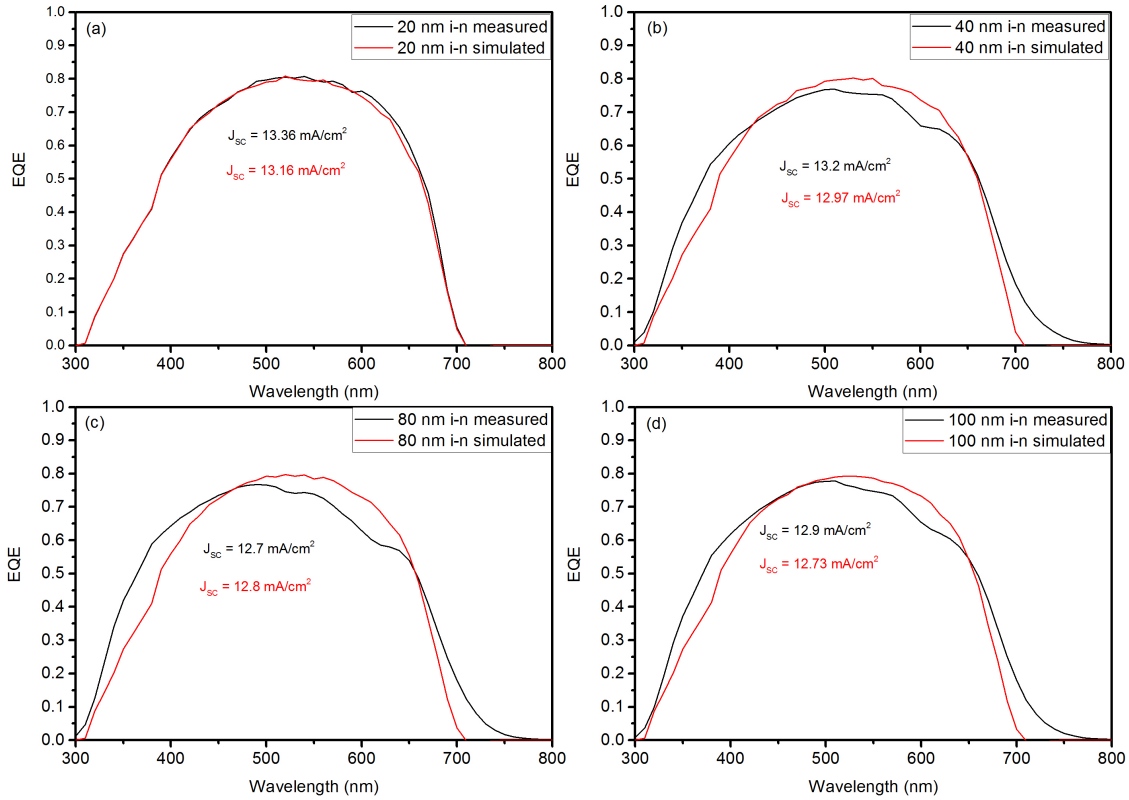

Figure 6.11: The measured and simulated EQE for graded bandgap energy a-SiO$_x$:H solar cells with a constant grading width of 100 nm in the p-i region. a-SiO$_x$:H cells labelled (a) 20 nm i-n grading width (b) 40 nm i-n grading width (c) 80 nm i-n grading width (d) 100 nm i-n grading width.

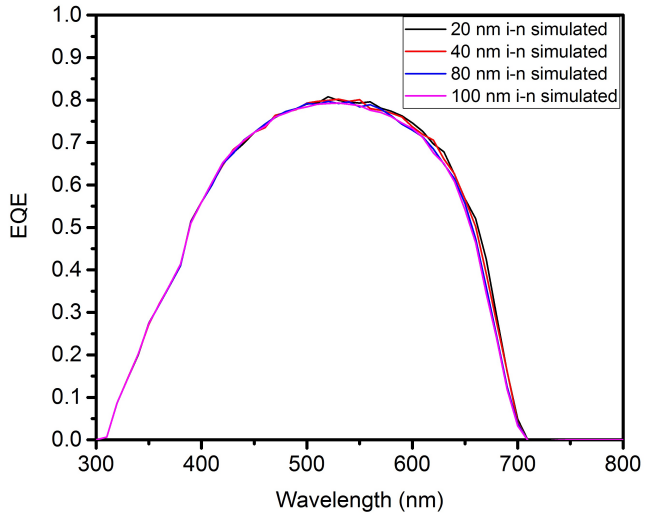

Figure 6.12: simulated EQE/absorbance curves of the simulated graded bandgap energy a-SiO$_x$:H solar cells as function of i-n grading width.

First observation in comparing the EQE of the experimental cells to the simulations in Figure 6.9 and Figure 6.11 is how the graded bandgap energy experimental cells showed higher response than those simulated. The simulated cells showed a higher response in the middle and longer wavelength regions.

The second observation is in the change of the EQE curves upon increasing grading width at the p-i and i-n region. In the experimental cells as seen in Figure 4.4 and Figure 4.8, upon increasing the grading width the response in the lower wavelength region increases then decreases and in the longer wavelength region the response decreases. Figure 6.10 and Figure 6.12 shows the change in EQE received from simulations upon varying the p-i and i-n region grading widths. In the simulated EQE curves, on increasing the grading width the response between 300 nm and 500 nm did not increase and then decrease upon further increase in grading width but remains almost the same without much significant change. In the longer wavelength region the simulated EQE curves shows the response decreasing in small units with increasing the grading width in the p-i and i-n region of the intrinsic layer.

The third observation is that some of the experimental cells showed higher J_{SC} than the simulated cells. Generally, the absorbance of the absorber layer is usually higher than the EQE of the solar cell. This is because not all the photons absorbed gives rise to charge carriers and some are absorbed in the inactive layers. But, the simulations for few cells showed lower J_{SC} values in comparison to their experimental counterparts.

Overall, only the decrease in J_{SC} obtained from simulations on increasing the grading width matches the trend observed with the experimental cells. The simulation results did not match the experimental results despite the attempt on matching the absorbance of the graded bandgap energy i-layer in Section 6.2. The possible theory as to the mismatch between the simulation and experimental results is that the simulation software does not take into consideration the electrical properties and the effects of a graded bandgap energy cell. Though this theory is not confirmed in this work, there are two possible ways to test this theory. First, is to implement a software that takes into account the optical and electrical properties of the solar cells into the simulation. Second, is to measure the EQE at a sufficiently large reverse bias voltage. At 0 V, the photocurrent density equals the J_{SC} [36]. By measuring the EQE at a reverse voltage bias, one can collect nearly every photo-generated charge carrier and observe how the EQE curve differs from the simulated EQE.

6.5. Conclusions

The first part of this chapter focused on obtaining the refractive index n and extinction coefficient k for i-a-SiO_x:H layer for different bandgap energies using a mixture of interpolation and smoothing of the n and k data obtained from SE measurements. This was followed by using the n and k obtained for various bandgap energies and trying to match the absorbance of the four fabricated graded bandgap energy a-SiO_x:H layers to the simulated absorbance. In simulations, the linearly graded bandgap energy i-layer was replaced with several i-layers with different bandgap energies in a step wise fashion. It was found that substituting the linearly graded bandgap energy i-layer with multiple layers with constant optical properties, the absorbance of the graded layers can be simulated with very little deviation. Finally, the graded bandgap energy solar cells were simulated with the graded bandgap energy sections being substituted with 10 i-layers with different bandgap energies oriented in a step wise fashion. Despite matching the absorbance of the graded bandgap energy regions, the solar cells simulated did not match their experimental counterparts. Further improvements and study on the graded bandgap energy solar cells is required in order to simulate the effects of implementing a graded bandgap energy absorber layer to solar cells.

7

Conclusion & Recommendations

7.1. Conclusion

This chapter provides a conclusion to this work. In chapter 1 the main objective of this thesis was presented and it was as follows:

To linearly grade the bandgap energy of a-SiO_x:H solar cell in order to increase the J_{SC} of the cell without effecting the high $V_{OC}\times$ FF product.

In this work a-SiO_x:H solar cells were fabricated with a linearly graded bandgap energy absorber layer to increase the J_{SC} of the cell. In chapter 3, the deposition rate and the bandgap energy as a function of gas flow ratio was discussed. After which an equation for obtaining the gas flow ratio as a function of deposition time was derived for depositing the linearly graded bandgap energy i-a-SiO_x:H layer. The derived formula was :

$$r(t) = \sqrt{K \cdot t + r^2(t_1)}; t \rightarrow (0, t_2) \tag{7.1}$$

Using Equation 7.1 derived in chapter 3, graded bandgap energy a-SiO_x:H solar cells are deposited. Chapter 4 focuses on the optimization of the grading width for the graded bandgap energy a-SiO_x:H solar cells. All the cells fabricated in this work are compared to two cells: (1) a reference a-SiO_x:H solar cell; and (2) a 1.96 eV flat bandgap energy cell. The optimization of the grading width are performed in two sets of experiments. The first set is to optimize the grading width in the p-i region and the second set is to optimize the grading width in the i-n region of the i-a-SiO_x:H layer. The cells fabricated have a bandgap energy grading from 2.1 eV to 1.96 eV and the total absorber layer thickness was 200 nm. The results presented in both the sets of experiments shows that as the grading width increased the J_{SC} decreased. Also, as the grading width increases the response at the shorter wavelengths increases and after a certain grading width the response at that region decreases. This is beneficial for 4T solar cells, where a higher response in the lower wavelength region for the top cell can increase the efficiency gained by the bottom cell. Increasing the grading width did increase the V_{OC} and the FF decreases in comparison to the reference and the 1.96 eV flat bandgap energy cell. The highest J_{SC} is observed in the cell with a 10 nm p-i region grading width and 20 nm i-n region grading width with a value of 13.4 $\pm$ 0.2 mA/cm^2 which is higher in comparison to the reference a-SiO_x:H with a value 10.84 $\pm$ 0.01 mA/cm^2. But, the $V_{OC}\times$ FF product, which is 0.62 $\pm$ 0.01 V for the cell with 10 nm p-i and 20 nm i0n grading is found to be lower than the reference cell which has a $V_{OC}\times$ FF product of 0.65 $\pm$ 0.04 V and same to the $V_{OC}\times$ FF product of the 1.96 eV flat bandgap energy cell. The main observation is to keep the p-i and i-n grading width as small as possible in order to attain a high J_{SC} for a-SiO_x:H solar cells, without compromising the high $V_{OC}\times$ FF product. Another observation is that none of the graded bandgap energy cell showed a higher J_{SC} than that of the 1.96 eV flat bandgap energy cell.

The effect of varying the grading height (i.e keeping $E_{04,min}$ constant at 1.96 eV and varying $E_{04,max}$) is discussed in chapter 5. Increasing the $E_{04,max}$ did not show any trend in the V_{OC} and the FF decreases. The J_{SC} decreases with increasing the $E_{04,max}$ of the bandgap energy grading. All the cells developed shows J_{SC} higher

than the reference cell but lower than the 1.96 eV flat bandgap energy cell. Moreover, as $E_{04,max}$ increases the response of the cells decreases at shorter wavelengths of the visible spectrum.

An a-SiO_x:H solar cell is made with a bandgap energy grading from 2.1 eV to 1.92 eV and a 10 nm and 20 nm grading width at the p-i and i-n region respectively . The cell is graded to a lower E_{04} aiming for a higher J_{SC}. In the cells fabricated with a bandgap energy grading of 2.1 eV to 1.96 eV, the grading is made possible by manipulating the SiH_4 and CO_2 gas flows. But, in order to grade the bandgap energy to an even lower value of 1.92 eV, the H_2 is also manipulated to decrease the bandgap energy after the CO_2 and SiH_4 gas flows are manipulated to a gas flow ratio of zero. The cell deposited shows a J_{SC} value of 13.95 ± 0.03 mA/cm^2 but exhibits a low V_{OC}× FF product of 0.55 ± 0.01. The low V_{OC}× FF product is a consequence of both the V_{OC} and the FF, but the high J_{SC} pushes the cell to an efficiency of 7.7 ± 0.1 %.

Graded bandgap energy a-SiO_x:H solar cells with bandgap energy grading from 2.1 eV to 1.96 eV and a 10 nm and 20 nm grading width at the p-i and i-n region respectively are fabricated, but with varying i-layer thicknesses. As the thickness of the i-layer increases, the J_{SC} increases and the V_{OC}× FF product decreases. The J_{SC} obtained was the highest of all the cells developed in this work, with a value of 14.4 ± 0.3 mA/cm^2. The efficiency of most of the cells fabricated stayed within an efficiency range of 7.5% - 8%. This is different to the results observed in the work by Kim et al. [7], where the cells with varying i-layer thickness did not stay within the same efficiency range.

Finally, chapter 6 focuses on the optical simulation of graded bandgap energy a-SiO_x:H solar cells. By obtaining the wavelength dependent n and k for a limited number of i-a-SiO_x:H layer of different bandgap energies, the n and k for the intermediate bandgap energies i-layers are interpolated from 1.95 eV to 2.48 eV for every 0.01 eV. Upon obtaining the n and k data for the various bandgap energies the absorbance of four graded bandgap energy i-a-SiO_x:h layer were measured and matched to the simulated absorbance by replacing the linear grading with multiple layers having constant optical properties. Simulations for the graded bandgap energy cells are preformed by utilizing multiple layers (in this case, 10 layers) to replace the graded bandgap regions. It is found that the simulation results does not match the experimental results, despite matching the absorbance of the graded bandgap layer and requires more attention.

7.2. Recommendations

The differences in J_{SC} between the reference cell and the graded bandgap energy cells were large. But, the grading did not show a satisfactory increase in the V_{OC} and FF. The p-, n- and buffer layers of the cells developed in this work were optimized for an absorber layer with a bandgap energy of 2.02 eV in the work by Erwin Guijt and Do Yun Kim [88]. Optimizing the p-, n- and buffer layers of the cell for the graded bandgap energy absorber layer can further improve the V_{OC} and FF of the cell and the results can be promising. Also using another substrate, TCO and implementing an anti-reflective coating can easily push the efficiency beyond the current world record efficiency of 8.8% for a-SiO_x:H solar cells [63].

a-SiO_x:H solar cells used as a top cell in tandem cell configurations are observed to be current limiting [7]. Kim et al. [7] showed that the maximum achievable J_{SC} from increasing the i-layer thickness is limited by a certain thickness, as beyond that thickness the efficiency drops drastically. But graded bandgap energy a-SiO_x:H cells exhibit a high J_{SC} and efficiency in comparison to a-SiO_x:H solar cells of the same i-layer thickness and without bandgap grading. It would be interesting to observe the performance of graded bandgap a-SiO_x:H with i-layer thickness from 250 nm - 300 nm utilized as a top cell in a tandem cell configuration.

Chaudhary [9] recommended that the efficiency of a crystalline silicon based solar cell can be increased by using an a-SiO_x:H solar cell as a top cell in a 4T configuration and the efficiency gained can be further increased by increasing the response of the top cell in the blue region. Graded bandgap energy cells can be applied in a 4T configuration to increase the efficiency gain of the bottom cell. In chapter 4, it has been shown that the response in the blue region increases when the grading width increases. Two cells fabricated in this work can be recommended for increasing the efficiency gained by c-Si solar cells in a 4T configuration; (1) an a-SiO_x:H cell with a p-i grading width of 30 nm and i-n grading width of 100 nm; and (2) an a-SiO_x:H solar cell with a p-i grading width of 10 nm and i-n grading width of 80 nm.

The simulations performed for the graded bandgap energy solar cells in this work did not match the results obtained for the experimental solar cells. It was postulated, that the reason for the mismatch is that the simulation does not take into consideration the electrical properties and the effects of grading the bandgap energy on the performance of the solar cells. For future work, electrical simulations need to be performed and also measuring the EQE of the graded bandgap energy solar cells under a significant reverse bias can help in providing a better understanding on the effects of bandgap energy grading.

Finally, the 1.96 eV flat bandgap energy a-SiO_x:H solar cell surprisingly showed a high efficiency of 8.5 ± 0.1 %. It is 0.3% short of a a-SiO_x:H cell with a world record efficiency of 8.8 % [63]. optimizing the other layers of the solar cell, can easily push the efficiency beyond the current world record. It also needs to be noted that for a 200-nm thick absorber layer, the 1.96 eV flat bandgap energy solar cell shows the highest J_{SC} among the other solar cells with the same absorber layer thickness. It would be interesting to observe the V_{OC}× FF product vs. J_{SC} performance of this solar on increasing the i-layer thickness. Further investigations need to conducted on graded bandgap energy a-SiO_x:H solar cells. For instance a look into the elemental composition of the graded bandgap layer using x-ray photoelectron spectroscopy, lifetime measurements and a look into light induced effects.

Bibliography

[1] *World Energy Resources Full Report 2016*, World Energy Council, 2016.

[2] X. Ziang, L. Shifeng, Q. Laixiang, P. Shuping, W. Wei, Y. Yu, Y. Li, C. Zhijian, W. Shufeng, D. Honglin *et al.*, "Refractive index and extinction coefficient of ch 3 nh 3 pbi 3 studied by spectroscopic ellipsometry," *Optical Materials Express*, vol. 5, no. 1, pp. 29–43, 2015.

[3] A. Smets, K. Jäger, O. Isabella, M. Zeman, and R. van Swaaij, *Solar Energy: The Physics and Engineering of Photovoltaic Conversion, Technologies and Systems*. UIT Cambridge, 2016. [Online]. Available: https://books.google.nl/books?id=vTkdjgEACAAJ

[4] M. G. Kumbhare and P. Sathya, "Design and analysis of indium gallium nitride based pin solar cell," *International Journal of Renewable Energy Research (IJRER)*, vol. 6, no. 3, pp. 1159–1166, 2016.

[5] O. Nordseth, R. Kumar, K. Bergum, L. Fara, I. Chilibon, S. Foss, E. Monakhov, and B. Svensson, "Boosting the performance of silicon based tandem cells using non-toxic metal oxides," *Laboratory journal*, 2017.

[6] A. McEvoy, T. Markvart, L. Castañer, T. Markvart, and L. Castaner, *Practical handbook of photovoltaics: fundamentals and applications*. Elsevier, 2003.

[7] D. Y. Kim, E. Guijt, F. T. Si, R. Santbergen, J. Holovskỳ, O. Isabella, R. A. van Swaaij, and M. Zeman, "Fabrication of double-and triple-junction solar cells with hydrogenated amorphous silicon oxide (a-siox: H) top cell," *Solar Energy Materials and Solar Cells*, vol. 141, pp. 148–153, 2015.

[8] P. Babal, "Doped nanocrystalline silicon oxide for use as (intermediate) reflecting layers in thin-film silicon solar cells, msc thesis, tu delft," 2014.

[9] A. Chaudhary, "Development of four-terminal mechanically-stacked solar cells utilising hydrogenated amorphous silicon oxide (a-sio$_x$:h) and crystalline silicon cells," Master's thesis, Delft University of Technology, 2017.

[10] G. Yang, "High-efficient nip thin-film silicon solar cells," 2015.

[11] J. Co. Ellipsometry tutorial. [Online]. Available: https://www.jawoollam.com/resources/ellipsometry-tutorial

[12] P. INC. Applications and use of integrating spheres with the lambda 650 and 850 uv/vis and lambda 950 uv/vis/nir spectrophotometers. [Online]. Available: https://www.ophiropt.com/blog/laser-measurement/what-is-an-integrating-sphere/

[13] D. Neamen, "semiconductor physics and device 4th ed," 2003.

[14] M. Konagai and K. Takahashi, "Graded-band-gap p ga1- x al x as-n gaas heterojunction solar cells," *Journal of Applied Physics*, vol. 46, no. 8, pp. 3542–3546, 1975.

[15] S. Guha, J. Yang, A. Pawlikiewicz, T. Glatfelter, R. Ross, and S. Ovshinsky, "Band-gap profiling for improving the efficiency of amorphous silicon alloy solar cells," *Applied Physics Letters*, vol. 54, no. 23, pp. 2330–2332, 1989.

[16] L. Olsen, "Graded bandgap solar cells," *Washington Univ. Seattle Tech. Rep.*, 1989.

[17] T. Krajangsang, S. Inthisang, A. Dousse, A. Moollakorn, A. Hongsingthong, S. Kittisontirak, P. Chinnavornrungsee, A. Limmanee, J. Sritharathikhun, and K. Sriprapha, "Band gap profiles of intrinsic amorphous silicon germanium films and their application to amorphous silicon germanium heterojunction solar cells," *Optical Materials*, vol. 51, pp. 245–249, 2016.

[18] M. R. R. Luna, "Band gap grading of a–siox:h and its effect on the performance of thin film solar cells," Master's Thesis, Delft University of Technology, Delft, Netherlands, 2017.

[19] *adapted from a figure made by Dr. Rudi Santbergen*, PVMD, TU Delft, 2018.

[20] I. E. Agency. International energy agency: World energy balance and world energy statistics summarised. [Online]. Available: https://www.iea.org/newsroom/news/2016/august/iea-data-shows-global-energy-production-and-consumption-continue-to-rise.html

[21] *World Population Prospects: The 2016 Revision, Key Findings and Advance Tables*, United Nations Department of Economic and Social Affairs/Population Division UN DESA, 2016.

[22] *International Energy Outlook 2017*, U.S Energy Information Administration, 2017.

[23] *International Energy Outlook 2017*, U.S Energy Information Administration, 2018.

[24] *Powering the future: mapping our low-carbon path to 2050*, Parsons Brinckerhoff, 2009.

[25] *BP Statistical Review of World Energy*, BP, 2009.

[26] *World Nuclear Association*, Supply of uranium, 2009.

[27] I. Skeet, "Geopolitics of energy," *Energy Exploration & Exploitation*, vol. 14, no. 3/4, pp. 265–272, 1996. [Online]. Available: http://www.jstor.org/stable/43866316

[28] L. R. Brown, *State of the World, 1998: A Worldwatch Institute Report on Progess Toward a Sustainable Society*. WW Norton & Company, 1997.

[29] S. I. Rasool and S. H. Schneider, "Atmospheric carbon dioxide and aerosols: Effects of large increases on global climate," *Science*, vol. 173, no. 3992, pp. 138–141, 1971.

[30] *Energy From the Sun: Student Guide*, National Energy Education Development Project, 2017.

[31] *Solar energy FAQ*, Sandia National Laboratory, 2007.

[32] G. Resch, A. Held, T. Faber, C. Panzer, F. Toro, and R. Haas, "Potentials and prospects for renewable energies at global scale," *Energy policy*, vol. 36, no. 11, pp. 4048–4056, 2008.

[33] T. Vernon. Improving solar energy efficiency. [Online]. Available: https://www.firstchoicepower.com/the-light-lab/green-power/improving-solar-energy-efficiency/

[34] *Renewable Power Generation Costs in 2017*, International Renewable Energy Agency, 2017.

[35] J. Fialka. Are we entering the photovoltaic energy era? [Online]. Available: https://www.scientificamerican.com/article/are-we-entering-the-photovoltaic-energy-era/

[36] O. Isabella, A. Smets, K. Jäger, M. Zeman, and R. van Swaaij, "Solar energy: The physics and engineering of photovoltaic conversion, technologies and systems," *UIT Cambridge Limited*, 2016.

[37] *Photovoltaics Report*, Fraunhofer Institute for Solar Energy Systems (ISE), 2017.

[38] K. Yoshikawa, H. Kawasaki, W. Yoshida, T. Irie, K. Konishi, K. Nakano, T. Uto, D. Adachi, M. Kanematsu, H. Uzu *et al.*, "Silicon heterojunction solar cell with interdigitated back contacts for a photoconversion efficiency over 26%," *Nature Energy*, vol. 2, no. 5, p. 17032, 2017.

[39] A. Richter, M. Hermle, and S. W. Glunz, "Reassessment of the limiting efficiency for crystalline silicon solar cells," *IEEE Journal of Photovoltaics*, vol. 3, no. 4, pp. 1184–1191, 2013.

[40] M. Zeman, J. Willemen, L. Vosteen, G. Tao, and J. Metselaar, "Computer modelling of current matching in a-si: H/a-si: H tandem solar cells on textured tco substrates," *Solar Energy Materials and Solar Cells*, vol. 46, no. 2, pp. 81–99, 1997.

[41] S. Reynolds and V. Smirnov, "Modelling performance of two-and four-terminal thin-film silicon tandem solar cells under varying spectral conditions," *Energy procedia*, vol. 84, pp. 251–260, 2015.

[42] Y. Hamakawa, *Thin-film solar cells: next generation photovoltaics and its applications*. Springer Science & Business Media, 2013, vol. 13.

[43] A. Madan, "Flexible solar cells and stable high-efficiency four-terminal solar cells using thin-film silicon technology," *Materials and manufacturing processes*, vol. 22, no. 4, pp. 412–418, 2007.

[44] S. Essig, M. A. Steiner, C. Allebe, J. F. Geisz, B. Paviet-Salomon, S. Ward, A. Descoeudres, V. LaSalvia, L. Barraud, N. Badel *et al.*, "Realization of gainp/si dual-junction solar cells with 29.8% 1-sun efficiency," *IEEE Journal of Photovoltaics*, vol. 6, no. 4, pp. 1012–1019, 2016.

[45] S. Hassan, "Four-terminal mechanically stacked gaas/si tandem solar cells," *arXiv preprint arXiv:1505.06711*, 2015.

[46] R. Chittick, J. Alexander, and H. Sterling, "The preparation and properties of amorphous silicon," *Journal of the Electrochemical Society*, vol. 116, no. 1, pp. 77–81, 1969.

[47] D. E. Carlson, "Semiconductor device having a body of amorphous silicon," Dec. 20 1977, uS Patent 4,064,521.

[48] W. Spear and P. Le Comber, "Substitutional doping of amorphous silicon," *Solid state communications*, vol. 17, no. 9, pp. 1193–1196, 1975.

[49] M. Brodsky, M. Frisch, J. Ziegler, and W. Lanford, "Quantitative analysis of hydrogen in glow discharge amorphous silicon," *Applied Physics Letters*, vol. 30, no. 11, pp. 561–563, 1977.

[50] X. Deng and E. A. Schiff, "Amorphous silicon based solar cells," 2003.

[51] D. Staebler and C. Wronski, "Reversible conductivity changes in discharge-produced amorphous si," *Applied physics letters*, vol. 31, no. 4, pp. 292–294, 1977.

[52] A. Kołodziej, "Staebler-wronski effect in amorphous silicon and its alloys," *Opto-electronics review*, vol. 12, no. 1, pp. 21–32, 2004.

[53] H. M. Branz and M. Silver, "Potential fluctuations due to inhomogeneity in hydrogenated amorphous silicon and the resulting charged dangling-bond defects," *Physical Review B*, vol. 42, no. 12, p. 7420, 1990.

[54] L. Jiao, H. Liu, S. Semoushikina, Y. Lee, and C. Wronski, "Initial, rapid light-induced changes in hydrogenated amorphous silicon materials and solar cell structures: The effects of charged defects," *Applied physics letters*, vol. 69, no. 24, pp. 3713–3715, 1996.

[55] M. Güneş and C. R. Wronski, "Differences in the densities of charged defect states and kinetics of staebler–wronski effect in undoped (nonintrinsic) hydrogenated amorphous silicon thin films," *Journal of applied physics*, vol. 81, no. 8, pp. 3526–3536, 1997.

[56] D. Carlson and C. Wronski, "Solar cells using discharge-produced amorphous silicon," *Journal of Electronic Materials*, vol. 6, no. 2, pp. 95–106, 1977.

[57] D. Carlson, C. Wronski, A. Triano, and R. Daniel, "Solar cells using schottky barriers on amorphous silicon," in *12th Photovoltaic Specialists Conference*, 1976, pp. 893–895.

[58] K. Yamamoto, A. Nakajima, M. Yoshimi, T. Sawada, S. Fukuda, T. Suezaki, M. Ichikawa, Y. Koi, M. Goto, T. Meguro *et al.*, "A high efficiency thin film silicon solar cell and module," *Solar Energy*, vol. 77, no. 6, pp. 939–949, 2004.

[59] P. Zanzucchi, C. Wronski, and D. E. Carlson, "Optical and photoconductive properties of discharge-produced amorphous silicon," *Journal of Applied Physics*, vol. 48, no. 12, pp. 5227–5236, 1977.

[60] G. Nakamura, K. Sato, T. Ishihara, M. Usui, K. Okaniwa, and Y. Yukimoto, "Tandem type amorphous solar cells," *Journal of Non-Crystalline Solids*, vol. 59, pp. 1111–1114, 1983.

[61] T. Markvart and L. Castafier, "Handbook of photovoltaics: Section finder."

[62] D. Y. Kim, E. Guijt, R. A. Swaaij, and M. Zeman, "Development of a-sio$_x$:h solar cells with very high voc× ff product," *Progress in Photovoltaics: Research and Applications*, vol. 23, no. 6, pp. 671–684, 2015.

[63] D. Y. Kim, E. Guijt, R. A. van Swaaij, and M. Zeman, "Hydrogenated amorphous silicon oxide (a-sio x: H) single junction solar cell with 8.8% initial efficiency by reducing parasitic absorptions," *Journal of Applied Physics*, vol. 121, no. 13, p. 133103, 2017.

[64] D. Zhang, W. Soppe, and R. E. Schropp, "Design of 4-terminal solar modules combining thin-film wide-bandgap top cells and c-si bottom cells," *Energy Procedia*, vol. 77, pp. 500–507, 2015.

[65] I. Kavvadas, "Optimization of aluminum-doped zinc oxide front tco layer for different thin-film silicon solar cells," Master's thesis, Delft University of Technology, 2016.

[66] B. Institute of Physics. Rf magnetron sputterin. [Online]. Available: http://surface.iphy.ac.cn/sf03/sputtering.htm

[67] G. Yang, "High-efficient n-i-p thin-film silicon solar cells," Master's thesis, Delft University of Technology, 2015.

[68] C. S. Solanki, *Solar photovoltaics: fundamentals, technologies and applications*. PHI Learning Pvt. Ltd., 2015.

[69] O. P. Blog. What is an integrating sphere ? [Online]. Available: https://www.ophiropt.com/blog/laser-measurement/what-is-an-integrating-sphere/

[70] H. H. Ku, "Notes on the use of propagation of error formulas," *Journal of Research of the National Bureau of Standards*, vol. 70, no. 4, 1966.

[71] P. Emtage, "Electrical conduction and the photovoltaic effect in semiconductors with position-dependent band gaps," *Journal of Applied Physics*, vol. 33, no. 6, pp. 1950–1960, 1962.

[72] X. Chao, Y. Ruo-He, and G. Kui-Wei, "Photovoltage analysis of a heterojunction solar cell," *Chinese Physics B*, vol. 20, no. 5, p. 057302, 2011.

[73] R. Arya, A. Catalano, and R. Oswald, "Amorphous silicon p-i-n solar cells with graded interface," *Applied physics letters*, vol. 49, no. 17, pp. 1089–1091, 1986.

[74] J. Zimmer, H. Stiebig, and H. Wagner, "a-sige: H based solar cells with graded absorption layer," *Journal of applied physics*, vol. 84, no. 1, pp. 611–617, 1998.

[75] J. Folsch, H. Stiebig, F. Finger, B. Rech, D. Lundszien, A. Lambertz, and H. Wagner, "Role of bandgap grading for the performance of a-sige: H based solar cells," in *Photovoltaic Specialists Conference, 1996., Conference Record of the Twenty Fifth IEEE*. IEEE, 1996, pp. 1133–1136.

[76] J. P. Conde, D. Shen, V. Chu, and S. Wagner, "a-si: H, to or from a-si, ge: H, f graded-bandgap structures," *IEEE Transactions on Electron Devices*, vol. 36, no. 12, pp. 2834–2838, 1989.

[77] R. van Swaaij, M. Zeman, S. Arnoult, and J. Metselaar, "Performance dependence on grading width of a-sige: H component solar cells," in *Photovoltaic Specialists Conference, 2000. Conference Record of the Twenty-Eighth IEEE*. IEEE, 2000, pp. 869–872.

[78] H.-J. Hsu, C.-H. Hsu, and C.-C. Tsai, "Improvement of a-si1- xgex: H single-junction thin-film solar cell performance by bandgap profiling techniques," *Journal of Non-Crystalline Solids*, vol. 358, no. 17, pp. 2277–2280, 2012.

[79] A. Morales-Acevedo, "A simple model of graded band-gap cuingase2 solar cells," *Energy Procedia*, vol. 2, no. 1, pp. 169–176, 2010.

[80] G. F. Baldwin, "Analytical and numerical modeling of a graded band gap amorphous silicon based pin solar cell," 1992.

[81] D. Lundszien, F. Finger, and H. Wagner, "Band-gap profiling in amorphous silicon–germanium solar cells," *Applied physics letters*, vol. 80, no. 9, pp. 1655–1657, 2002.

[82] D. Lundszien and F. Finger, "A-si: H buffer in a-sige: H solar cells," *Solar energy materials and solar cells*, vol. 74, no. 1-4, pp. 365–372, 2002.

[83] I. M. Dharmadasa, A. A. Ojo, H. I. Salim, and R. Dharmadasa, "Next generation solar cells based on graded bandgap device structures utilising rod-type nano-materials," *Energies*, vol. 8, no. 6, pp. 5440–5458, 2015.

[84] R.Santbergen. Manual for solar cell optical simulation software: Genpro4. [Online]. Available: http://www.ewi.tudelft.nl/fileadmin/faculteit/ewi/documentenafdelingen/electricalsustainableenergy/pvmd/genpro4manual.pdf

[85] R. Santbergen, T. Meguro, T. Suezaki, G. Koizumi, K. Yamamoto, and M. Zeman, "Genpro4 optical model for solar cell simulation and its application to multijunction solar cells," *IEEE Journal of Photovoltaics*, vol. 7, no. 3, pp. 919–926, 2017.

[86] J.R.D'Errico. Surface fitting using gridfit. [Online]. Available: https://nl.mathworks.com/matlabcentral/fileexchange/8998-surface-fitting-using-gridfit

[87] M. A. Wank, "Manipulating the hydrogenated amorphous silicon growing surface," Ph.D. dissertation, TU Delft, Delft University of Technology, 2011.

[88] E. Guijt, "Application of intrinsic amorphous silicon oxide in multi-junction solar cells," Master's thesis, Delft University of Technology, 2014.

A

Electrical Parameters obtained during the optimization of grading width for a-SiO$_x$:H solar cells

Table A.1: Electrical parameters of graded bandgap energy a-SiO$_x$:H solar cells with varying grading widths in the p-i region.

p-i region grading width (nm)	V_{OC} (V)	FF	J_{SC} (mA/cm^2)	Efficiency (%)
10	0.960 ± 0.007	0.642 ± 0.007	13.12 ± 0.02	7.92 ± 0.11
20	0.967 ± 0.005	0.571 ± 0.008	13.02 ± 0.02	7.18 $\pm 0.11
30	0.955 ± 0.003	0.528 ± 0.012	12.06 ± 0.01	6.08 ± 0.13
40	0.936 ± 0.006	0.542 ± 0.018	12.27 ± 0.01	6.23 ± 0.21
60	0.957 ± 0.004	0.510 ± 0.005	12.44 ± 0.01	6.07 ± 0.06
80	0.946 ± 0.002	0.430 ± 0.008	11.44 ± 0.03	4.67 ± 0.14
100	0.971 ± 0.003	0.47 ± 0.02	11.81 ± 0.01	5.43 ± 0.25

Table A.2: Electrical parameters of graded bandgap energy a-SiO$_x$:H solar cells with varying grading widths in the i-n region.

i-n region grading width (nm)	V_{OC} (V)	FF	J_{SC} (mA/cm^2)	Efficiency (%)
20	0.964 ± 0.001	0.642 ± 0.007	13.36 ± 0.01	8.2 ± 0.1
40	0.951 ± 0.004	0.612 ± 0.027	13.22 ± 0.02	7.6 ± 0.3
60	0.93 ± 0.01	0.617 ± 0.004	13.14 ±0.02	7.53 ± 0.11
80	0.931 ± 0.001	0.68 ± 0.01	12.74 ± 0.03	7.99 ± 0.12
100	0.964 ± 0.002	0.64 ± 0.02	12.92 ± 0.02	7.92 ± 0.27
120	0.946 ± 0.001	0.56 ± 0.02	12.01 ± 0.02	6.44 ± 0.22
140	0.957 ± 0.006	0.60 ± 0.02	11.81 ± 0.01	6.89 ± 0.28
190	0.946 ± 0.006	0.59 ± 0,02	11.13 ± 0.04	6.18 ± 0.31

B

Electrical parameters of all graded bandgap energy a-SiO$_x$:H solar cells presented in Chapter 5

Table B.1: Electrical parameters of graded bandgap energy a-SiO$_x$:H solar cell with varying $E_{04,max}$

$E_{04,max}$ (eV)	V_{OC} (V)	FF	J_{SC} (mA/cm^2)	Efficiency (%)
2.1	0.964 ± 0.001	0.64 ± 0.01	13.36 ± 0.01	8.26 ± 0.17
2.2	0.981 ± 0.001	0.580 ± 0.008	13.57 ± 0.01	7.72 ± 0.12
2.3	0.97 ± 0.01	0.278 ± 0.008	13.15 ±0.01	3.53 ± 0.11
2.4	0.968 ± 0.003	0.363 ± 0.005	13.08 ± 0.01	4.61 ± 0.06
2.5	0.93 ± 0.04	0.32 ± 0.01	12.83 ± 0.02	3.85 ± 0.23

Table B.2: Electrical parameters of graded bandgap energy a-SiO$_x$:H solar cell with increasing i-layer thickness.

i-layer thickness (nm)	V_{OC} (V)	FF	J_{SC} (mA/cm^2)	Efficiency (%)
125	0.985 ± 0.003	0.61 ± 0.03	12.26 ± 0.02	7.35 ± 0.38
150	0.983 ± 0.002	0.62 ± 0.03	12.79 ± 0.03	7.77 ± 0.39
175	0.981 ± 0.001	0.610 ± 0.005	13.18 ±0.02	7.89 ± 0.07
200	0.981 ± 0.001	0.602 ± 0.005	13.22 ± 0.02	7.91 ± 0.07
225	0.982 ± 0.001	0.578 ± 0.007	11.65 ± 0.03	6.62 ± 0.08
250	0.977 ± 0.002	0.569 ± 0.002	13.91 ± 0.01	7.74 ± 0.03
275	0.976 ± 0.002	0.55 ± 0.01	14.39 ± 0.03	7.70 ± 0.18
300	0.977 ± 0.002	0.547± 0.009	14.36 ± 0.04	7.68 ± 0.13

C

Simulation of graded bandgap energy a-SiO$_x$:H solar cells.

C.1. Simulation of reference a-SiO$_x$:H solar cell

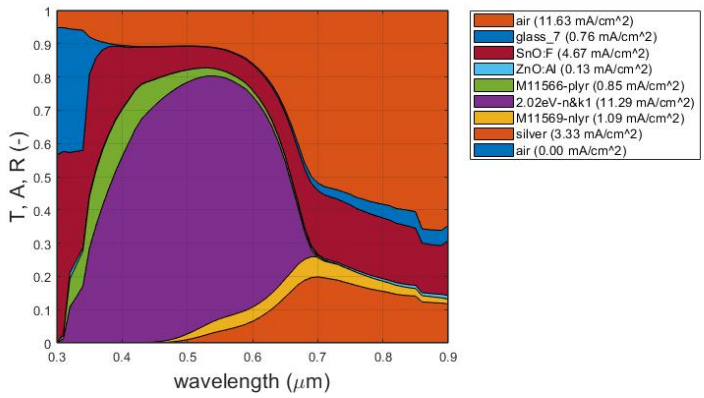

Figure C.1: Absorbance contributed by the layers in the reference a-SiO$_x$:H solar cell obtained from GenPro4 simulations.

Figure C.1 shows the simulation results of the reference a-SiO$_x$:H solar cell used in this work. The pyramidal texture of the Asahi VU substrate has also been implemented into the simulation. The i-layer of the solar cell shown in Figure C.1, is denoted by '2.02eV-n&k1'. The layers of the solar cells thicker than 100 nm are considered as a layer and thinner than 100 nm as an interface. GenPro4 plots the contribution of absorbance from every layer and the generated current corresponding to each of the layers. Thicknesses of the layers are expressed in micrometers.

Basically, the GenPro4 gives a plot like the one shown in Figure C.1 as the result of the simulation. In order to extract the absorbance values for each of the layers, the GenPro command is written as highlighted in Figure C.2.

```
clear Lay Int
load('AFM.mat','AsahiU_20um')
Lay(1).med ='air';                  Lay(1).thi = inf;
Lay(2).med = 'Glass_Eagle2000';     Lay(2).thi = 1000;
Lay(3).med = 'SnO:F';               Lay(3).thi = 0.7;
Lay(4).med = '2.04eV-n&k1';         Lay(4).thi = 0.2;
Lay(5).med= 'silver';               Lay(5).thi = 0.2;
Lay(6).med = 'air';                 Lay(6).thi = inf;

Int(1).model = 'flat';
Int(2).model = 'flat';

Int(3).model = 'ray';
Int(3).Z= -AsahiU_20um;                 Int(3).xy = [20e-6,20e-6];

Int(3).coat(1).med = 'ZnO:Al';          Int(3).coat(1).thi = 0.007;
Int(3).coat(2).med = 'M11566-plyr';     Int(3).coat(2).thi = 0.007;

Int(4).model= 'ray';
Int(4).Z= -AsahiU_20um;                 Int(4).xy = [20e-6,20e-6];

Int(4).coat(1).med = 'M11569-nlyr';     Int(4).coat(1).thi = 0.100;

Int(5).model = 'flat';

wav = 0.300:0.01:0.900;

[Lay,Int]=GENPRO4(Lay,Int,wav);
```

Figure C.2: Code for the GenPro4 simulation of the reference a-SiO$_x$:H solar cell.

C.2. Gridfit algorithm used for interpolating n and k data for i-a-SiO$_x$:H material

In chapter 6, a brief explanation about the gridfit algorithm is presented. In this section, the result obtained from the gridfit algorithm is shown. Gridfit calculates the refractive index n and extinction coefficient k as a function of bandgap energy and wavelength and shows a 3D surface plot of the optical constant data as shown in Figure C.3 and Figure C.4.

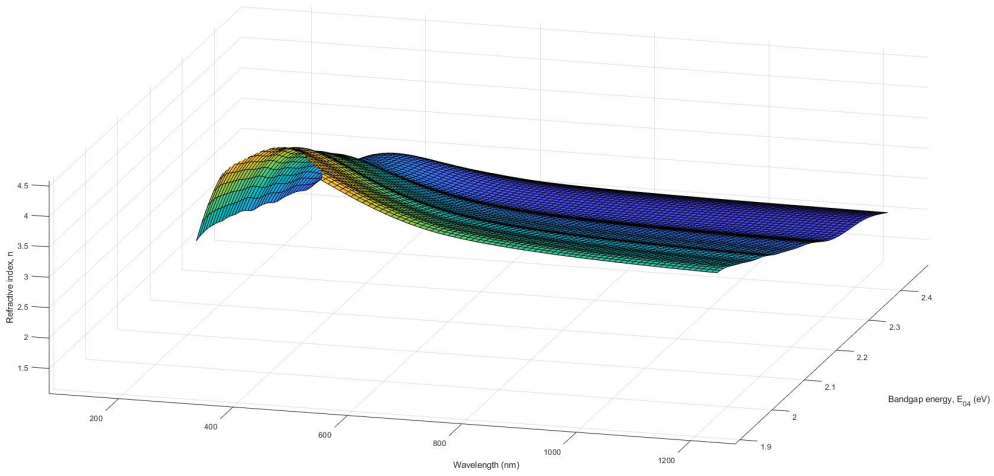

Figure C.3: The refractive index n for i-a-SiO$_x$:H layers for different bandgap energies and wavelength units as obtained from the gridfit algorithm.

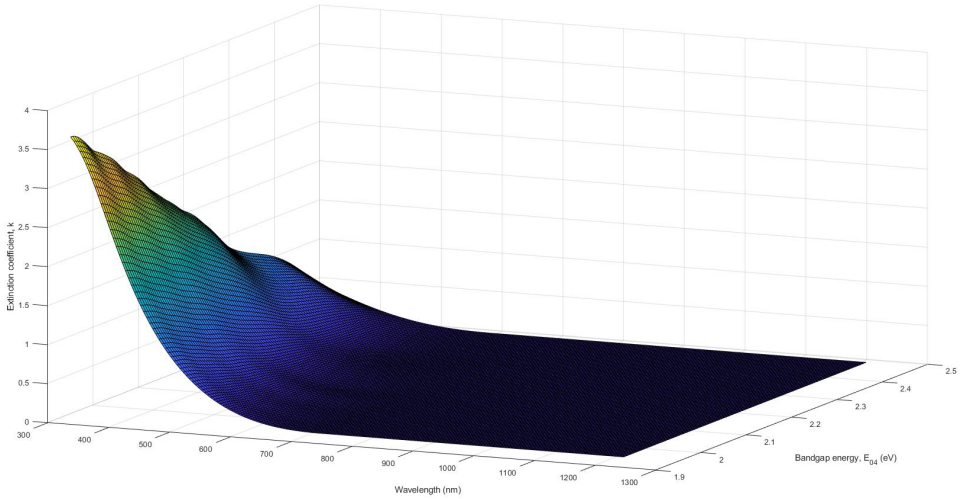

Figure C.4: The extinction coefficient k for i-a-SiO$_x$:H layers for different bandgap energies and wavelength units as obtained from the gridfit algorithm.

Figure C.5 shows the matlab code used for extracting the n and k data for an i-a-SiO$_x$:H layer with a particular bandgap energy. The code produces the data into a '.nk' file for swift use in GenPro4 simulations.

```
% defining wavelength
gx=300:10:1210;
% defining bandgap energy
gy=1.9503:0.01:2.486;
% obtain interpolated values for n and k
n=gridfitcopy(T.wav,T.e,T.k1,gx,gy);
k=gridfitcopy(N.wav,N.e,N.n1,gx,gy);
% program asks user for a bandgap energy value to extract the corresponding
% n and k data for an intrinsic layer with that bandgap energy
E=input('Enter your desired bandgap energy between 1.95 eV and 2.48 eV :')
d=round((E-1.95)/0.01)+1;
nm=transpose(gx);
k=transpose(g(d,:));
n=transpose(j(d,:));
L=table(nm,n,k);

% Outputs the n and k data for the i-layer into a '.nk' file for use in
% GenPro4
writetable(L,'2.48eV-n&k1.txt','Delimiter','tab');
movefile '2.48eV-n&k1.txt' 'nk/2.48eV-n&k1.nk'
```

Figure C.5: Matlab code for extracting the n and k data for a i-a-SiO$_x$:H layer with a particular bandgap energy.